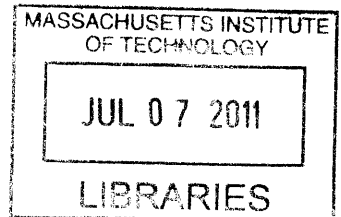


A Tilt Rotor UAV for Long Endurance Operations in Remote Environments

by

Josiah T. VanderMey



B.S., Aeronautical Engineering and Mathematical Sciences
United States Air Force Academy (2009)

ARCHIVES

Submitted to the Department of Aeronautics and Astronautics
in partial fulfillment of the requirements for the degree of

Master of Science in Aeronautics and Astronautics

at the

MASSACHUSETTS INSTITUTE OF TECHNOLOGY

May 2011
[June 2011]

© Massachusetts Institute of Technology 2011. All rights reserved.

Author
Department of Aeronautics and Astronautics
May 19, 2011

Certified by.....

Jonathan P. How

R. C. MacLaurin Professor of Aeronautics and Astronautics
Thesis Supervisor

Accepted by /...../.....

Eytan H. Modiano

Associate Professor of Aeronautics and Astronautics
Chair, Graduate Program Committee

A Tilt Rotor UAV for Long Endurance Operations in Remote Environments

by

Josiah T. VanderMey

Submitted to the Department of Aeronautics and Astronautics
on May 19, 2011, in partial fulfillment of the
requirements for the degree of
Master of Science in Aeronautics and Astronautics

Abstract

Extended mission times will greatly expand the utility of small UAVs that are currently limited to a single flight lasting no more than a few hours. This thesis assesses the challenges to developing a small, long endurance UAV and presents a preliminary vehicle and controller design for a tiltrotor UAV that achieves long endurance operation by combining autonomous takeoff and landing capabilities with a solar energy harvesting system.

Mass and power models are developed for the proposed vehicle configuration to provide mission performance and sizing analysis. Results indicate that a feasible design exists that is capable of achieving multiple, successive flights with continuous operation from one hour after sunrise to one hour before sunset. Based on the sizing results, a prototype tiltrotor vehicle is built with on-board sensing and control to demonstrate the required takeoff control capabilities.

The vehicle control architecture consists of a composition of locally valid feedback controllers. A nested PID linear feedback controller is implemented for the hover controller and dynamic inversion is used to cancel nonlinearities in the vehicle takeoff dynamics. Discontinuous control inputs during the transition between takeoff and hover controller modes are shown to result in undesirable transient behaviors that are mitigated by a an energy based switching algorithm. Using the prototype vehicle, the takeoff control algorithm is demonstrated successfully from several different terrains and starting orientations.

DISCLAIMER CLAUSE: The views expressed in this article are those of the author and do not reflect the official policy or position of the United States Air Force, Department of Defense, or the U.S. Government

Thesis Supervisor: Jonathan P. How
Title: R. C. MacLaurin Professor of Aeronautics and Astronautics

Acknowledgments

This thesis comes as the result of a great deal of support and encouragement. I would first like to thank Professor How for his guidance and the continual insightfulness that he provided. He never ceased to challenge me and encourage me to think more deeply through problems.

A great deal of appreciation is due to many individuals at MIT Lincoln Laboratories for both their financial and intellectual support of this project. In particular, I would like to extend thanks to Bob Shin, Kevin Cohen, and Marc Viera for taking the initiative to invest in on campus research and development through the BeaverWorks projects, and for the mentoring role that they have played. Throughout my interactions with Kevin Cohen, his desire to equip and enable students has been readily apparent, and I am sincerely indebted to him for his guidance and support. I would also like to thank Eli Cohen for patiently helping me with testing, thinking through problems, and ordering and printing countless parts for me. Julie Cusher and Pat DeCuir were extremely helpful in ensuring that I always had the resources that I needed.

Thanks to everyone in the Aerospace Control Lab for putting up with me and always being willing to lend advice or a helping hand. Specifically, I would like to thank Buddy Michini for patiently helping me understand and work through hardware issues, Andrew Kopeikin for always manning the override switch, video taping, and for providing encouragement, advice, and occasional commiseration, and Tuna Toksoz for always being in the lab to provide coding advice and general computer troubleshooting.

Finally, I would like to thank my family and friends. To all my Boston friends, thanks for a great two years. I have enjoyed our time together and sincerely appreciate all of your friendships. You will be missed. And to Mom and Dad, thanks for always being there to encourage me and listen to my problems. You are truly appreciated.

Thank you all.

HUB!

THIS PAGE INTENTIONALLY LEFT BLANK

Contents

1	Introduction	19
1.1	Motivation	19
1.2	Challenges	25
1.3	Contribution	28
1.4	Organization	29
I	Vehicle Performance and Design	31
2	Conceptual Design Exploration	33
2.1	Existing Aircraft	33
2.2	Conceptual Design and Evaluation	35
3	Sizing and Performance Analysis	39
3.1	Overview	39
3.2	Energy Model	40
3.2.1	Solar Irradiance	40
3.2.2	Aerodynamics	41
3.2.3	Propulsion	43
3.2.4	Summary	44
3.3	Mass Model	45
3.3.1	Solar Cells	45
3.3.2	Airframe	45
3.3.3	Propulsion System	46

3.3.4	Avionics	47
3.3.5	Battery	47
3.3.6	Summary	47
3.4	Sizing Constraints	48
3.5	Analysis	51
4	Prototype Vehicle Design	57
4.1	Tilt Rotor Aircraft Design Issues	57
4.2	Airframe and Aerodynamics	60
4.2.1	Wing and structure	60
4.2.2	Lateral Directional Stability	63
4.3	Propulsion	64
4.4	Power	65
4.5	Avionics	66
4.5.1	Actuators	66
4.5.2	Sensors	66
4.5.3	Controller	68
4.5.4	Wiring	69
4.6	Modified Sizing Model	69
II	Vehicle Control	73
5	Control Overview	75
6	Quaternion Attitude Descriptors	79
6.1	Reference Frames	79
6.2	Motivation	79
6.3	Quaternion Rotations	80
6.3.1	Quaternion Operations	80
6.3.2	Kinematics	82
6.4	Quaternion Error	83

6.5	Quaternion Linearization	84
7	Modeling and Simulation	87
7.1	Rotational Dynamics	87
7.1.1	Equations of Motion	87
7.1.2	Applied Torques	88
7.2	Translational Dynamics	91
7.2.1	Equations of Motion	91
7.2.2	Applied Forces	91
7.3	Thrust Model	92
7.4	Model Summary	93
7.5	Simulation	94
7.5.1	Overview	94
7.5.2	Validation	94
8	Hovering Control	99
8.1	Overview	99
8.2	Linearized Hovering Model	99
8.3	Attitude Control	101
8.4	Position Control	103
8.5	Hover Error Correction	105
8.6	Performance	108
8.6.1	Attitude Control	109
8.6.2	Position Control	109
8.6.3	Hover Region of Attraction Estimation	111
9	Takeoff Control	115
9.1	Overview	115
9.2	Pitch Only Model	116
9.3	Takeoff Trajectory	117
9.4	Takeoff Attitude Control	118

9.4.1	Algorithm	118
9.4.2	Performance	123
9.5	Switching Algorithm	126
9.6	Experimental Takeoff Results	134
10	Conclusions and Recommendations for Future Work	137
10.1	Conclusions	137
10.2	Future work	137
A	Sonar Validation and Test Data	143
A.1	Surface Test	143
A.2	Target Test	144
A.3	Interference Test	146
B	Linearization Details	149
References		152

List of Figures

1-1	Several UAVs currently employed by the US military: (a) Northrop Grumman RQ-4 Global Hawk [1], (b) General Atomics RQ-1 Predator [2], (c) AeroVironment RQ-11 Raven [3], and (d) AeroVironment Wasp III [4].	19
1-2	Maximum endurance vs. maximum takeoff weight for select UAVs from around the world [5].	22
1-3	Several power management approaches to long endurance MAVs: (a) Stanford University Perching [6], (b) USAF Academy Sticky-Pad Plane [7], and (c) Morphing Micro Air-Land Vehicle (MMALV) [8].	23
1-4	Several solar energy harvesting approaches to long endurance MAVs: (a) ETH SkySailor [9], (b) ETH Sun Surfer [10], (c) ISAE Solar Storm [11].	24
1-5	Sample mission for a long endurance, unattended solar UAV. Take off from a grassy field; Fly under solar power during the day; Land on a rooftop during cloud cover (recharge batteries); Take off once conditions improve; Land on rough, uneven terrain at night; Take off after the sun comes up.	25
1-6	Mission decomposition for a long endurance, unattended, energy harvesting UAV.	26
2-1	Several vertical takeoff and landing fixed wing UAVs: Sikorsky Cypher II [12] (a), Boeing X-50 Dragonfly [13] (b), Aurora GoldenEye 50 [14] (c), IAS Pitagora [15] (d), Bell Eagle Eye [16] (e), MLB V-Bat [17] (f). .	34

2-2	Aurora Flight Sciences Skate UAV.	35
2-3	Conceptual design takeoff scheme	36
2-4	Original (a) and modified (b) conceptual designs	37
3-1	Electric motor mass and maximum power for several high end brushless hobby motors	46
3-2	Solar model with power demand	50
3-3	Sizing results. Wing geometry (a), vehicle performance (b), and mass distribution (c)	53
3-4	Flight endurance, charge time, and duty cycle for a sized vehicle with $AR = 3$	55
4-1	Prototype vehicles: Initial prototype with single boom mounted vertical stabilizer (a), Second prototype with in-wing, pivoting vertical stabilizers (b).	58
4-2	Opposed lateral tilting prototype presented in [18].	59
4-3	Motor pivots (a) and support attachments (b).	61
4-4	Lateral directional stability augmentation of low aspect ratio wings	63
4-5	Propulsion system components	65
4-6	Prototype power system	66
4-7	Hitec HS-5245MG servo	66
4-8	Prototype sensors: (a) MicroStrain 3DM-GX3-25OEM IMU, (b) MaxBotix XL-MaxSonar-AE2 ultrasonic rangefinder, (c) Spektrum AR6110E Microlite 6-Channel DSM2 receiver, (d) XBee-PRO 900 extended range module with XtreamBee board.	67
4-9	Sparkfun ArduPilot Mega board with ATmega1280 and ATmega328.	68
4-10	Installed avionics and controller setup.	69
4-11	Mass comparison between prototype vehicle and sizing model results.	70
4-12	Sizing results for the modified sizing model: (a) Wing geometry, (b) vehicle performance, and (c) mass distribution.	72

5-1	Multi-modal control structure, where arrows represent transitions between controller modes.	76
6-1	Body fixed reference frame.	80
7-1	Motor test setup (a) and thrust data surface fit (b).	92
7-2	Prototype with standoff on trailing edge to simulate off nominal pivot locations	95
7-3	Simulated pitch response compared to experimental results for an open loop pitch up manuever with the pivot location at the trailing edge (a-c), 150 mm behind the trailing edge (d-f), and 300 mm behind the trailing edge (g-i).	96
7-4	Simulated pitch response compared to experimental results for a closed loop pitch up manuever with the pivot location at the trailing edge (a-c) and 150 mm behind the trailing edge (d-f).	97
7-5	Simulated pitch response with no delay compared to experimental results for a closed loop pitch up maneuver with the pivot location at the trailing edge (a-c) and 150 mm behind the trailing edge (d-f).	97
8-1	Example error calculation scenario with (a) desired and (b) measured orientations.	106
8-2	Heading angle calculation from y and z axis projections.	108
8-3	Prototype vehicle autonomously hovering with attitude and altitude control.	109
8-4	Attitude impulse responses. (a) x axis error for a 2.1 rad/sec impulse, (b) y axis error for a 4.9 rad/sec impulse, (c) z axis error for a 2.1 rad/sec impulse.	110
8-5	Filtered sonar altitude error measurements during hovering flight.	110
8-6	Vehicle translational position response to a simultaneous 1 m step input in X and Y	111

8-7	Experimental region of attraction data for the body y axis (a) and z axis (b) errors	112
8-8	Sum-of-squares approximation of the hover controller y axis region of attraction with actuator delays.	113
9-1	Desired takeoff trajectory in time (a) and phase (b) with a maximum pitch rate of 0.5 rad/sec , an angular acceleration of 1.0 rad/sec^2 , and an angular deceleration of 0.3 rad/sec^2	118
9-2	Simulated pitch response with five experimental results for a takeoff rotation from a flat, horizontal surface.	124
9-3	Off-nominal test setups: (a) 100 mm inboard pivot, (b) 200 mm offset, and (c) 30 deg incline.	124
9-4	Takeoff test data from the following surfaces and configurations: (a) flat, level surface, (b) 100 mm inboard pivot, (c) 100 mm offset, (c) 200 mm offset, (e) 15 degree incline, (f) 15 degree decline, (g) 30 degree incline, (h) 30 degree decline.	125
9-5	Experimental pitch responses for takeoff rotations from a variety of terrains and starting orientations with simulated hovering responses. .	127
9-6	Simulated hovering responses after switching from experimentally obtained takeoff trajectories based on a minimum rate constraint of 0.1 rad/sec , a maximum angle constraint of $\pi/2 - 0.1 \text{ rad}$, and phase tangency switching with a tolerance of $\pm 0.1 \text{ 1/sec}$ for pitch angles above 1.07 rad . Simulated responses are displayed as dotted lines, while the experimental data is shown as solid lines.	129
9-7	Experimentally obtained takeoff trajectory based on a minimum rate constraint of 0.1 rad/sec , a maximum angle constraint of $\pi/2 - 0.1 \text{ rad}$, and phase tangency switching with a tolerance of $\pm 0.1 \text{ 1/sec}$ for pitch angles above 1.07 rad	129
9-8	Energy based switching condition and linear approximation	130
9-9	Slope of Equation 9.31 evaluated at $\pi/4 \text{ rad}$	131

9-10 Simulated hovering responses after switching from experimentally obtained takeoff trajectories with an energy based switching condition with a slope of $-3.5 \text{ }^1/\text{sec}$ and a maximum angle of $\pi - 0.1 \text{ rad}$ for pitch angles above $\pi/4 \text{ rad}$. Simulated responses are displayed as dotted lines, while the experimental data is shown as solid lines.	131
9-11 Experimental responses with energy based switching conditions with a slope of $-3.5 \text{ }^1/\text{sec}$ and a maximum angle of $\pi - 0.1 \text{ rad}$ for pitch angles above $\pi/4 \text{ rad}$	133
9-12 Simulated hovering responses after switching from experimentally obtained takeoff trajectories with an energy based switching condition with a slope of $-3.5 \text{ }^1/\text{sec}$ and a maximum angle of $\pi - 0.1 \text{ rad}$ for pitch angles above $\pi/4 \text{ rad}$. Servo input is offset at the controller transfer with a decay time constant of 77 ms. Simulated responses are displayed as dotted lines, while the experimental data is shown as solid lines. . . .	133
9-13 Experimental pitch responses for takeoffs with an energy based switching condition with a slope of $-3.5 \text{ }^1/\text{sec}$ and a maximum angle of $\pi - 0.1 \text{ rad}$ for pitch angles above $\pi/4 \text{ rad}$. Servo input is offset at the controller transfer with a decay time constant of 77 ms.	135
9-14 Pitch time histories for takeoffs with an energy based switching condition with a slope of $-3.5 \text{ }^1/\text{sec}$ and a maximum angle of $\pm\pi - 0.1 \text{ rad}$ for pitch angles above $\pi/4 \text{ rad}$. Servo input is offset at the controller transfer with a decay time constant of 77 ms.	136
10-1 Conceptual design of a vehicle capable of performing the desired takeoff maneuver without the pitch up rotation in (a) Level flight and (b) takeoff/hover.	139
A-1 Test surfaces: (a) asphalt, (b) dirt, (c) gravel, (d) grass, and (e) 0.3 m bush.	144
A-2 Range measurements from (a) 0.80 m, (b) 0.50 m, (c) 0.30 m, and (d) 0.25 m.	145

A-3 Target test (a) targets and (b) test setup.	146
A-4 Target test results from (a) 0.5 m, (b) 1.0 m, (c) 2.0 m, (d) 5.0 m, and (e) 7.0 m	147
A-5 Motor interference test results	148

List of Tables

3.1	Sizing parameters	52
3.2	Sizing results for $AR = 3$	54
4.1	Modified sizing results for $AR = 3$	72
5.1	Mission phases	77
A.1	Target dimmensions	146

THIS PAGE INTENTIONALLY LEFT BLANK

Chapter 1

Introduction

1.1 Motivation

The demand for information and situational awareness both on and off the battlefield has led to increased military utilization of UAVs as sensor platforms for surveillance and communications. From 1995 to 2010, the iconic MQ-1 Predator, shown in Figure 1-1(b), flew more than 405,000 flight hours with the majority taking place over combat areas [19, 20]. Similarly, in its first seven years of military service, the RQ-4 Global Hawk logged over 17,000 combat flight hours, providing high resolution intelligence, surveillance, and reconnaissance data that formed a large component of the targeting imagery for strike mission support during Operation Iraqi Freedom [21]. In addition to military applications, UAV systems are also being used in civil applications such as border patrol and environmental monitoring [20, 22].

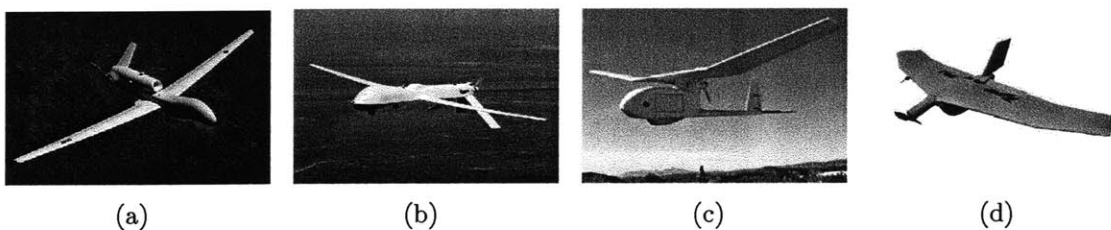


Figure 1-1: Several UAVs currently employed by the US military: (a) Northrop Grumman RQ-4 Global Hawk [1], (b) General Atomics RQ-1 Predator [2], (c) AeroVironment RQ-11 Raven [3], and (d) AeroVironment Wasp III [4].

While large UAV systems like the Predator and Global Hawk are capable of achieving long endurance and range, they are complex systems that require extensive dedicated ground support including both physical infrastructure and significant personnel resources for operation, maintenance, and information processing. These support requirements are costly and can be prohibitive in terms of where the aircraft may operate. The time and fuel spent in transit from UAV launch locations to their desired targets can hinder their utility in time critical situations or tactical environments.

Over the last two decades, emerging technologies in microprocessors, communications, sensors, energy storage, propulsion, materials, and fabrication have enabled the development of small UAVs capable of carrying payloads with functionality similar to larger UAV systems. The ability to rapidly transport and deploy these UAVs with minimal infrastructure and support makes them particularly well suited to supplement large UAV systems through their integration with military operations at a tactical level.

The U.S Air Force Remotely Piloted Aircraft and Unmanned Aerial Vehicle Strategic Vision notes the significance of small UAVs, stating [20]:

Small UAVs provide a unique capability to get close to a target and provide “bird’s eye view”. Their small size, quiet propulsion systems, and ability to feed information directly to Battlefield Airmen enhance the combat effectiveness of our forces.

and

By taking advantage of their small size, increased maneuverability, and low-altitude flight, small UAVs can assist in defeating camouflage, concealment, and deception techniques to locate and identify targets.

Furthermore, the size, operating altitude, and low flight speed of small UAVs provide them with inherent low observability characteristics. Additional efforts to design flight paths and vehicle profiles could help prevent identification by allowing small UAVs to be mistaken for birds.

The low masses and energies associated with small UAVs allows them to operate in close proximity to humans and infrastructure with little risk of damage or harm. This feature, makes small UAVs an ideal solution for combat identification of friendly, adversary, and neutral forces [20].

Size and the use of off the shelf components make small UAV acquisitions significantly less expensive than larger vehicles. The Aeroenvironment RQ-11 Raven costs \$173,000 for a complete system [3]; more than 400 times less than the cost of larger systems like the RQ-4 Global Hawk [21]. As a result of their lower cost, small UAVs can encourage widespread employment.

A number of small UAV systems have already been developed with optical sensors designed to give front line troops over-the-hill reconnaissance and real-time situational awareness. Two of the most notable examples, shown in Figure 1-1, are the Aeroenvironment RQ-11 Raven and Wasp III. The Raven is a 1.4m wingspan UAV with a range of 8-12 km and an endurance of 60-90 minutes that is currently used by all of the US military service branches in combat locations including Iraq and Afghanistan. With a wingspan of only 25.4 cm, The Wasp III provides similar surveillance capabilities in an even smaller, more mobile package [3, 4].

Small size and portability also make civilian UAV applications more appealing. The Washington State Department of Transportation has investigated the use of man-portable UAVs in applications as diverse as avalanche control, search and rescue, crash scene photography, land-use mapping, surveying, security inspections, hazardous material monitoring, construction data collection, aerial surveillance, and monitoring the traffic conditions of congested roadways [23].

The downside to small UAVs comes in the form of restricted endurance. Figure 1-2 clearly demonstrates the trend towards reduced endurance associated with smaller UAV designs. This trend is a result of both limited available mass for energy storage and the reduced efficiency of low Reynolds number aerodynamics. For UAVs with a maximum takeoff weight of less than 5 kg, endurance is typically limited to no more than a few hours [5].

With longer endurance times, small UAVs could more fully capitalize on the ad-

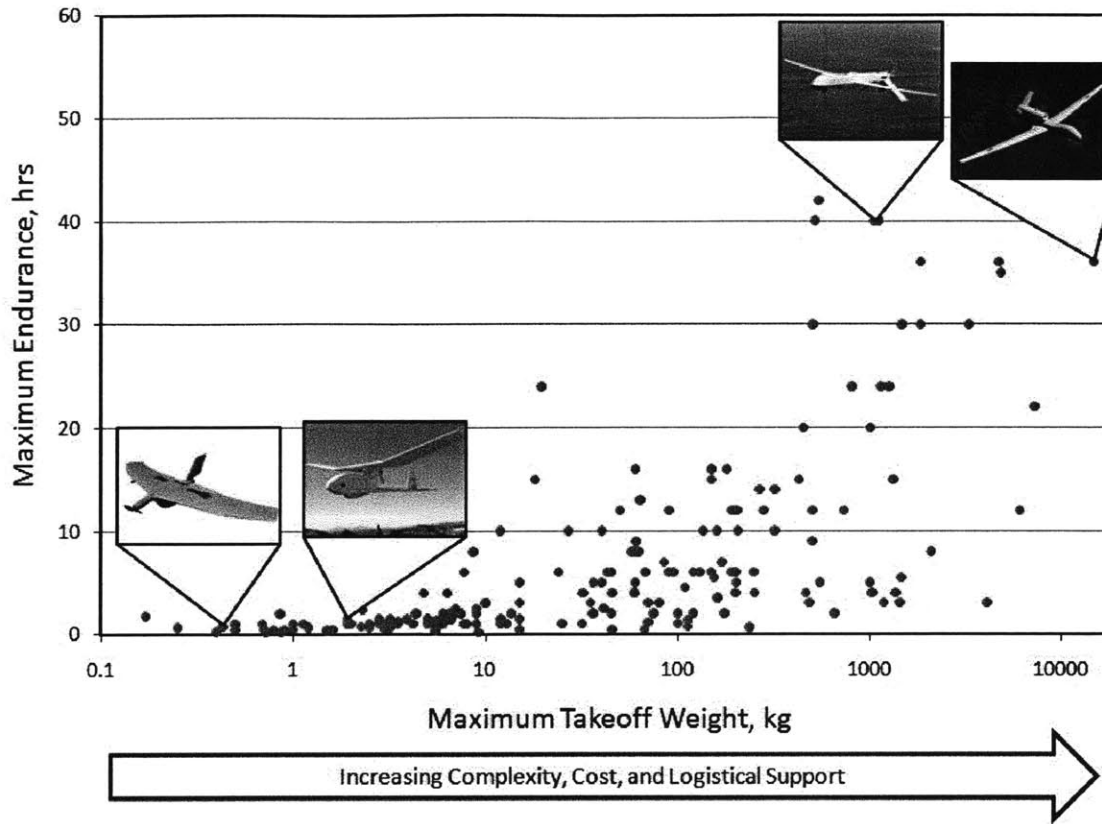


Figure 1-2: Maximum endurance vs. maximum takeoff weight for select UAVs from around the world [5].

vantages provided by their size and cost. Additional long endurance missions could include persistent surveillance, exploratory reconnaissance, vehicle tracking, mobile communication relays or sensor networks, environmental monitoring, chemical dispersion tracking, and extended boarder and coastal patrol. Several small UAVs capable of persistent operation could work together to provide continuous, large area coverage. In doing so, they would enable rapid response to time critical targeting and surveillance requests. In a net-centric architecture, this information could be combined with satellite imagery and other forms of intelligence to provide decision makers with improved situational awareness.

UAVs with longer endurance times will alleviate demands on ground crews by requiring fewer launches and recoveries [20]. The ability to achieve longer endurance times will also allow for greater levels of autonomy. As a result, operators will be able to focus more on processing the data collected from the UAV rather than on

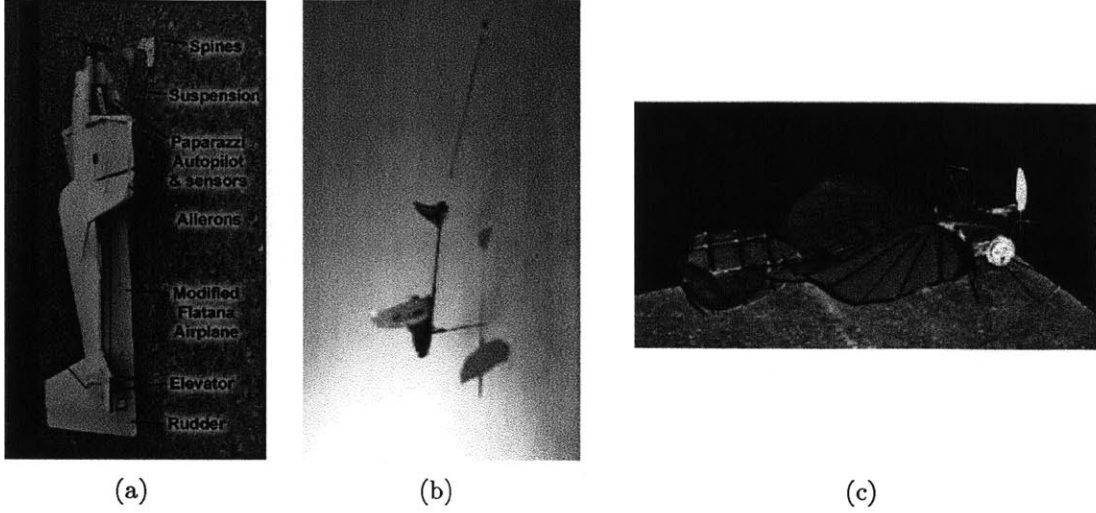


Figure 1-3: Several power management approaches to long endurance MAVs: (a) Stanford University Perching [6], (b) USAF Academy Sticky-Pad Plane [7], and (c) Morphing Micro Air-Land Vehicle (MMALV) [8].

controlling, operating, and maintaining the vehicle.

Current strategies for achieving long endurance operations for small UAVs can be generally described as either power management or energy harvesting approaches. The UAVs shown in Figure 1-3 are examples of the power management approach. Once it has reached an area of interest, the UAV will land or perch on a vertical surface in order to reduce on station power consumption. While this approach does allow for extended operation, these designs do not facilitate dynamic missions like tracking and are still fundamentally limited in their endurance. Additionally, they typically require stringent landing conditions and must remain undisturbed in order to resume flight [6–8].

Small, solar powered sailplanes like the one shown in Figure 1-4(a) have demonstrated flights in excess of twenty four hours. Nevertheless, these demonstrations have occurred during summer months, under ideal conditions, with small payloads and slim energy margins, limiting their use to tightly regulated conditions that preclude them from extended continuous operation in uncooperative environments [24].

A design that incorporates both the low power features of a UAV capable of making repeated takeoffs and landings with an energy harvesting mechanism such as solar cells would allow for a UAV that is capable of both long term operation

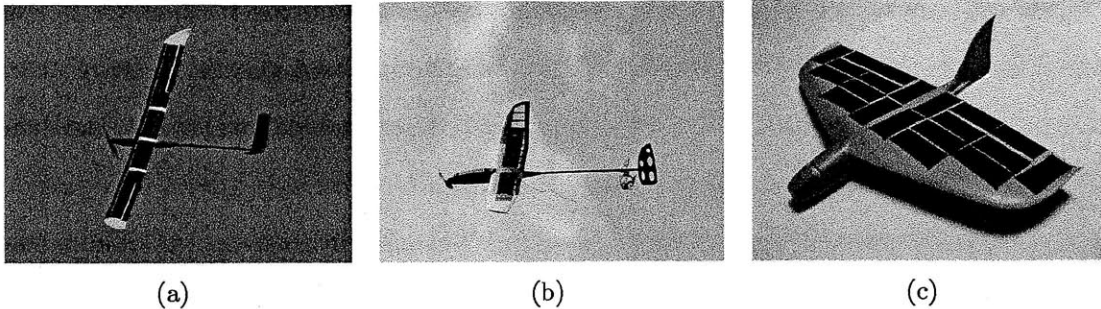


Figure 1-4: Several solar energy harvesting approaches to long endurance MAVs: (a) ETH SkySailor [9], (b) ETH Sun Surfer [10], (c) ISAE Solar Storm [11].

and dynamic missions. Figure 1-5 depicts a sample mission for a such a UAV with solar energy harvesting capabilities. During unfavorable conditions where the vehicle is unable to collect or store sufficient energy to maintain flight, it would land and wait for conditions to improve. With a repeatable takeoff and landing capability, this approach would allow for an indefinite extension of mission times. The cost of this approach comes with the inability to achieve continuous operation. However, intelligent selection of landing site locations could allow for time spent on the ground to be used for conducting mission activities.

Energy harvesting is possible from a number of readily available energy sources such as solar radiation, thermal potentials, and electromagnetic emissions [25]. Nevertheless, due to its technical maturity, high energy density, ease of implementation, proven integration with air vehicles, and consistent supply in diverse geographic locations, solar energy was selected as the preferred energy source.

In order to be fully effective, an increase in man-portable UAV endurance needs to be accompanied by an increased level of autonomy. While existing UAVs like the Raven and Wasp III are capable of fully autonomous way-point navigation, way-points must be computed and updated by the user. For each flight, the operator must determine an optimal set of way-points for the given mission objective and perform continuous monitoring during the flight. The requirement for these vehicles to be manually launched further limits their autonomy to a single flight.

A fully autonomous man-portable UAV would be capable of unattended operation without any external support or intervention for extended periods of time and over

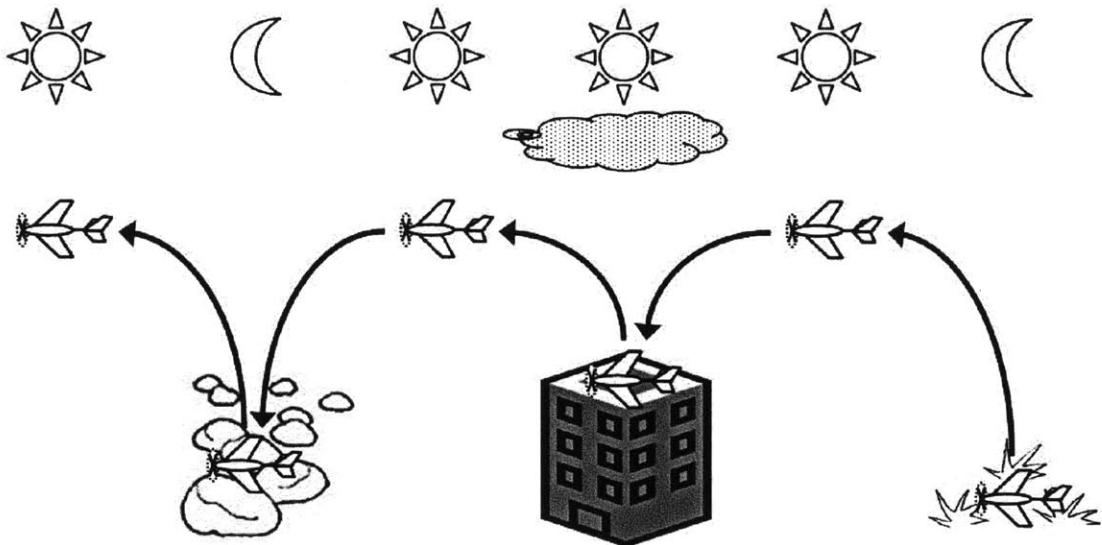


Figure 1-5: Sample mission for a long endurance, unattended solar UAV. Take off from a grassy field; Fly under solar power during the day; Land on a rooftop during cloud cover (recharge batteries); Take off once conditions improve; Land on rough, uneven terrain at night; Take off after the sun comes up.

large geographic areas. Such missions could require the vehicle to perform on-line re-planning, and multiple autonomous takeoffs and landings from a variety of unknown, unconditioned, and potentially uncooperative terrains in remote locations. These capabilities could allow for numerous UAVs to be operated with minimal operator demand.

1.2 Challenges

Figure 1-6 shows a functional decomposition of the elements that make up a persistent, unattended UAV mission with energy harvesting. Unlike typical mission decompositions in which the start and end of the mission are decoupled by recovery and servicing by ground crews, the persistent, unattended mission presented here is cyclical with a seamless transition from the end of the mission back to the beginning to allow for sustained operations through repeated takeoffs and landings.

Clearly, flight performance and mission planning are significant challenges for an unattended, long endurance UAV. Low Reynolds number aerodynamics associated



Figure 1-6: Mission decomposition for a long endurance, unattended, energy harvesting UAV.

with small UAVs tend to be less efficient than those of larger vehicles. Similarly, path planning and flight scheduling will also have a significant effect on the performance of the vehicle.

Nevertheless, while path planning and aerodynamic optimization are important for vehicle performance and effectiveness, they do not enable the basic functionality of the vehicle. As shown in Figure 1-6 the takeoff and landing capabilities are vital to the persistent UAV mission functionality. Typically, takeoff and landing in diverse environments necessitate the use of rotary wing vehicles. However, the large surface area requirement of solar energy harvesting and the desire for efficient flight characteristics precludes the use of such vehicles in this application. Accordingly, an autonomous takeoff and landing mechanism must be developed for a fixed wing aircraft. This challenge is fundamental to the concept and its solution will have a significant impact on the utility of the system since it will constrain where the vehicle is capable of operating. A complete solution will address the following issues:

1. Independent Operation

The vehicle must be capable of landing and taking off autonomously without dedicated ground infrastructure. Furthermore, it is desired that the vehicle be able to operate over both urban and rural areas encompassing diverse terrain.

As a result, the vehicle takeoff and landing mechanism should not require any

ground infrastructure that is unique to a particular environment (e.g. elevated surfaces, suspended power lines, trees, etc.). In the same manner, the vehicle should be able to take off and land from diverse terrain with varying levels of surface roughness, composition, grade, and other large features like shrubs, rocks, or tall grass. Limitation to prepared or well conditioned surfaces would impose restrictions on the operating capabilities of the vehicle.

2. Robust Operation from Diverse, Uncooperative Terrain and Environments

The takeoff and landing system also needs to be highly robust and allow for repeatable takeoffs and landings. Failure of this system will terminate the mission. The design should account for environmental perturbations like wind gusts both on the ground and in the air. If the vehicle experiences a strong gust on the ground, it should either be able to resist flipping or should be able to function in a number of different orientations. The robustness and versatility of a well designed takeoff and landing algorithm may reduce the demand on collision avoidance and landing site selection mechanisms. The vehicle should allow for adequate performance even from a poor landing site, thereby reducing the importance of optimal landing site selection. Similarly, in the event of a low altitude collision, the vehicle should be able to rebound or survive a crash, allowing the takeoff mechanism to resume the mission.

3. Autonomous Operation

Autonomous operation requires integration of a flight controller and associated feedback sensors capable of stabilizing and controlling the aircraft through the entire takeoff and landing operation. The controller must be robust and its sensing and processing capabilities must be balanced with the need to conserve both weight and power.

4. Optimal Solar Utilization

While on the ground or in the air, it is desirable to orient the wings to provide the largest cross section to incoming solar radiation. Solar tracking is not required,

but the wings should be kept in an orientation near horizontal both during flight and on the ground.

5. Collision Avoidance

In many operating environments, man-made structures or natural features present obstacles near the ground. Avoiding these obstacles during takeoff and landing presents an additional challenge that the takeoff and landing mechanism must be able to account for. In addition to its impact on takeoff and landing, adept collision avoidance could increase the functionality of the proposed UAV by allowing it to navigate through crowded environments at low altitudes.

6. Precision Landing

When operating in urban environments or over variable terrain, precision landing may be important in order to ensure that the vehicle is able to land on the specified surface (e.g. a specific rooftop, on top of a vehicle, or a space between buildings). The need for precise landing requires high resolution sensing and control during the landing maneuver. Further complicating this issue is the fact that physical obstructions or electromagnetic interference may render GPS ineffective in urban or other highly crowded environments.

1.3 Contribution

This thesis develops and demonstrates a design for a fixed wing aircraft that is capable of repeated, autonomous takeoff and landing from a variety of unprepared, uncooperative terrains. The work presented here contributes to the existing literature in the following ways:

1. **Design of a fixed wing vehicle that is capable of taking off and landing on diverse terrain while supporting a nominal payload mass and solar cell integration**

The contribution of the vehicle design comes from its mode of operation and its uniqueness from existing aircraft designs. The vehicle design serves as a proof

of concept to demonstrate the feasibility of the proposed takeoff maneuver. The design addresses issues as to why existing designs are insufficient for the proposed task and what additional considerations must be taken into account to accommodate the desired functionality.

2. Sizing and Performance Analysis

A performance model is adapted to the proposed vehicle design and concept of operations and is used to demonstrate the feasibility of the proposed mission concept. Vehicle performance parameters are identified and used to select a sized design configuration.

3. Takeoff controller design and testing

The challenges to autonomous takeoff are identified and addressed through a controller design that allows for takeoff from diverse, unknown terrains. The controller is implemented in hardware and experimental results are presented.

4. Evaluation of additional performance capabilities or limitations of the proposed vehicle design

The performance capabilities and limitations that arise due to the unique features of the vehicle design are explored to provide insight into the merit of the design features and potential areas of future research.

1.4 Organization

The remainder of the work presented in this thesis is structured as follows:

Part I addresses the vehicle design process.

Chapter 2 presents the conceptual phase of the vehicle design. Existing aircraft and original designs are considered and evaluated. A final vehicle configuration is selected to provide the desired functionality.

Chapter 3 presents a solar and performance model for the vehicle. The trade space is analyzed and the configuration is sized accordingly. Performance results for

the sized aircraft are presented.

Chapter 4 outlines the physical design of the prototype vehicle. A review of tilt rotor designs guides the design process. All sensors, actuators, and hardware are described.

Part II addresses the vehicle control architecture.

Chapter 5 consists of a review of related work in controls. Other fixed wing aircraft capable of hover and transition to level flight are considered as well as vehicles capable of performing agile maneuvers. Control approaches are evaluated and a multi modal controller composition is selected based on the identification of four distinct mission phases.

Chapter 6 introduces the quaternion attitude representation framework and provides a brief overview of the quaternion error calculation used in the vehicle control.

Chapter 7 develops a nonlinear dynamics model for the prototype vehicle. The model is used to create a simulation that is validated against experimental data.

Chapter 8 presents the control development for hovering flight. The model is linearized about the hovering condition and a linear feedback controller is implemented. The stability of the hovering controller is evaluated using both sum of squares and experimental techniques.

Chapter 9 presents the control development for takeoff while the vehicle is on the ground. A switching algorithm is developed to provide acceptable transient responses during the transition between controller modes. Simulated and experimental takeoff results are presented.

Chapter 10 outlines future work that will build on the capabilities demonstrated in this thesis. The suggested work will lead towards a complete system capable of persistent operation.

Part I

Vehicle Performance and Design

THIS PAGE INTENTIONALLY LEFT BLANK

Chapter 2

Conceptual Design Exploration

2.1 Existing Aircraft

Autonomous takeoff and landing has been successfully demonstrated in many fixed wing aircraft of varying sizes and configurations. In fact, several commercial autopilots are available with built in takeoff and landing functionality [26, 27]. However, for fixed wing aircraft, the takeoff and landing maneuvers typically consist of standard runway approaches that require well prepared terrains with minimal obstructions. The requirement of these vehicles to fly above stall speed further restricts landing sites to regions with sufficient above ground clearance to descend and land. This restriction prohibits the use of such systems on unprepared, uncooperative terrain or in areas with cluttered near earth environments. Helicopters and other rotary aircraft have typically been used to circumvent this issue, however, as mentioned previously, the lack of available wing area on such vehicles prohibits their integration with solar cells.

In order to bridge the gap between the performance of fixed wing aircraft and the takeoff and landing capabilities of rotary wing vehicles, a number of hybrid designs have been proposed that consist of both an articulated or fixed rotor that allows the vehicle to takeoff and land vertically and a fixed wing area for efficient forward flight. A few examples of such aircraft can be seen in Figure 2-1. Several designs, like the Boeing X-50 Dragonfly use the fixed wing as a rotor during vertical flight and then

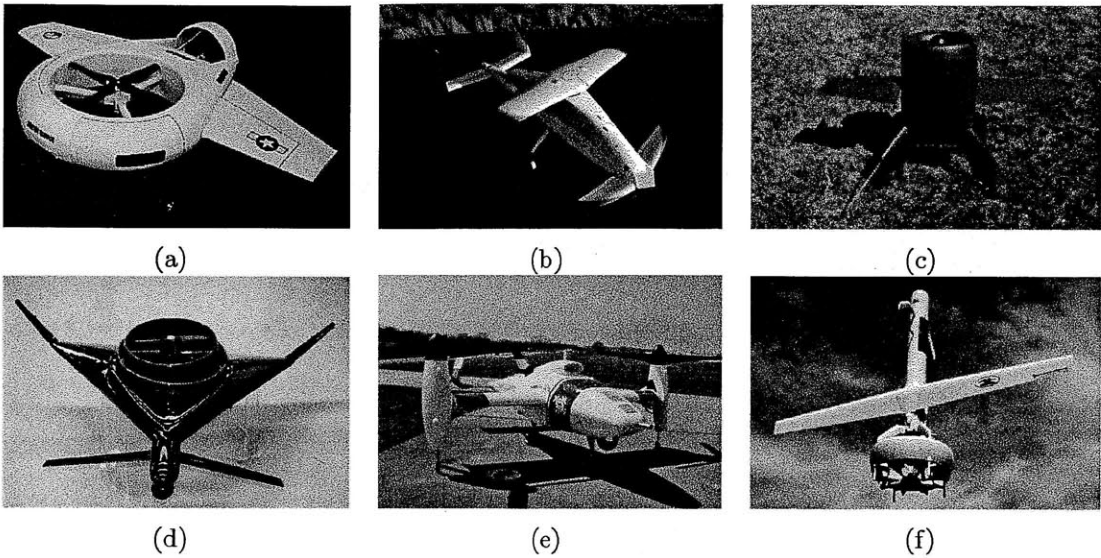


Figure 2-1: Several vertical takeoff and landing fixed wing UAVs: Sikorsky Cypher II [12] (a), Boeing X-50 Dragonfly [13] (b), Aurora GoldenEye 50 [14] (c), IAS Pitagora [15] (d), Bell Eagle Eye [16] (e), MLB V-Bat [17] (f).

lock it in place for forward flight.

While these vehicles do allow for expanded takeoff and landing capabilities, they all have high wing loadings that would result in minimal on station time before landing to recharge if they were integrated with solar cells.

The Aurora Flight Sciences Skate, shown in Figure 2-2, is a small UAV that provides low wing loading and vertical takeoff and landing capabilities through the use of two independently articulated rotors [28]. Nevertheless, like the MLB V-Bat, the Skate can only takeoff and land from a vertical orientation. In a long endurance mission with multiple takeoffs and landings, it is likely that the vehicle could land on uneven terrain and fall over or be knocked down by winds, rendering it incapable of takeoff.

The limitations of existing aircraft designs would impose restrictions on both their effectiveness as energy harvesting platforms and where they could be used in long endurance missions requiring multiple takeoffs and landings. In some cases, their additional failure modes would introduce significant risk to the mission completion. Accordingly, a new aircraft design is needed that is capable of repeated takeoff and landing from unimproved, uncooperative terrain while providing sufficiently low wing

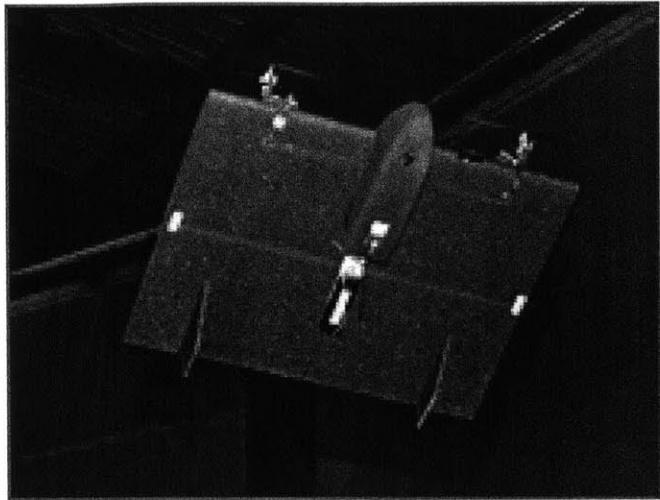


Figure 2-2: Aurora Flight Sciences Skate UAV.

loading for integration with solar cells.

2.2 Conceptual Design and Evaluation

Takeoff and landing conceptual designs were evaluated based on the following criteria:

- Dependence on terrain
 - Infrastructure requirements
 - Surface condition requirements
 - Takeoff and landing volume
- Robustness
 - Ability to make multiple takeoff attempts
 - System failure due to disturbances while in a low power state
- Performance
 - Additional mass
 - Power consumption
 - Effect on aerodynamic performance
 - Vehicle size

In the preliminary design phase over 20 different concepts were generated. These designs included traditional wheeled vehicles, jumping vehicles, perching vehicles, flapping wing vehicles, rocket propelled vehicles, variable geometry vehicles, ducted

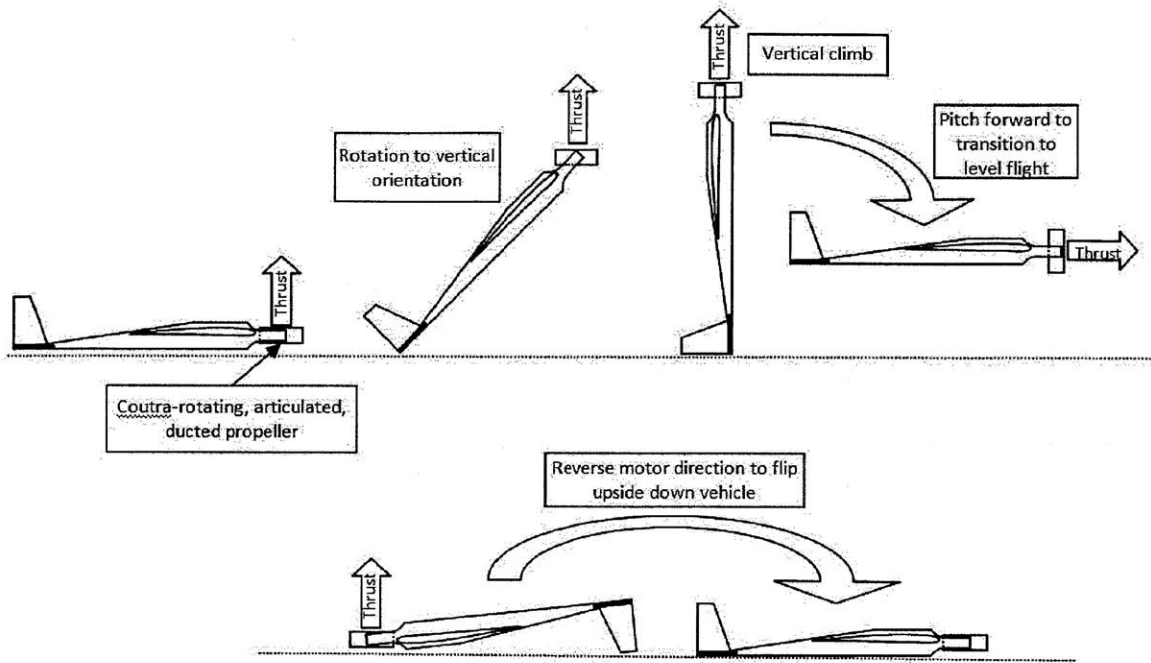


Figure 2-3: Conceptual design takeoff scheme

fans in annular wings, lighter than air vehicles, and vertical takeoff and landing vehicles with articulated rotors. Designs that were highly dependent on terrain or likely to fail from disturbances while on the ground were rejected immediately due to their inability to effectively facilitate the required mission. The remaining designs were evaluated based on their performance characteristics.

The design that presented the best performance and reliability consisted of an articulated, ducted propeller with contra-rotating blades located in front of the aircraft. As shown in Figure 2-3, the vehicle would takeoff by pointing the rotors vertically and rotating the entire airframe to a vertical orientation. It would then enter a vertical climb and, upon reaching the desired altitude, pitch forward to transition to level flight. The use of the rotor thrust to provide the takeoff force minimizes any terrain dependence.

By simply reversing the rotor direction or articulating them in the opposite direction, the vehicle would be capable of righting itself in the event that it landed upside down or was flipped upside down by winds. Additionally, a failed takeoff attempt would alter the starting orientation, but would not preclude a second attempt. Sim-

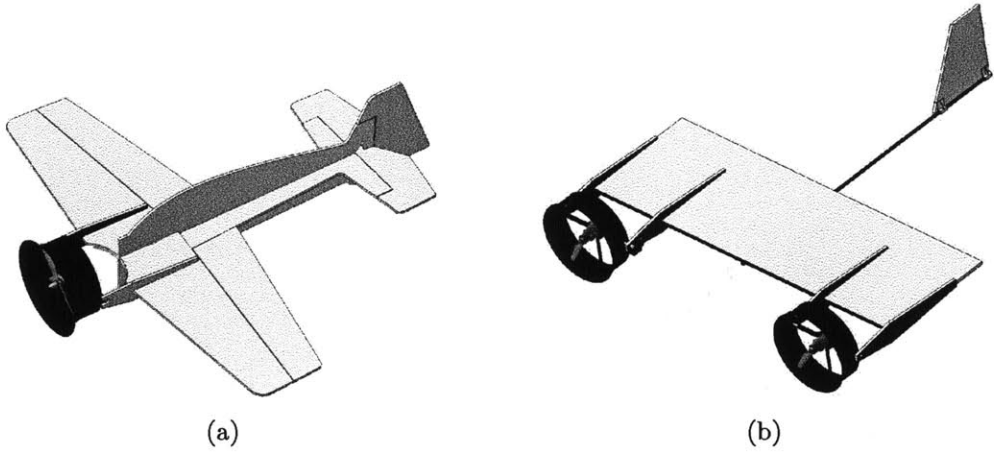


Figure 2-4: Original (a) and modified (b) conceptual designs

ilar vehicles have demonstrated successful transitions from hovering flight to forward flight through the use of relatively simple, multimodal PID controllers [29].

The initial prototype design consisted of only a single contra-rotating ducted propeller and aerodynamic control surfaces, however, as depicted in Figure 2-4 this design was quickly abandoned in favor of two counter rotating rotors located along the wings. This change allows for increased lateral-directional control authority while reducing the required articulation to a single axis.

The modified design is very similar to the Aurora Flight Sciences Skate, however, the rotors are located much further in front of the wing. This change provides additional control authority and prevents the wing from blocking the rotor slipstream flow when they are fully articulated at takeoff.

THIS PAGE INTENTIONALLY LEFT BLANK

Chapter 3

Sizing and Performance Analysis

3.1 Overview

In order to create a feasible design that is capable of performing the required mission, the vehicle must be sized from its basic configuration. In [9], Noth presents an integrated sizing model for small solar powered UAVs. His work synthesizes many existing sizing models for sailplanes and seeks to extend their validity to a wider size range of solar powered aircraft. The sizing model presented here draws heavily from the model developed in [9], however, several key differences arise when considering both the form and desired functionality of the proposed vehicle.

The desire for efficient flight typically results in sailplanes with large aspect ratios. This trend is evident in [9] where aspect ratios as large as 40 are cited. However, the resulting large wingspans are not appropriate for navigating through cluttered near earth environments and impose undesirable spatial constraints on takeoff and landing. In addition to the disadvantages of their size, high aspect ratio wings are less rigid than lower aspect ratio wings. This can cause undesirable aeroelastic effects at higher speeds or when subjected to the high aerodynamic loads required to perform agile maneuvers.

A model was developed in order to determine the optimal sizing of a vehicle with the proposed configuration and capable of achieving the desired mission. The primary objective of the model is to identify the design that minimizes vehicle size and mass.

Additional vehicle performance metrics such as stall speed, maximum level flight speed, charge time, and mission duty cycle are considered.

The input to the model over which the design space is assessed is the wing aspect ratio. The model encompasses a solar irradiance model to account for the required energy harvesting, an aerodynamics and propulsion model to determine the vehicle energy expenditure, and a mass model.

3.2 Energy Model

3.2.1 Solar Irradiance

Incoming solar irradiance varies considerably with the current date, time, and location. Over the course of a year, the changing distance from the earth to the sun results in a variation of 6.6% in terrestrial irradiance [30]. The total solar irradiance arriving at the mean Sun-Earth distance has been measured by the Solar Radiation and Climate Experiment satellite project with a highly accurate Total Irradiance Monitor to be approximately 1361 W/m^2 [31]. This energy is further attenuated by the atmosphere to an average of about 1000 W/m^2 on a clear day at a sea-level location perpendicular to the the Sun's rays . Additional cloud cover or atmospheric haze can significantly reduce the energy absorbed or reflected by the atmosphere. Variation in latitude or surface orientation further reduce the irradiance on a given surface. This results in additional seasonal variations in available irradiance due to the tilt of the earth's axis.

The sinusoidal model of terrestrial solar irradiance shown in Equation 3.1 has been demonstrated to be accurate for horizontal flat surfaces for a given time, t , from sunrise with a duration of Δt_{day} [30] between sunrise and sunset. This model assumes a maximum terrestrial irradiance, I_{max} of 1000 W/m^2 . The scaling parameter $k_{att} \leq 1$ allows for modeling of additional atmospheric attenuation. Assuming that the orientation of the solar cells remains approximately constant and that the vehicle remains in approximately the same geographic location, Equation 3.1 can be used to

model the solar irradiance received at the cells.

$$I = \begin{cases} I_{max} k_{att} \sin\left(\frac{t}{\Delta t_{day}}\pi\right) & 0 \leq t \leq \Delta t_{day} \\ 0 & otherwise \end{cases} \quad (3.1)$$

The total energy received by the cells during a day can be found by integrating Equation 3.1 from t_{start} to $\Delta t_{day} - t_{end}$, and multiplying by the wing planform area S and a scaling constant q_{fill} which indicates the proportion of the wing surface that is covered by solar cells where t_{start} and t_{end} represent the amount of time after sunrise and before sunset when the cells are not collecting energy such that,

$$I_{day} = \frac{I_{max} \Delta t_{day} k_{att}}{\pi} \left(\cos \frac{t_{start}}{\Delta t_{day}} - \cos \frac{\Delta t_{day} - t_{end}}{\Delta t_{day}} \right) S q_{fill} \quad (3.2)$$

Before it can be used or stored, the energy received by the solar cells must be converted into a usable form. In order to achieve the maximum power output from the cells, a maximum power point tracker (MPPT) must be used to regulate the voltage of the cells. The efficiencies of both the MPPT and the solar cells, η_{MPPT} and η_{cell} are used to scale the total solar energy received at the cells.

3.2.2 Aerodynamics

Only the aerodynamics of the wing are considered in the performance model. The design is essentially a flying wing and the interaction between the propeller slipstreams and the wing are neglected.

The wing lift and drag can be expressed by

$$L = \frac{1}{2} C_L \rho S V_\infty^2 \quad (3.3)$$

and

$$D = \frac{1}{2} C_D \rho S V_\infty^2 \quad (3.4)$$

where C_L and C_D are the lift and drag coefficients of the wing respectively, ρ is the

air density, and V_∞ is the free-stream velocity.

The drag coefficient can be expanded as a drag polar consisting of a parasite drag component, C_{D_0} , and an induced drag component as

$$C_D = C_{D_0} + \frac{C_L^2}{\pi e_O AR} \quad (3.5)$$

where e_O is the wing Oswald's efficiency factor and AR is the wing aspect ratio. Equation 3.6 gives an approximation for e_O , parametrized on the aspect ratio and the leading edge wing sweep Λ_{LE} . This estimate is a curve fit from wind tunnel data compiled for a variety of wing and body configurations [32].

$$e_O \approx 4.61 (1 - 0.045 AR^{0.68}) (\cos \Lambda_{LE})^{0.15} - 3.1 \quad (3.6)$$

In steady, level flight

$$W = L \quad (3.7)$$

where W is the weight of the vehicle. As a result,

$$D = W \frac{C_D}{C_L} \quad (3.8)$$

The power required by the propulsive system in this operating condition is given by

$$P_{cruise} = \frac{1}{\eta_{motor} \eta_{prop}} T V_\infty \quad (3.9)$$

where T is the thrust required and η_{motor} and η_{prop} are the efficiencies of the motor and propeller respectively. Setting the required thrust equal to the vehicle drag and solving Equations 3.9, 3.7, and, 3.3 for the cruise speed gives the total power required during cruise flight as

$$P_{cruise} = \frac{1}{\eta_{motor} \eta_{prop}} W \left(\frac{W}{S} \right)^{1/2} \left(\frac{C_D}{C_L^{3/2}} \right) \left(\frac{2}{\rho} \right)^{1/2} \quad (3.10)$$

If the motor and propulsive efficiencies are assumed to be constant, Equation 3.10

indicates that, for a given configuration, the cruise power is proportional to the ratio $\frac{C_D}{C_L^{3/2}}$. Using Equation 3.5, the minimum $\frac{C_D}{C_L^{3/2}}$ can be found to occur when $3C_{D_0} = \frac{C_L^2}{\pi e O A R}$. Substituting this result back into Equations 3.3 and 3.7 gives the lowest power cruise speed to be

$$V_{min P} = \left(\frac{2W}{\rho S} \sqrt{\frac{1}{3C_{D_0}\pi e O A R}} \right)^{1/2} \quad (3.11)$$

The cruise speed must be lower bounded by the vehicle stall speed which can be determined by

$$V_{stall} = \sqrt{\frac{2W}{\rho S C_{L_{max}}}} \quad (3.12)$$

Thus, at the optimal cruise speed, the power required is given by

$$P_{cruise} = \frac{1}{\eta_{motor}\eta_{prop}} W \left(\frac{W}{S} \right)^{1/2} a_{aero} \quad (3.13)$$

where

$$a_{aero} = \max \left(\frac{4C_{D_0}^{1/4}}{(3\pi e O A R)^{3/4}}, \frac{C_{D_0} + \frac{C_{L_{max}}^2}{\pi e O A R}}{C_{L_{max}}^{3/2}} \right) \left(\frac{2}{\rho} \right)^{1/2} \quad (3.14)$$

The maximum level flight speed can be found by solving

$$P_{avail} = TV = DV = \frac{1}{2} \rho S C_D V^3 \quad (3.15)$$

3.2.3 Propulsion

The requirement for vertical takeoff and landing drives the maximum power that the motors must be capable of supplying. During the takeoff, initial climb, descent, and landing phases, the rotors will be in a near static load condition where total thrust is approximately equal to the vehicle weight. For a static rotor, conservation of momentum at the rotor plane yields

$$T_{static} = \frac{\pi \rho D^2}{8} \Delta v^2 \quad (3.16)$$

where D is the rotor diameter and Δv is the exit velocity of the air in the stream tube. The power created by the rotor is similarly given by

$$P_{static} = T_{static} \frac{\Delta v}{2} \quad (3.17)$$

Solving Equation 3.17 for Δv and substituting into Equation 3.16 gives an expression for the power required as a function of the rotor diameter, the air density, and the required thrust. In order to take into account the dual rotor system, the total required thrust must be divided in half and the resulting power required doubled. Dividing by the motor and propeller efficiencies results in the total required power input to both of the motors.

$$P_{static} = \frac{2}{\eta_{motor}\eta_{prop}} \sqrt{\frac{T_{static}^3}{4\pi\rho D^2}} \quad (3.18)$$

Equation 3.18 can be used to size the motors by setting the thrust equal to the weight multiplied by the desired thrust to weight ratio. Although this sizing constraint results in much larger motors than required for level, unaccelerated flight, the additional weight penalty is somewhat offset by the fact that electric motors are typically most efficient at one half to one third of their maximum power [33]. The efficiency losses of the motor electric speed controllers (ESCs) are included in the overall motor efficiency estimate.

3.2.4 Summary

The energy produced by the solar cells at a given time t after sunrise is can be estimated by

$$P_{cells} = \eta_{mppt}\eta_{cell}I_{max}k_{att}S q_{fill} \sin\left(\frac{t}{\Delta t_{day}}\pi\right) \quad (3.19)$$

Integrating Equation 3.19 over the time period from t_{start} to t_{end} gives the total energy supplied by the cells to be

$$E_{cell} = \eta_{mpp} \eta_{cell} \frac{I_{max} k_{att} S q_{fill} \Delta t_{day}}{\pi} \left(\cos \frac{t_{start}}{\Delta t_{day}} \pi - \cos \frac{\Delta t_{day} - t_{end}}{\Delta t_{day}} \pi \right) \quad (3.20)$$

At the optimal cruise speed, the power required for level flight is

$$P_{cruise} = \frac{1}{\eta_{motor} \eta_{prop}} W \left(\frac{W}{S} \right)^{1/2} a_{aero} \quad (3.21)$$

The maximum power required from each motor can be found by

$$P_{motor} = \frac{1}{\eta_{motor} \eta_{prop}} \sqrt{\frac{(c_T W)^3}{4\pi\rho D^2}} \quad (3.22)$$

where c_T is the desired thrust to weight ratio.

3.3 Mass Model

3.3.1 Solar Cells

The mass of the solar cells was estimated through a linear mass coefficient of 32 mg/cm^2 taken from specifications for high performance AzurSpace S32 silicon solar cells [34]. An additional mass of 16 mg/cm^2 is included in the solar cell mass estimate to account for materials required to encapsulate and protect the cells on the wing. The mass of the maximum power point tracker was estimated as proportional to the maximum power delivered by the cells with a coefficient of 422 mg/W .

3.3.2 Airframe

It is common practice in aircraft design to estimate the vehicle airframe mass through curve fits of data from similar existing aircraft [32, 35]. In [9], Noth extends several existing mass models by performing a least squares fit on data from more than 400 sailplanes including both manned and unmanned vehicles. The model used, is a

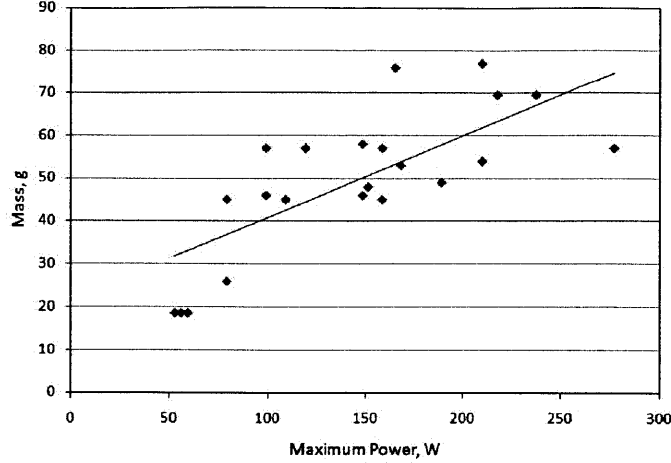


Figure 3-1: Electric motor mass and maximum power for several high end brushless hobby motors

function of the wing aspect ratio and planform area and gives the vehicle mass, in kg, as

$$m_{af} = k_{struct} S^{x_1} AR^{x_2} \quad (3.23)$$

When evaluated over only the lightest 20% of aircraft, the exponents x_1 and x_2 were found to be 1.55 and 1.21 respectively and the linear scaling term was 0.0795

3.3.3 Propulsion System

Data from approximately 50 high performance brushless electric hobby motors was compiled and, as shown in Figure 3-1, a linear regression was used to correlate the motor mass and maximum power for all of the motors less than 300 W. This regression resulted in a motor mass given by

$$m_{motor} = 0.192 \text{ kg/kW} P_{motor} + 0.022 \text{ kg} \quad (3.24)$$

The linear coefficient in this regression is smaller than that presented in [9] from a similar study. However, in [9] the data was fit over a much wider range of motor powers and a zero intercept was imposed. The non-zero intercept and smaller power range ensure a better fit about the region of interest.

In [9], a linear propeller mass model of 0.25kg/kW is used to estimate the propeller

mass as a function of the motor power. Here a value of 0.10kg/kW will be used to account for the relatively lighter weight of small composite hobby propellers compared to larger propellers.

Similarly, the mass coefficient of 0.06kg/kW obtained in [9] from 170 optimized ESCs is used to estimate the mass requirement of the controller for each motor.

3.3.4 Avionics

The aircraft avionics are assumed to remain fixed with vehicle size. The mass contribution for the vehicle avionics is estimated as the sum of the controller, sensor, and actuator masses. For sizing purposes, the assumed sensors include an inertial measurement unit (IMU), GPS, ultrasonic range finder, differential pressure sensor, and an absolute pressure sensor. Using data from commercially available components results in an avionics mass estimate of 150 g.

3.3.5 Battery

The battery mass is assumed to be proportional to the required storage capacity with a specific energy of 1.75mg/J , which is a typical value for model aircraft lithium polymer batteries [36].

3.3.6 Summary

The total vehicle mass is given by

$$m = m_{af} + m_{cell} + m_{mppt} + 2m_{motor} + 2m_{prop} + 2m_{ESC} + m_{bat} + m_{av} + m_{payload} \quad (3.25)$$

where the component masses are approximated by

$$m_{af} = k_{struct} S^{1.55} AR^{1.21} \quad (3.26)$$

$$m_{cell} = (k_{cell} + k_{encap}) S q_{fill} \quad (3.27)$$

$$m_{mppt} = k_{mppt} \eta_{cell} I_{max} S q_{fill} \quad (3.28)$$

$$m_{motor} = k_{motor1}P_{motor} + k_{motor0} \quad (3.29)$$

$$m_{prop} = k_{prop}P_{motor} \quad (3.30)$$

$$m_{ESC} = k_{ESC}P_{motor} \quad (3.31)$$

$$m_{bat} = k_{bat}E_{bat} \quad (3.32)$$

and the linear mass coefficients k_{struct} , k_{cell} , k_{encap} , k_{mppt} , k_{motor0} , k_{motor1} , k_{prop} , k_{ESC} , and k_{bat} take the values specified in the text.

3.4 Sizing Constraints

Given a specified time interval t_{start} after sunrise, the vehicle is sized to give continuous flight from t_{start} hours after sunrise to t_{start} hours before sunset with no charging assumed to occur while the vehicle is not flying. Applying a power balance with Equations 3.20 and 3.13 results in the constraint

$$E_{cell} - P_{cruise}(\Delta t_{day} - 2t_{start}) = 0 \quad (3.33)$$

Given a vehicle weight and configuration, the required wing surface area is

$$S = a_S m \quad (3.34)$$

where

$$a_S = g \left[\frac{a_{aero}\pi}{\eta_{tot} I_{max} k_{att} q_{fill}} \left(1 - \frac{2t_{start}}{\Delta t_{day}} \right) \left(\cos \frac{t_{start}}{\Delta t_{day}}\pi - \cos \frac{\Delta t_{day} - t_{start}}{\Delta t_{day}}\pi \right)^{-1} \right]^{2/3} \quad (3.35)$$

and

$$\eta_{tot} = \eta_{motor}\eta_{prop}\eta_{mppt}\eta_{cell} \quad (3.36)$$

Setting the propeller diameter to one fourth of the wingspan and noting that the wingspan is related to the planform area and aspect ratio by $b = \sqrt{ARS}$, Equation 3.34 can be substituted into Equation 3.22 to give the required power of each

motor as a function of the vehicle weight such that

$$\begin{aligned} P_{motor} &= \frac{2}{\eta_{motor}\eta_{prop}} \sqrt{\frac{(c_T W)^3}{\pi \rho A R S}} \\ &= \frac{2}{\eta_{motor}\eta_{prop}} \sqrt{\frac{(c_T g)^3}{\pi \rho A R a_S}} m = a_m m \end{aligned} \quad (3.37)$$

where

$$a_m = \frac{2}{\eta_{motor}\eta_{prop}} \sqrt{\frac{(c_T g)^3}{\pi \rho A R a_S}} \quad (3.38)$$

Since the cruise energy demand is constant throughout the day, there will be periods of time where the energy demand is greater than the energy supplied by the solar cells. As shown in Figure 3-2, this deficit will be accounted for by the battery. The battery is sized with a capacity that will allow it to provide the deficit power needed for an entire day. From Equations 3.19 and 3.13 the time after sunrise where the power supplied by the cells first equals the power demanded by the propulsion system is,

$$\begin{aligned} t_{break} &= \arcsin \left(\frac{1}{\eta_{tot} I_{max} k_{att} S q_{fill}} W \left(\frac{W}{S} \right)^{1/2} a_{aero} \right) \frac{\Delta t_{day}}{\pi} \\ &= \arcsin \left(\frac{1}{\eta_{tot} I_{max} k_{att} q_{fill}} \left(\frac{g}{a_S} \right)^{3/2} a_{aero} \right) \frac{\Delta t_{day}}{\pi} \end{aligned} \quad (3.39)$$

Integrating Equations 3.19 and 3.13 from t_{start} to t_{break} and taking twice the difference between the two integrals gives the required battery capacity. An additional scaling factor c_{bat} is used to provide an energy storage margin.

$$E_{bat} = a_{bat} m \quad (3.40)$$

where

$$a_{bat} = 2c_{bat} \left[\frac{1}{\eta_{motor}\eta_{prop}} g^{3/2} \left(\frac{1}{a_S} \right)^{1/2} a_{aero} (t_{break} - t_{start}) \right]$$

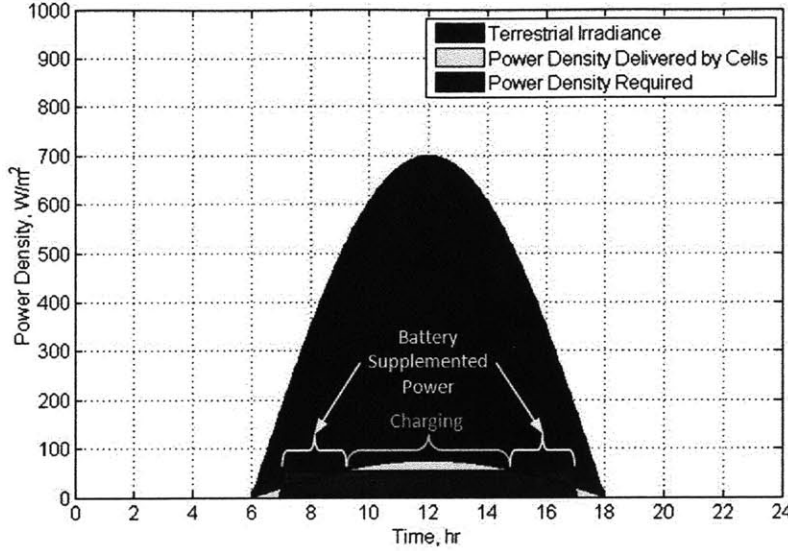


Figure 3-2: Solar model with power demand

$$-\eta_{mpp} \eta_{cell} \frac{I_{max} \Delta t_{day} k_{att} q_{fill}}{\pi} a_S \left(\cos \frac{t_{start}}{\Delta t_{day}} \pi - \cos \frac{t_{break}}{\Delta t_{day}} \pi \right) \quad (3.41)$$

Substituting Equations 3.34, 3.37, and 3.40 into Equations 3.26 through 3.32 and solving Equation 3.25 for the total vehicle mass gives

$$a_2 m^{1.55} + a_1 m + a_0 = 0 \quad (3.42)$$

where

$$a_2 = k_{struct} a_S^{1.55} A R^{1.21} \quad (3.43)$$

$$\begin{aligned} a_1 &= (k_{cell} + k_{encap} + k_{mpp} \eta_{cell} I_{max}) q_{fill} a_S \\ &\quad + 2 (k_{motor1} + k_{prop} + k_{ESC}) a_m + k_{bat} a_{bat} - 1 \end{aligned} \quad (3.44)$$

and

$$a_0 = 2k_{motor0} + m_{av} + m_{payload} \quad (3.45)$$

Solving 3.42 for the first positive, real root gives the lowest feasible vehicle mass.

3.5 Analysis

Equation 3.42 was solved for aspect ratios varying from 1 to 10. The day was assumed to be 12 hours long and the flight was defined as beginning and ending one hour after sunrise and one hour before sunset respectively. Table 3.1 lists the values of all parameters used in the sizing process. These values were held fixed for all of the runs.

Figure 3-3 shows the results of the sizing analysis. In Figure 3-3(a) the wing geometry parameters of span and planform area are plotted against aspect ratio. Although the total wing planform area decreases as aspect ratio increases for aspect ratios of approximately 7 or less, the wingspan increases with aspect ratio for all aspect ratios greater than two. In Figure 3-3(b), it can be similarly noted that smaller aspect ratio wings tend to provide advantages in terms of their lower stall speeds and higher maximum speeds.

It is interesting to note that, with the exception of the smallest aspect ratios, the cruise velocity for minimum power consumption was limited by the stall speed of the aircraft. Optimized airfoil designs would allow for slower stall speeds which would result in improved performance by flying slower. Such a change would likely favor the larger aspect ratio wings more than the smaller aspect ratio wings since the stall speed tends to increase with aspect ratio.

The cumulative mass distribution of the vehicle is plotted in Figure 3-3(c) against aspect ratio. The total vehicle mass drops rapidly with aspect ratio for very small aspect ratio wings. However, the total mass varies by less than 10% for all aspect ratios between 3 and 10. This trend is very similar to the change in planform area shown in Figure 3-3(a). The most significant changes in mass between different aspect ratio designs can be seen to come from the battery and the structure. However, while the battery mass decreases with aspect ratio to account for more efficient flight characteristics, the airframe mass must increase to support the larger structure,

Since the change in mass is minimal for all aspect ratios above 3, the wingspan and flight performance will drive the design. In both the cases, smaller aspect ratio

Table 3.1: Sizing parameters

Parameter	Description	Units	Value
<i>Solar Model</i>			
I_{max}	maximum solar irradiance	W/m ²	1,000
Δt_{day}	length of day	hr	12
t_{start}	no fly duration after sunrise and before sunset	hr	1
k_{att}	atmospheric attenuation factor	-	0.7
q_{fill}	solar cell wing fill ratio	-	0.8
η_{cell}	solar cell efficiency	-	0.169
η_{mppt}	MPPT efficiency	-	0.95
<i>Aerodynamics Model</i>			
C_{D_0}	parasitic drag coefficient	-	0.05
$C_{L_{max}}$	maximum lift coefficient	-	1.0
<i>Propulsion Model</i>			
c_T	thrust to weight ratio	-	1.5
η_{motor}	motor efficiency	-	0.8
η_{prop}	propeller propulsive efficiency	-	0.6
<i>Mass Parameters</i>			
k_{struct}	airframe mass coefficient	-	0.0795
k_{cell}	solar cell mass coefficient	mg/cm ²	32.0
k_{encap}	solar cell encapsulation mass coefficient	mg/cm ²	16.0
k_{mppt}	MPPT mass coefficient	mg/W	422.0
k_{motor0}	motor mass offset	kg	0.022
k_{motor1}	motor mass coefficient	kg/kW	0.192
k_{prop}	propeller mass coefficient	kg/kW	0.10
k_{esc}	electric speed control mass coefficient	kg/kW	0.06
k_{bat}	battery mass coefficient	mg/J	1.75
m_{av}	avionics mass	kg	0.150
$m_{payload}$	payload mass	kg	0.150
c_{bat}	battery margin	-	1.5
<i>Physical Constants</i>			
ρ	air density	kg/m ³	1.225
g	gravitational acceleration	m/s ²	9.81

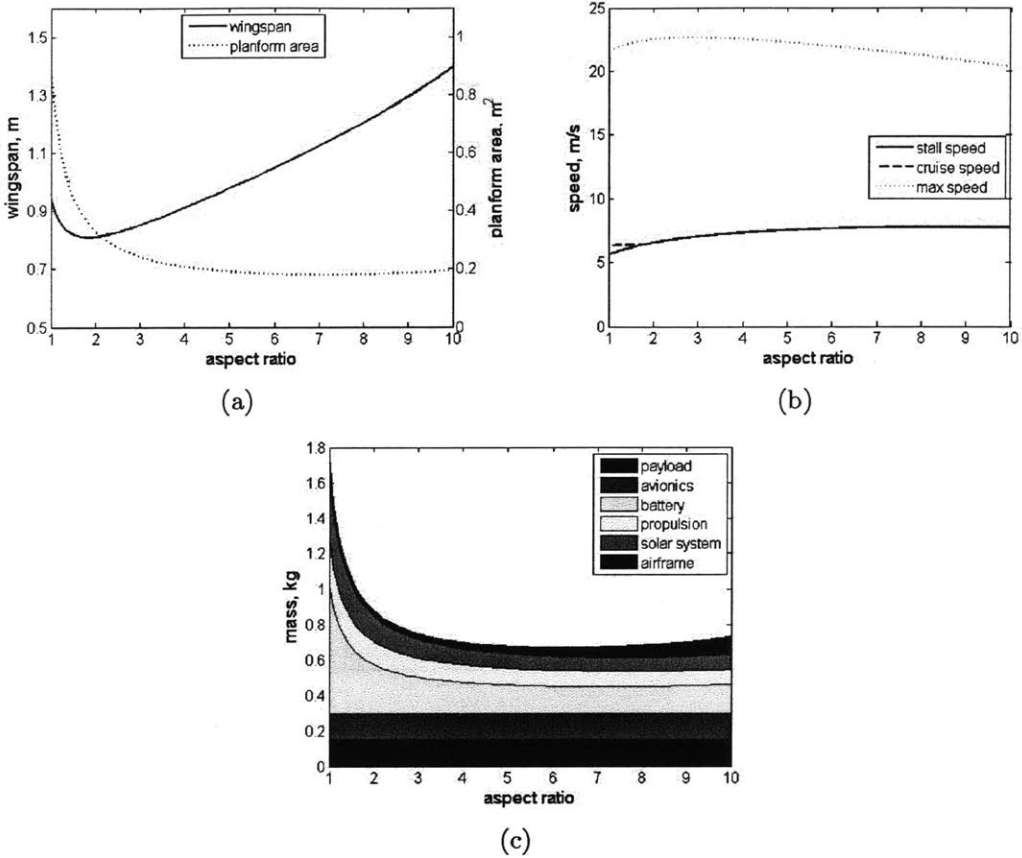


Figure 3-3: Sizing results. Wing geometry (a), vehicle performance (b), and mass distribution (c)

designs exhibit more desirable characteristics. Additionally, at such low flight speeds, lower aspect ratio wings will have higher Reynolds number flow characteristics. The flight performance of micro air vehicles has been shown to rapidly decrease as the Reynolds number decreases [33]. As a result, the design will be sized with an aspect ratio of 3. The sizing results for a vehicle with an aspect ratio of 3 are presented in Table 3.2.

Figure 3-4 shows the flight time, charge time, and duty cycle for the configuration specified in Tables 3.1 and 3.2 under various solar conditions. At around 500 W/m^2 of received irradiance, the solar cells are able to supply all of the power needed by the propulsion system to maintain continuous flight. Below this level, the duty cycle approaches zero approximately linearly with irradiance level. At 500 W/m^2 , the battery would require 2.06 hrs to fully charge from empty. At 1000 W/m^2 , the required charge

Table 3.2: Sizing results for $AR = 3$

Parameter	Units	Value
m_{af}	kg	0.033
m_{cell}	kg	0.093
m_{mppt}	kg	0.014
m_{motor}	kg	0.040
m_{prop}	kg	0.009
m_{esc}	kg	0.006
m_{bat}	kg	0.201
m	kg	0.750
S	m^2	0.242
b	m	0.852
V_{stall}	m/s^2	7.04
V_{cruise}	m/s^2	7.04
V_{max}	m/s^2	22.64
P_{motor}	W	91.22
E_{bat}	kJ	115.11

time is only 1.03 hrs.

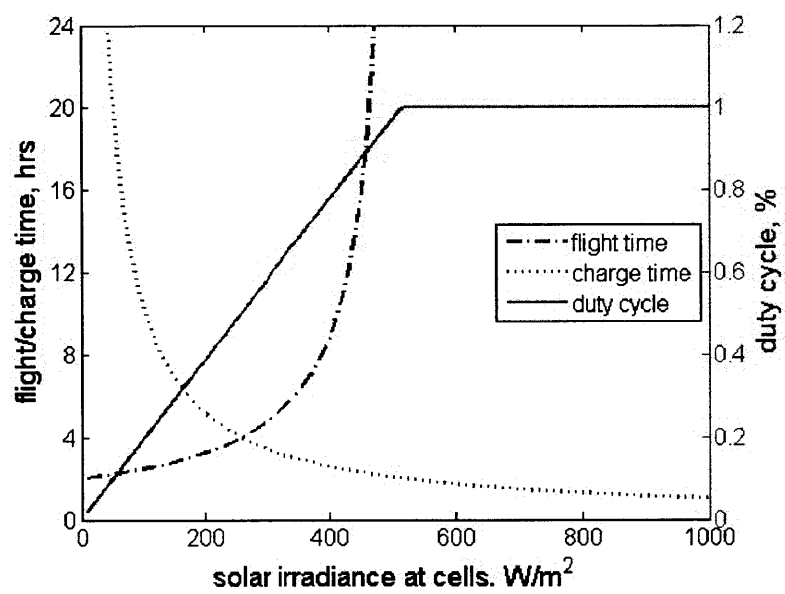


Figure 3-4: Flight endurance, charge time, and duty cycle for a sized vehicle with $AR = 3$

THIS PAGE INTENTIONALLY LEFT BLANK

Chapter 4

Prototype Vehicle Design

The prototype vehicles, shown in Figure 4-1 were designed and built to demonstrate the capability of the proposed vehicle to accomplish the takeoff maneuver from diverse, unknown terrain and stabilize itself in hovering flight. The prototypes are sized based on the analysis presented in Chapter 3. However, since the vehicles are intended only as proofs of concept, the aerodynamics and structural components are not optimized. The wing is a flat plate and the structure is overbuilt to provide improved survivability. The overbuilt structure results in an increased vehicle mass that is offset by the lack of solar cell and payload masses. A final design would include an optimized airfoil and structural design that would improve flight performance and reduce the vehicle mass.

4.1 Tilt Rotor Aircraft Design Issues

Tilt rotor aircraft concepts have been recorded from as early as the early 1920's when Henry Berliner designed and built a tilt-propeller helicopter that was capable of partially rotating its rotors forward for increased flight speeds. Since then, a number of tilt rotor aircraft designs have been proposed or implemented with varying degrees of success [37]. Nevertheless, only since the 1980s, with the development and military integration of the V-22 Osprey, have tilt rotor designs been viewed as a viable option for aircraft designs. Since then, a number of disastrous mishaps have resulted

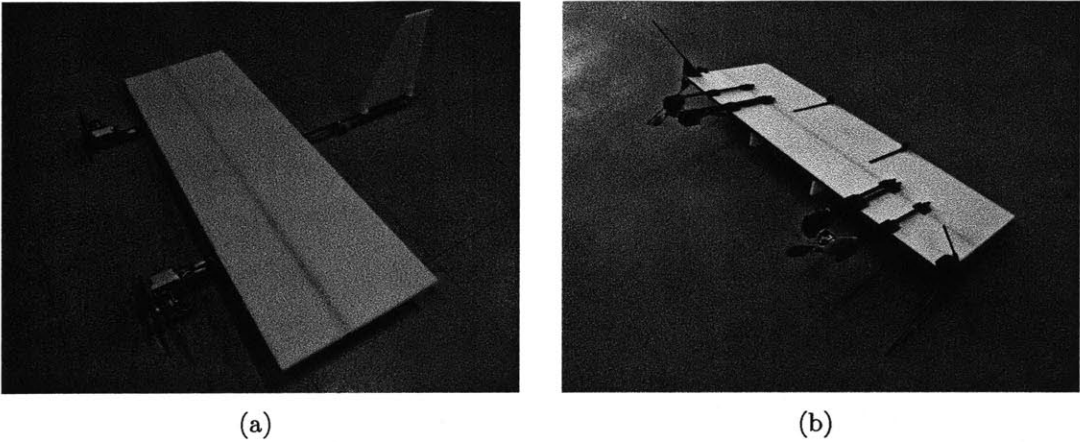


Figure 4-1: Prototype vehicles: Initial prototype with single boom mounted vertical stabilizer (a), Second prototype with in-wing, pivoting vertical stabilizers (b).

in widespread controversy over their use in manned applications [38].

In most tilt rotor designs, the rotors are located longitudinally near the vehicle center of gravity. This placement is typically driven by the practical requirement of mounting the motors on the front of the wings and a desire to allow the vehicle to remain in a horizontal orientation during hover. However, placement near the center of gravity results in short moment arms which limit the pitch control authority that can be achieved through rotor articulation. Typical control strategies for such vehicles utilize cyclic blade controls to augment or replace rotor articulation as the primary pitch control effector [39]. Although it has been proven to be effective in several designs, this approach adds considerable mechanical complexity to the design and increases the number of moving parts and maintenance demands of the aircraft.

Other tilt rotor designs include three or more rotors, veined ducts, or exhaust vents to achieve improved control authority while in vertical flight [40]. An opposed lateral tilting mechanism is proposed in [41] which articulates the rotors about both the lateral and longitudinal axes in order to achieve additional pitch control through the gyroscopic moments created by articulating the rotors.

In [18], the opposed lateral tilting mechanism is demonstrated successfully with a back stepping controller in a 6 degrees of freedom nonlinear simulation. Nevertheless, as with cyclic blade control, all of these approaches increase the complexity of the system and still tend to have limited or insufficient control authority [41, 42].

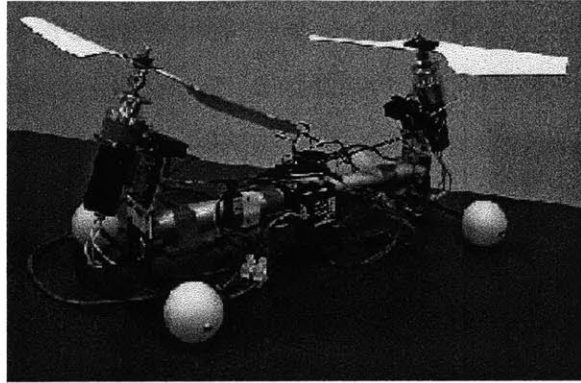


Figure 4-2: Opposed lateral tilting prototype presented in [18].

In a long endurance, persistent operation scenario it is imperative to have a design that is capable of sustained operation without servicing or maintenance. A simple mechanical design with few moving parts will reduce the potential failure modes of any proposed design. Furthermore, the limited attitude control authority of most existing tilt rotor aircraft could hinder their ability to takeoff or land effectively from diverse, unprepared terrains where the surface orientation may be far from level.

In addition to utilizing gyroscopic torques, the opposed lateral tilting design shown in Figure 4-2 also improves the pitch control authority by increasing the moment arm of the vectored thrust system by elevating the rotors above the center of gravity [18]. While this configuration provides a significant improvement in control authority, it is not practical for implementation in a fixed wing vehicle capable of forward flight. The vehicle design proposed here modifies this approach by extending the rotors in front of the wing and allowing the vehicle to pitch up to a vertical orientation during the takeoff maneuver.

During takeoff and hover, the extended distance between the center of gravity and the rotor articulation point allows for sufficient pitch control authority with articulation only about the longitudinal axis. Similarly, the outboard location of the rotors along the span of the wings allows for adequate yaw control through differential throttle inputs to the motors and roll control through differential articulation of the rotors. This design eliminates the need for cyclic blade control and relies only on articulation about a single axis, thus providing a simple design.

Rather than gradually transitioning the rotors from a hovering to a level flight configuration, the proposed design will allow for transition from hover to level flight by pitching the vehicle forward with a gradual increase in collective throttle to account for the reduction in vertical thrust as the vehicle builds forward speed. Returning to hover is similarly accomplished by pitching the vehicle up and increasing the collective throttle so that the thrust is equal to the vehicle weight. This technique has been demonstrated successfully in a number of prop-hanging fixed wing vehicles [29, 43–45].

The proposed design also allows for vectored thrust from the rotors to be used for attitude control during both hovering and level flight. A similar approach to control during level flight has been demonstrated on the Aurora Flight Sciences Skate [28]. Since no additional actuators are required, this approach reduces the vehicle weight and allows the vehicle to quickly recover into either flight mode. Unlike vehicles with aerodynamic control surfaces, the use of articulated thrust further prevents the vehicle from losing control authority during spins or other stalled maneuvers.

Finally, the small size, low wing loading, and slow flight speeds that results from the sizing considerations presented in Chapter 3 will help to preclude the aeroelastic instabilities that are often present in larger tilt rotor designs.

4.2 Airframe and Aerodynamics

4.2.1 Wing and structure

Based on the sizing analysis in Section 3.5, a rectangular planform with a chord length of 280 mm and a span of 840 mm was chosen, giving a total planform area of 0.235 m^2 which is within 3% of the sized area presented in Table 3.2. The wing was constructed from 9 mm thick depron foam.

Carbon fiber tube was inlaid in the wing at 40% of the chord length (112 mm) from the leading edge. Similarly, a carbon fiber bar was glued to the leading edge to add rigidity to the wing and protect the foam from denting. In the second prototype

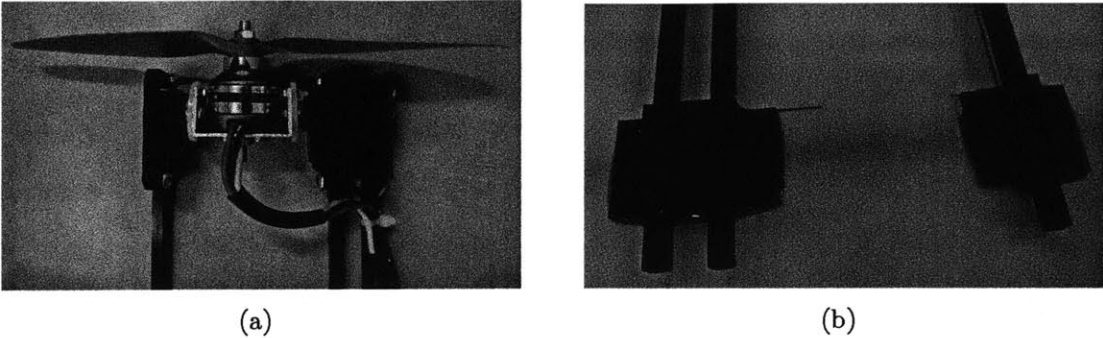


Figure 4-3: Motor pivots (a) and support attachments (b).

a second bar was also glued to the trailing edge.

Each motor is mounted directly to a servo on one side and to a ball bearing pivot on the other. Testing showed that cantilevering the motor off of the servo only would result in large amplitude oscillations that would damage the servos. The servo and pivot mounts, shown in Figure 4-3(a), are supported by square carbon fiber tubes. The supports are attached to the wing by a series of set screws in ABS plastic mounts that are epoxied onto the wing as depicted in Figure 4-3(b).

The motors are positioned 165 mm from each wingtip. Locating the motors near the wingtips creates a helical flow over the outer wing sections. By selecting the propeller rotation direction, this flow can be used to counteract wingtip vortices, thus reducing induced drag. Additionally, in [46] it was shown that for low aspect ratio wings where the rotor diameter is a significant portion of the wingspan, the increased airflow over the wing assists in increasing the wing lift coefficient and delaying stall. However, this benefit may come at the cost of additional drag [46].

With the motors located near the wingtips, any potential optical sensor payloads would have a clear field of view to the front of the aircraft. Furthermore, locating the fuselage and main components near the center of the wing moves them out of the rotor slipstream. This configuration will reduce the profile drag of the fuselage over that of typical configurations with center mounted rotors.

In order to achieve positive static stability about the longitudinal axis, the aerodynamic center of the vehicle must be located aft of the center of gravity. This configuration results in a nose down moment on the aircraft. When cambered air-

foils are used, this nose down moment is further increased by the pitching moment of the wing about its aerodynamic center. In conventional aircraft, this moment is countered by a horizontal stabilizer which provides a small amount of negative lift. Flying wings and tailless aircraft often utilize a reflexed airfoil shape to accomplish the same effect. Both of these techniques effectively increase the amount of lift that the main wing must produce, thereby adding drag and reducing their efficiency.

Similar to canard designs, the proposed design is capable of achieving longitudinal trim in forward flight by offsetting the negative aerodynamic pitching moment with a trust torque by angling the rotors upward. Since the rotors are located in front of the center of gravity, the trim thrust reduces the amount of lift required by the wing. Thus, using the articulating thrust mechanism to trim the aircraft allows for more efficient forward flight than conventional designs.

For the prototype, the aerodynamic center was assumed to be located at 25% of the chord length (70 mm) from the leading edge. The desired stability margin was chosen to be 10%, resulting in a center of gravity located 42 mm behind the leading edge of the wing.

The magnitude of the component of the thrust vector oriented in the lift direction needed for trim or pitch control is inversely proportional to the distance between the rotor pivot locations and the aircraft center of gravity. Thus, the further forward the location of the rotor pivots, the more efficiently control moments can be exerted. Similarly, moving the rotors forward will improve their control authority during hovering flight. In the prototype design, the rotor pivots were located 102 mm in front of the leading edge. This ensures that the wing does not block any of the rotor slipstream when the rotors are fully articulated during takeoff. Moving the rotors further forward made it difficult to achieve the necessary center of gravity location for the desired stability margin.

An additional square carbon fiber tube is mounted to the center of the wing to attach the battery and IMU. As shown in Figure 4-10, the battery is secured to the airframe with two rubber bands to allow it to release in the event of a crash. The IMU and battery mount are attached directly to the carbon fiber tube. All other

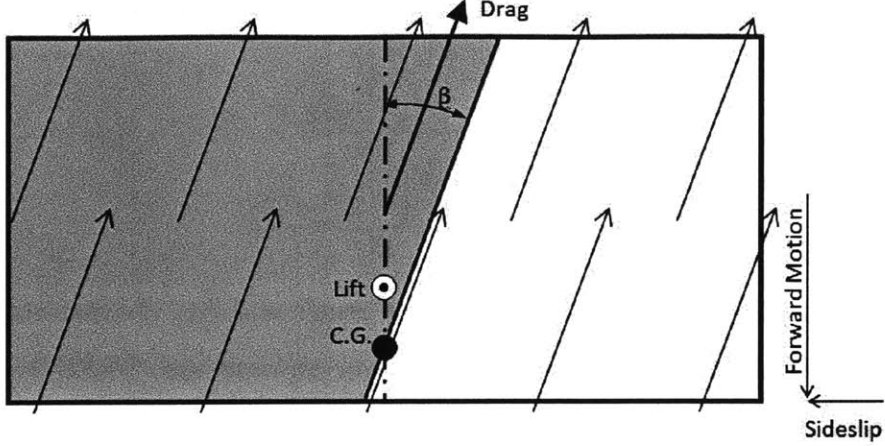


Figure 4-4: Lateral directional stability augmentation of low aspect ratio wings

components are secured to the bottom of the wing surface with either hot glue or Velcro.

The total prototype airframe mass is 338.3g.

4.2.2 Lateral Directional Stability

According to [33], for wings with aspect ratios less than 6, an appreciable amount of lateral directional stability is achieved due to change in area about the center of gravity. As sideslip angle increases, the wing area bounded by a line parallel to the free stream that passes through the center of gravity increases on the side that is angled into the wind. This effect is illustrated in Figure 4-4.

If it is assumed that the center of pressure remains along the center line of the wing at 25% of the chord length from the leading edge and that the drag force acts at the center of the planform, the contribution of the sideslip to the lateral and directional moment coefficients can be estimated as

$$C_l = -\sin \beta \frac{S.M.C_L}{AR} \quad (4.1)$$

$$C_n = \sin \beta \frac{(S.M. + 0.25) C_D}{AR} \quad (4.2)$$

Taking the derivatives of Equations 4.1 and 4.2 and evaluating at the trim condi-

tion with zero sideslip gives the linearized wing contributions to the lateral directional stability derivatives.

$$C_{l_{\beta_{wing}}} = -\frac{S.M. c C_L}{b} \quad (4.3)$$

$$C_{n_{\beta_{wing}}} = \frac{(S.M. + 0.25) c C_D}{b} \quad (4.4)$$

Two vertical tails were added for improved static stability characteristics. Each tail is one quarter of a 240 mm circle made of 3 mm depron foam. The tails are hinged at the bottom of the trailing edge and spring loaded to allow them to rotate through the wing if they encounter an obstacle during the takeoff rotation.

For the sized configuration at the cruise speed determined in Section 3.5, the methods presented in [47] were used to estimate the total lateral stability derivative as -0.0343, the directional stability derivative as 0.0181, and the ratio of directional to lateral stability derivatives as 0.5268 which is within the recommended range of $\frac{1}{3}$ to $\frac{2}{3}$ recommended in [32] for adequate Dutch roll performance.

4.3 Propulsion

The requirement for the motors to operate in close proximity to the ground may result in the rotors spinning while they are very close to rocks or other objects. Accordingly, a complete design would incorporate shrouded propellers. A well designed shrouded propeller would increase the static thrust and hovering efficiencies of the motors, allowing for smaller, lighter motors to be used [48].

An AXI 2208/26 GOLD LINE motor was selected for the prototype vehicle and paired with an APC 8 \times 3.8 slow flyer propeller. The motor has an input power of up to 122.1 W which is 34% larger than the sized motor from Section 3.5 and is rated to a maximum efficiency of 82%. The motor has a wide efficiency peak, maintaining an efficiency of above 74% for throttle inputs of 45-82% throttle. Each motor was paired with a JETI ADVANCE Pro 18A ESC which uses a pulse width modulated (PWM) throttle input signal.

The increased motor size was due partly to a limited motor selection as well as a

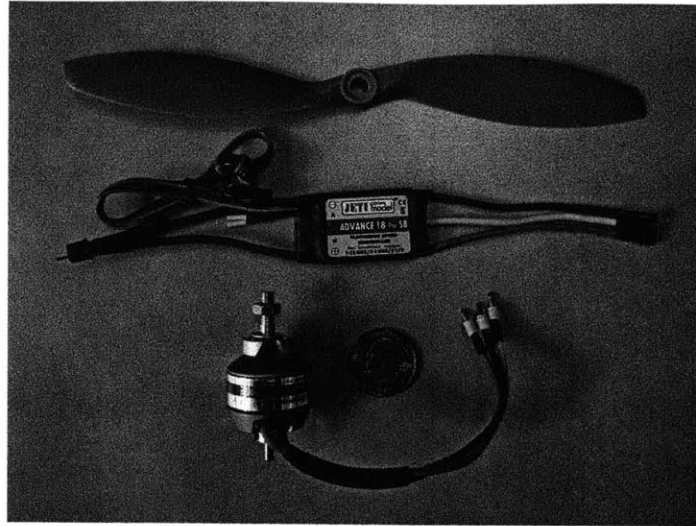


Figure 4-5: Propulsion system components

desire to slightly overpower the vehicle for testing. Using the actual motor power and solving Equation 3.18 for the static thrust gives a predicted maximum static thrust of 1.077 kg. In testing, an actual maximum thrust of 1.158 kg was observed. Thus, the model is within 7% of the observed performance for the selected motors.

Each motor weighs 51.4 g with connectors and prop adapter. Each propeller weighs 7.2 g, and each ESC weighs 25.8 g with connectors. The total propulsion system mass is 168.8 g. Figure 4-5 shows the complete propulsion system setup.

4.4 Power

The sized battery energy capacity from Section 3.5 was 115.11 kJ. Since the prototype will not be flown with energy harvesting capabilities, a smaller 53.95 kJ Thunder Power RC G4 Pro Lite V2 20C 1350mAh 11.1V 3 Cell Lithium Polymer battery was used. The battery, weighs 98 g with connectors. An 11g Castle Creations 10 amp switching power regulator is used to regulate the battery output voltage to 5.5 V. The battery and regulator are shown in Figure 4-6.

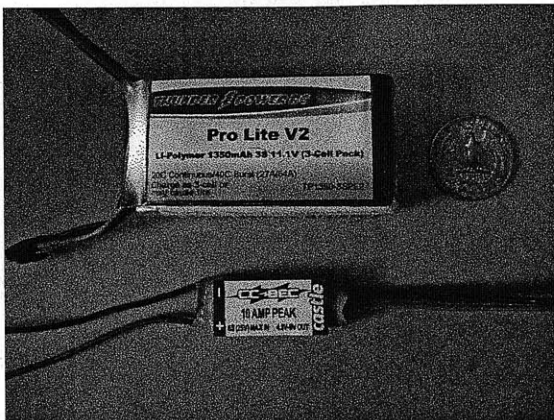


Figure 4-6: Prototype power system

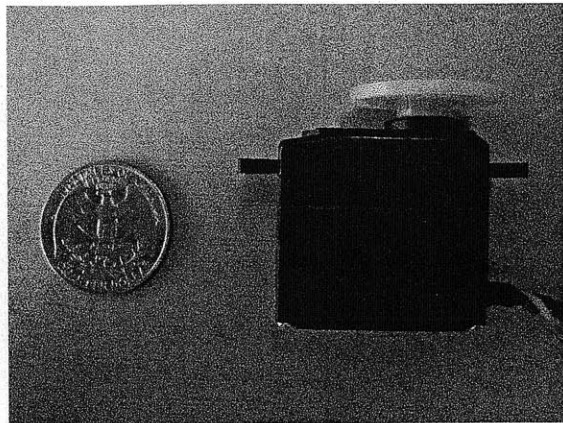


Figure 4-7: Hitec HS-5245MG servo

4.5 Avionics

4.5.1 Actuators

Hitec HS-5245MG metal gear servos were selected to articulate the prototype motors. The servos are rated for a maximum torque of 5.5 kg/cm and a maximum no-load speed of 8.73 rad/sec at 6 V. The servos take a PWM input from $900 \mu\text{sec}$ to $2100 \mu\text{sec}$ and vary the angular position of the output shaft linearly with the input signal from 0 to $\pi \text{ rad}$. The servos, shown in Figure 4-7, weigh 31.8 g each with connectors.

4.5.2 Sensors

The prototype state estimation sensors include an 11.5 g MicroStrain 3DM-GX3-25OEM inertial measurement unit (IMU) for attitude sensing, a 6 g MaxBotix XL-MaxSonar-AE2 ultrasonic rangefinder for hovering altitude detection, and a simple voltage divider circuit to monitor battery voltage. The prototype also includes a 4.3 g Spektrum AR6110E Microlite 6-Channel DSM2 receiver for receiving control inputs from an RC transmitter and an XBee-PRO 900 extended range module for telemetry output and communication with the ground station.

The IMU, shown in Figure 4-8(a), includes three axis accelerometers, rate gyros, and magnetometers. The sensors are sampled and digitally filtered at 30 kHz. Coning and sculling integrals are computed at 1 kHz. The IMU is configured to output a

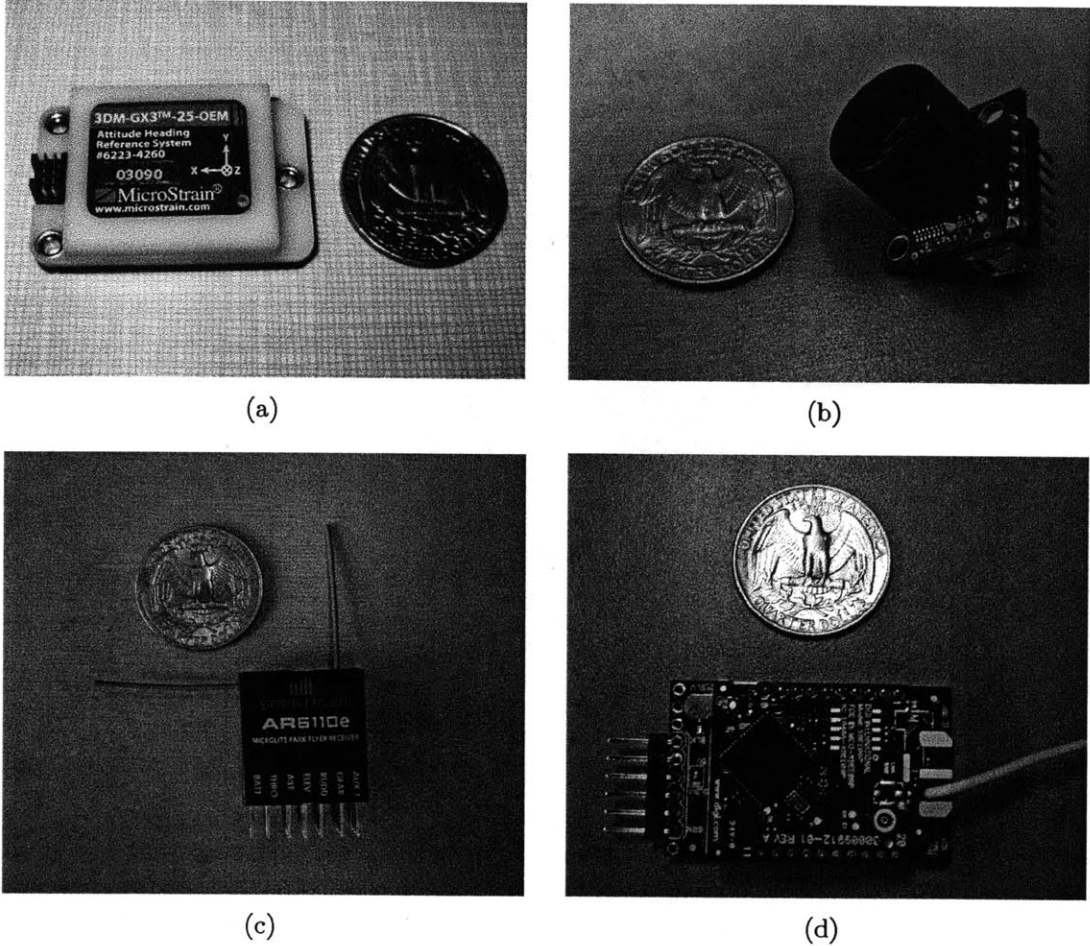


Figure 4-8: Prototype sensors: (a) MicroStrain 3DM-GX3-25OEM IMU, (b) MaxBotix XL-MaxSonar-AE2 ultrasonic rangefinder, (c) Spektrum AR6110E MicroLite 6-Channel DSM2 receiver, (d) XBee-PRO 900 extended range module with XtreamBee board.

rotation matrix, body frame angular rates, and body frame accelerations at 200 Hz over an LVTTL serial connection running at 115,200 bps.

Figure 4-8(b) shows the ultrasonic rangefinder used for altitude sensing. The sensor operates using 42 kHz sound pulses and has a resolution of 1 cm. The range measurement saturates below 20 cm and above 765 cm. Range data is output on a 5 V analog pin and updates at 10 Hz.

The RC receiver and XBee radio are shown in 4-8(c) and 4-8(d) respectively. The XBee is interfaced to a DIY Drones XtreamBee board and configured to provide serial communication at 115,200 bps. Together, the XBee and XtreamBee board weigh 9.7 g.

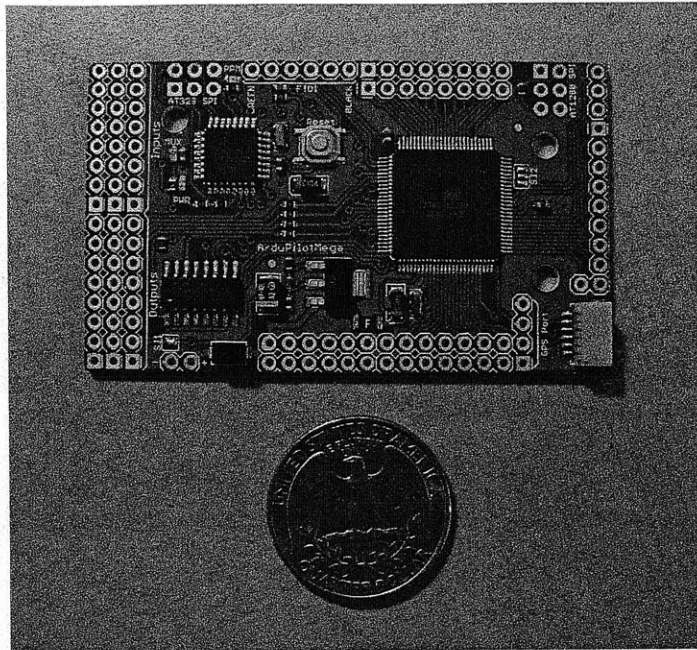


Figure 4-9: Sparkfun ArduPilot Mega board with ATmega1280 and ATmega328.

4.5.3 Controller

The sensor data is read in and processed by an 8-bit, 16 MHz ATmega1280 micro controller on a Sparkfun ArduPilot Mega board shown in Figure 4-9. The controller board includes a separate 16 MHz ATmega328 micro controller that decodes the PWM inputs from the RC receiver and re-encodes PWM signals for the servos and ESCs. The ATmega1280 has 16, 10 bit A/D converters and includes 4 USARTs for serial communication. With connectors, the controller weighs 19.6 g.

The altitude and battery sensors are sampled and low pass filtered at 10 Hz. Altitude range measurements are corrected for the vehicle orientation. A low pass filtered, backward difference on the altitude measurements is used to estimate the vehicle's rate of ascent while hovering.

The control law is recomputed after every complete packet is received from the IMU and parsed (nominally at 200 Hz). A five point moving average filter is used to estimate the vehicle angular accelerations from backward differences on the angular rate data provided by the IMU. Position and attitude integral errors are computed at every control cycle using trapezoidal integration.

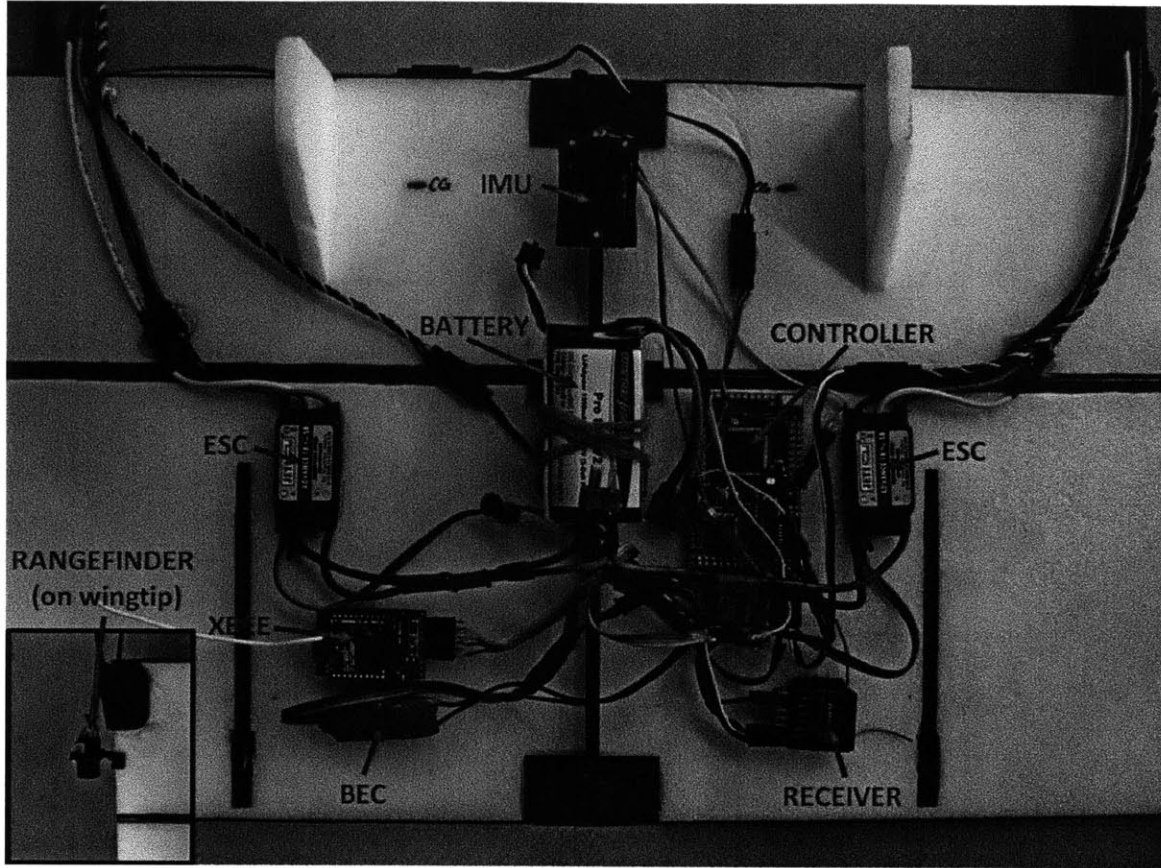


Figure 4-10: Installed avionics and controller setup.

User configurable telemetry data is sent to the ground station via serial communication over the XBee radio at user specified intervals. Actuator outputs are communicated to the ESCs and the servos by a 200Hz PWM signal. The complete avionics and controller setup is shown in Figure 4-10

4.5.4 Wiring

An additional 38g of wiring and connectors were needed to connect the sensors, actuators, and controller.

4.6 Modified Sizing Model

In Figure 4-11, the prototype vehicle masses are compared to the values predicted by the sizing model in Table 3.2. The totals given in Figure 4-11 do not include payload,

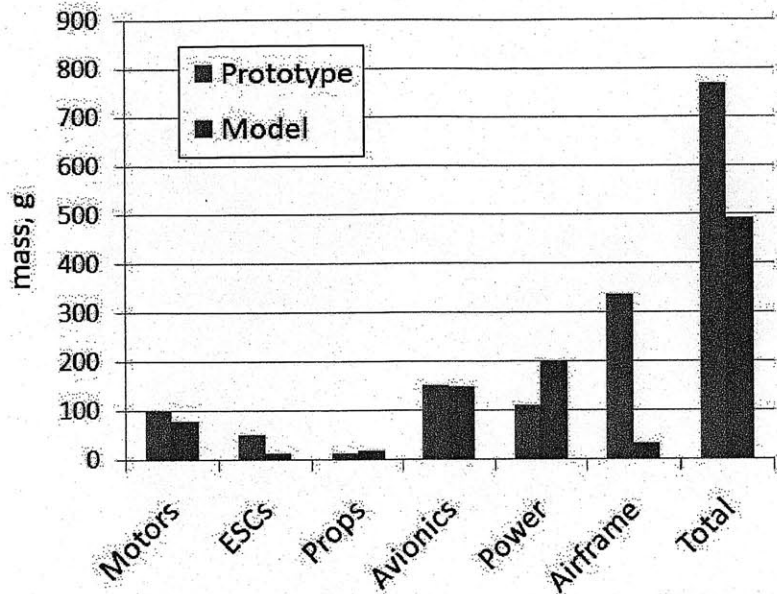


Figure 4-11: Mass comparison between prototype vehicle and sizing model results.

solar cell, or MPPT masses since these components are not included in the prototype.

As expected, the actual motor and ESC mass is slightly greater than predicted in the model due to the over sized motor selection. The avionics prediction, which was a fixed input to the model of 150 g is only 2.7 g less than the actual prototype mass.

The undersized battery used in the prototype results in an over prediction of the power systems mass. Nevertheless, the BEC is unaccounted for in the model and results in a proportionally greater power system mass than would be expected based on the model.

The most significant difference between the model prediction and the actual prototype mass occurs in the airframe mass. The actual prototype airframe mass of 338.3 g is an order of magnitude greater than the 33 g predicted by the model. While the airframe is somewhat overbuilt for testing purposes, the magnitude of the difference suggests a gross underestimate in the sizing model.

In addition to weight reduction from an optimized airframe design, the final vehicle mass can be expected to decrease from that of the prototype mass due to the use of custom built components. The prototype vehicle includes only off the shelf components meant to expedite the development process. Nevertheless, due to limited

selection, these parts cannot be precisely sized and additional mass could be eliminated by consolidating them. Consolidating components would also reduce a large portion of the required wiring mass.

The prototype mass results motivate a modification to the original sizing model presented in Chapter 3. Since actuator mass is dependent on the motor size, a more accurate model would account for actuator mass explicitly as a function of the motor mass. Accordingly, the actuator mass was included separately in the modified model as a having a linear relationship with motor mass as described by Equation 4.5, and the avionics mass was reduced to 50 g to account for only the sensors and controller.

$$m_{act} = k_{act} m_{motor} \quad (4.5)$$

The prototype results suggest that a value of about 0.6 is appropriate for k_{act} in Equation 4.5.

In order to correct the mass prediction, the airframe mass coefficient, k_{struct} was increased from 0.0795 to 0.3. Using these modifications, the sizing model predicts a vehicle sized to the values presented in Table 4.1. The total vehicle mass increases to 952 g and the wingspan increases to 96 cm.

With these modifications to the sizing model, the sizing constraints become infeasible for aspect ratios of 5 or above. The mass build-up, wing geometry, and performance plots for the modified sizing model are shown in Figure 4-12. Based on these results, it can be seen that the minimum sized mass of 0.941 g occurs at an aspect ratio of 3.4. Nevertheless, the mass curve is relatively flat about the minimum mass point and the original aspect ratio choice of 3 adds only 11.2 g to the total vehicle mass while reducing the wingspan by almost 4 cm.

Table 4.1: Modified sizing results for $AR = 3$

Parameter	Units	Value
m_{af}	kg	0.182
m_{cell}	kg	0.118
m_{mppt}	kg	0.018
m_{motor}	kg	0.044
m_{prop}	kg	0.012
m_{esc}	kg	0.007
m_{act}	kg	0.027
m_{bat}	kg	0.256
m	kg	0.952
S	m^2	0.307
b	m	0.960
V_{stall}	m/s^2	7.04
V_{cruise}	m/s^2	7.04
V_{max}	m/s^2	22.64
P_{motor}	W	115.77
E_{bat}	kJ	146.09

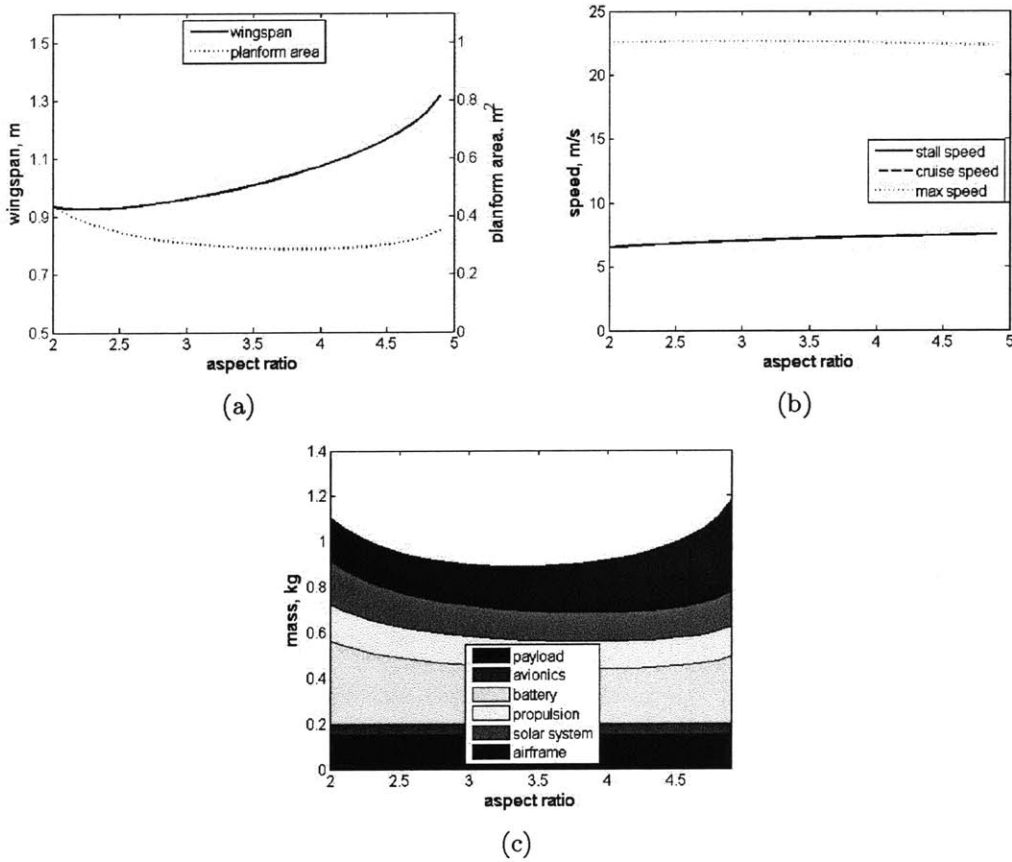


Figure 4-12: Sizing results for the modified sizing model: (a) Wing geometry, (b) vehicle performance, and (c) mass distribution.

Part II

Vehicle Control

THIS PAGE INTENTIONALLY LEFT BLANK

Chapter 5

Control Overview

In order to accomplish the proposed mission, the vehicle must be controlled over a wide range of attitudes as it takes off, climbs vertically, transitions to level flight, re-enters vertical flight, and lands. Operating through such a wide range of attitudes with different lift generation mechanisms results in nonlinear dynamics that are not readily controllable using a single linear controller. Control approaches for such problems typically involve the use of nonlinear controllers such as backstepping and dynamic inversion or a composition of locally valid feedback controllers that “funnel” the system dynamics sequentially between controllers.

Nonlinear backstepping and dynamic inversion controllers are valid over the region where their underlying models accurately describe the system dynamics and have been shown to be capable of controlling prop hanging, fixed wing vehicles during hovering and through transition to and from level flight [43, 44, 49]. Since a single controller is used, these control strategies provide simple transitions between hovering and level flight. Furthermore, Lyapunov based backstepping controllers are particularly well suited for the hovering dynamics where there is a high degree of coupling between attitude and translational dynamics. In [43], a backstepping controller is designed for a small fixed wing RC aircraft. The system model driving the controller design is generated through extensive system identification of pre and post stall aerodynamics. Flight test results verify the ability of the controller to successfully transition the vehicle between hovering and level flight regimes in a space constrained, indoor

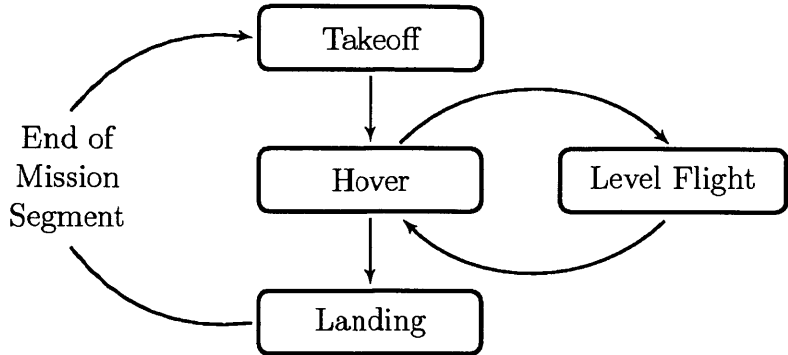


Figure 5-1: Multi-modal control structure, where arrows represent transitions between controller modes.

environment. In order to minimize the demand for detailed system identification and reduce the complexity of the control structure, researchers at BYU have developed a backstepping controller for a tailsitter UAV based on a simplified model with on-line parameter estimation [44]. The backstepping controller was shown to have superior tracking performance when compared to a baseline gain scheduled PID controller. A group at the Georgia Institute of Technology has, similarly, demonstrated transitions to and from hovering flight using an approximate dynamic inversion with neural network parameter estimation [49]. A backstepping approach has also been shown in simulation to successfully control the opposed lateral tilting tiltrotor vehicle described in Section 4.1 during hover [18].

The nonlinear controllers presented above are effective for fixed wing vehicles in flight. However, they are all highly dependent on accurate system models. In some cases, with adaptive techniques such as on-line parameter estimation, the models can be corrected for limited model uncertainty. Nevertheless, the maneuvers proposed for the vehicle presented here involve rapid changes in system dynamics based on whether or not the vehicle is in contact with the ground, hovering, or in level flight. Since each of these phases occur at known times during the mission, the mission phase information can be used to improve the controller performance. This is accomplished through the use of separate controllers for each of the four mission phases described in Table 5.1.

A number of studies have demonstrated the effectiveness of switching between

Table 5.1: Mission phases

Mission Phase	Description
Takeoff	Vehicle in contact with the ground. Rotates from starting attitude to a vertical orientation.
Hover	Vehicle in a verticle orientation with lift generated by rotors. Free from contact with external surfaces and capable of ascent or descent.
Level Flight	Vehicle traveling horizontaly with wing as primary source of lift.
Landing	Vehicle below a specified altitude or in contact with ground. Descends and rotates to lie horizontally on the ground.

multiple controllers that are each capable of performing the desired stabilization task over a subset of the state space. In [50], the author presents a motion planning framework based on a hierarchical system of motion primitives. The results are applied to the control of a small autonomous helicopter through a range of maneuvers. Using convex optimization to compute Sum-of-Squares Lyapunov functions, other research at the Massachusetts Institute of Technology has shown that using sparse trees of LQR stabilized trajectories, quantized control policies can be developed that probabilistically cover the entire controllable subspace [51]. In [29], two linear controllers are used with a transition algorithm to successfully transition a small fixed wing UAV from hover to level flight and back to hover. At Drexel University, a fixed wing UAV demonstrated autonomous transitions from manually controlled level flight to automatically controlled hovering flight using a PD attitude controller [45].

Based on the success of these quantized control approaches, the chosen control structure consists of a separate feedback control algorithm for each phase. Each controller is capable of stabilizing the vehicle dynamics in the current phase as well as taking them into the controllable region of one or more adjacent controllers. Transition algorithms provide conditions for switching between controllers. Figure 5-1 depicts the proposed control structure. Although separate controllers are used for hovering and level flight, they could easily be replaced with a nonlinear controller as

in the referenced examples, thereby reducing the number of distinct controller modes to three.

Chapter 6

Quaternion Attitude Descriptors

6.1 Reference Frames

For the purposes of modeling and control, the equations of motion and angular errors will be defined in the vehicle body axis system shown in Figure 6-1. The x axis of the body frame is defined as pointing out the nose of the aircraft, the y axis is defined as out the right wing, and the z axis points out the bottom of the aircraft as prescribed by the right-hand rule. The earth fixed, inertial frame is defined similarly with the X axis pointing North, the Y axis pointing East, and the Z axis pointing down.

All vehicle orientations will be described relative to the earth fixed frame. Unless explicitly stated or denoted by $(\cdot)_E$, to indicate the earth fixed reference frame, all values are expressed in the body reference frame. Similarly, all body frame axes will be referred to with lower case letters while upper case letters will indicate the Earth fixed axes.

6.2 Motivation

Euler angles are a convenient and commonly used aircraft attitude representation that allow for easy visualization and manipulation. The kinematic equations for the

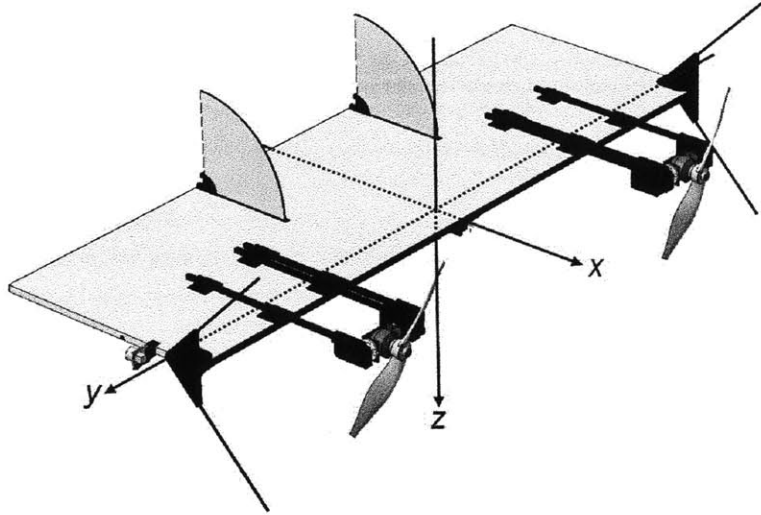


Figure 6-1: Body fixed reference frame.

body rates in terms of the Euler angular rates are [47]

$$\begin{bmatrix} P \\ Q \\ R \end{bmatrix} = \begin{bmatrix} 1 & 0 & -\sin \theta \\ 0 & \cos \phi & \sin \phi \cos \theta \\ 0 & -\sin \phi & \cos \phi \cos \theta \end{bmatrix} \begin{bmatrix} \dot{\phi} \\ \dot{\theta} \\ \dot{\psi} \end{bmatrix} \quad (6.1)$$

The matrix in Equation 6.1 loses rank at $\theta = \pi/2 + k\pi$, where $k \in \mathbb{Z}$. This phenomenon is known as gimbal lock and can result in large magnitude control inputs when the singularity arises [52]. The requirement for the proposed vehicle to operate through a wide range of orientations, including hovering at a pitch angle near vertical, motivates the use of unit quaternions as a singularity free attitude descriptor.

6.3 Quaternion Rotations

6.3.1 Quaternion Operations

A quaternion is a four-vector $q = [q_0, q_1, q_2, q_3]^T$ that can be thought of as consisting of a real scalar component q_0 and a vector component \mathbf{q} in \mathbb{R}^3 such that $q = [q_0, \mathbf{q}^T]^T$. Quaternion multiplication is a non-commutative operation, and defined such that the

quaternion product of the quaternions q and p is

$$q \otimes p = \left[q_0 p_0 - \mathbf{q} \cdot \mathbf{p}, [q_0 \mathbf{p} + p_0 \mathbf{q} + \mathbf{q} \times \mathbf{p}]^T \right]^T \quad (6.2)$$

where the operator \otimes denotes the quaternion product [52].

In some cases, it will be useful to define the quaternion product in the form of a matrix multiplication as shown in Equation 6.3.

$$q \otimes p = [q \otimes] p \quad (6.3)$$

where the matrix $[q \otimes]$ is defined by

$$[q \otimes] = \begin{bmatrix} q_0 & -q_1 & -q_2 & -q_3 \\ q_1 & q_0 & -q_3 & q_2 \\ q_2 & q_3 & q_0 & -q_1 \\ q_3 & -q_2 & q_1 & q_0 \end{bmatrix} \quad (6.4)$$

It is simple to verify that Equation 6.3 is an equivalent expression for Equation 6.2.

The quaternion conjugate is defined by

$$q^* = [q_0, -\mathbf{q}^T]^T = [q_0, -q_1, -q_2, -q_3]^T \quad (6.5)$$

such that $q \otimes q^* = q^* \otimes q = [q_0^2, \mathbf{0}]^T$ and $[q^* \otimes] = [q \otimes]^T = [q \otimes]^{-1}$.

In many cases, it is useful to manipulate vectors in \Re^3 by quaternion multiplication. In such cases, the vector may be converted to a pure quaternion by appending it with a scalar component of zero such that, for a vector $\mathbf{v} \in \Re^3$, the pure quaternion representation is given by $v = [0, \mathbf{v}^T]^T$. It can be seen from Equation 6.2, that

$$q \otimes v \otimes q^* = q \otimes [0, \mathbf{v}^T]^T \otimes q^* = w = [0, \mathbf{w}^T]^T \quad (6.6)$$

where $\mathbf{w} \in \Re^3$.

Thus, bracketing a pure quaternion with a quaternion and its conjugate results in

another pure quaternion. Furthermore, if the quaternion bracketing the pure quaternion is defined as a unit quaternion such that $q = [\cos \frac{\gamma}{2}, \mathbf{u}^T \sin \frac{\gamma}{2}]^T$, then \mathbf{w} is the vector that results from a rotation of \mathbf{v} through an angle of γ , about the axis \mathbf{u} [53]. Similarly, $q^* \otimes v \otimes q$ will result in a rotation of the vector \mathbf{v} through an angle of $-\gamma$, about the axis \mathbf{u} , and can be seen as a frame rotation by an angle of γ , about the axis \mathbf{u} .

Sequential rotations by quaternions q_1 and q_2 in a fixed frame can be written as,

$$\begin{aligned} q_2 \otimes (q_1 \otimes v \otimes q_1^*) \otimes q_2^* &= (q_2 \otimes q_1) \otimes v \otimes (q_2 \otimes q_1)^* \\ &= q_{total} \otimes v \otimes q_{total}^* \end{aligned} \quad (6.7)$$

where

$$q_{total} = q_2 \otimes q_1 \quad (6.8)$$

In the case of two successive frame rotations defined by the quaternions q_1 and q_2 ,

$$\begin{aligned} q_2^* \otimes (q_1^* \otimes v \otimes q_1) \otimes q_2 &= (q_1 \otimes q_2)^* \otimes v \otimes (q_1 \otimes q_2) \\ &= q_{total}^* \otimes v \otimes q_{total} \end{aligned} \quad (6.9)$$

where

$$q_{total} = q_1 \otimes q_2 \quad (6.10)$$

Thus, in the frame rotation case the order of the quaternions is reversed in the composite quaternion [53].

6.3.2 Kinematics

The quaternion rates can be expressed in terms of the current orientation and the body rates as [54]

$$\dot{q} = \frac{1}{2}q \otimes \begin{bmatrix} 0 \\ \boldsymbol{\omega} \end{bmatrix}$$

$$= \frac{1}{2} \begin{bmatrix} -q_1 & -q_2 & -q_3 \\ q_0 & -q_3 & q_2 \\ q_3 & q_0 & -q_1 \\ -q_2 & q_1 & q_0 \end{bmatrix} \begin{bmatrix} P \\ Q \\ R \end{bmatrix} \quad (6.11)$$

6.4 Quaternion Error

The desired vehicle position may be expressed as a successive frame rotation from the earth fixed frame by

$$q_d = q_m \otimes q_e^* \quad (6.12)$$

where q_d is the desired attitude with respect to the earth fixed frame, q_m is the measured attitude from the earth frame, and q_e is an error quaternion defined in the body frame as the rotation from the desired orientation to the measured orientation. Solving Equation 6.12 for the error quaternion gives

$$q_e = q_d^* \otimes q_m \quad (6.13)$$

The total angular error may be calculated from the error quaternion as

$$\gamma_e = 2 \arccos q_{e0} \quad (6.14)$$

As in [55], the vector component of the error quaternion can then be used to project this error onto each of the body axes to form the angular error $\mathbf{e} = [e_x, e_y, e_z]^T$, where

$$\begin{aligned} e_x &= \gamma_e \frac{q_{e1}}{\sin \frac{\gamma_e}{2}} \\ e_y &= \gamma_e \frac{q_{e2}}{\sin \frac{\gamma_e}{2}} \\ e_z &= \gamma_e \frac{q_{e3}}{\sin \frac{\gamma_e}{2}} \end{aligned} \quad (6.15)$$

6.5 Quaternion Linearization

In many cases, it will be useful to linearize the system model. Since a quaternion attitude description is used, this means that the equations must be linearized with respect to the elements of the quaternion. For a vector valued function $\mathbf{G}(\mathbf{q})$, the Jacobian of the function with respect to the quaternion elements is given by

$$\nabla_{\mathbf{q}} \mathbf{G} \approx \begin{bmatrix} \frac{\partial G_1}{\partial q_0} & \frac{\partial G_1}{\partial q_1} & \frac{\partial G_1}{\partial q_2} & \frac{\partial G_1}{\partial q_3} \\ \vdots & \vdots & \vdots & \vdots \\ \frac{\partial G_n}{\partial q_0} & \frac{\partial G_n}{\partial q_1} & \frac{\partial G_n}{\partial q_2} & \frac{\partial G_n}{\partial q_3} \end{bmatrix} \quad (6.16)$$

The linearization is then

$$\mathbf{G} = \mathbf{G}_O + (\nabla_{\mathbf{q}} \mathbf{G})_O \Delta \mathbf{q} \quad (6.17)$$

where the subscript O indicates evaluation at the specified operating point and $\Delta \mathbf{q} = \mathbf{q} - \mathbf{q}_O$.

Since $\Delta \mathbf{q}$ is dependent on the operating point chosen, it is often more convenient to express the linearization in terms of the error quaternion defined in Equation 6.13. The error quaternion can be thought of as a linear map from the measured quaternion parameterized by the desired quaternion. As a result, the Jacobian in Equation 6.16 can be transformed to the error quaternion coordinates by

$$\nabla_{q_e} \mathbf{G} = \nabla_{\mathbf{q}} \mathbf{G} [q_O \otimes] \quad (6.18)$$

The linearization can then be written in terms of the error quaternion as

$$\mathbf{G} = \mathbf{G}_O + (\nabla_{\mathbf{q}} \mathbf{G})_O [q_O \otimes] \Delta q_e \quad (6.19)$$

When the operating point for linearization coincides with the desired quaternion, then

$$\Delta q_e = [q_{e_0} - 1, q_{e_1}, q_{e_2}, q_{e_3}]^T \quad (6.20)$$

Writing the error quaternion in axis angle form

$$\Delta q_e = \left[\cos \frac{\gamma_e}{2} - 1, \mathbf{u}^T \sin \frac{\gamma_e}{2} \right]^T \quad (6.21)$$

Linearizing this result about zero angular error gives the change in the error quaternion in terms of the angular errors derived in Equation 6.15.

$$\Delta q_e = \frac{\gamma_e}{2} [0, \mathbf{u}^T]^T = \frac{1}{2} [0, \mathbf{e}^T]^T \quad (6.22)$$

The linearization of the vector valued function can then be written in terms of the angular errors as

$$\mathbf{G} = \mathbf{G}_O + \frac{1}{2} (\nabla_q \mathbf{G})_O [q_O \otimes] [0, \mathbf{e}^T]^T \quad (6.23)$$

Noting that $[0, \dot{\mathbf{e}}^T]^T = [0, \boldsymbol{\omega}^T]^T$, the linearized quaternion error rate can be computed from Equation 6.22 as (This result could have also been reached by directly linearizing Equation 6.11)

$$\dot{q}_e = \frac{1}{2} [0, \boldsymbol{\omega}^T]^T \quad (6.24)$$

The linearized quaternion rate can now be found by

$$\dot{q} = \frac{1}{2} q_O \otimes [0, \boldsymbol{\omega}^T]^T \quad (6.25)$$

THIS PAGE INTENTIONALLY LEFT BLANK

Chapter 7

Modeling and Simulation

7.1 Rotational Dynamics

7.1.1 Equations of Motion

The rotational dynamics of the vehicle are governed by

$$J\dot{\boldsymbol{\omega}} = \mathbf{L} \times \boldsymbol{\omega} + \boldsymbol{\tau} \quad (7.1)$$

where J is the vehicle's inertia tensor, $\boldsymbol{\omega} = [P, Q, R]^T$ is the vehicle angular velocity, \mathbf{L} is the vehicle's angular momentum, and $\boldsymbol{\tau} = [\tau_x, \tau_y, \tau_z]^T$ is the vector of applied torques.

Since the inertia tensor is always symmetric, positive definite, it is a full rank matrix and can be inverted [56]. As a result, Equation 7.1 can be solved for the angular acceleration.

$$\dot{\boldsymbol{\omega}} = J^{-1}(\mathbf{L} \times \boldsymbol{\omega} + \boldsymbol{\tau}) \quad (7.2)$$

The angular momentum \mathbf{L} is composed of the angular momentum from rotation about the vehicle's center of gravity (or pivot location in the case of a takeoff) as well as the angular momentum of the spinning motors and rotors. Since the rotors are counter rotating, typically close to being aligned, and will normally be rotating at similar rates, their momenta will largely cancel out. Thus, the angular momentum of the

rotors will be neglected, giving

$$\mathbf{L} = J\boldsymbol{\omega} \quad (7.3)$$

In cases such as takeoff where the vehicle is pivoting about a point other than the center of gravity, the moment of inertia can be parametrized in terms of the pivot location such that

$$J = J_{C.G.} + m [(\mathbf{r}_p^T \mathbf{r}_p) I_3 - \mathbf{r}_p \mathbf{r}_p^T] \quad (7.4)$$

where $J_{C.G.}$ is the inertia tensor about the center of gravity, $\mathbf{r}_p = [r_{px}, r_{py}, r_{pz}]^T$ is the position of the pivot point relative to the center of gravity, m is the vehicle mass, and I_3 is the 3×3 identity matrix. For the purposes of this model, $J_{C.G.}$ will be assumed to be constant. Articulation of the rotors relative to the aircraft body will cause slight variations in the actual values of the elements of the inertia tensor. However, detailed CAD models show that this variation will not exceed more than 2% for any of the principal moments of inertia. Rotor articulation will have significant effects on the off-diagonal products of inertia J_{xz} , J_{xy} , and J_{yz} , however, these terms are all at least two orders of magnitude smaller than the principal moments of inertia and will be neglected.

7.1.2 Applied Torques

The applied torques in Equation 7.1 are caused by gravity, rotor thrust and drag, and aerodynamic forces. The torque from gravitational acceleration arises when the vehicle is rotating about a point other than the center of gravity and can be expressed in terms of the pivot location \mathbf{r}_p , and vehicle orientation q as

$$\boldsymbol{\tau}_g = mg \left[-\mathbf{r}_p \times \left(q^* \otimes [0, 0, 0, 1]^T \otimes q \right) \right] \quad (7.5)$$

where g is gravitational acceleration. Writing each component separately in terms of the individual quaternion components gives

$$\tau_{gx} = -mg [r_{py} (q_0^2 - q_1^2 - q_2^2 + q_3^2) - r_{pz} (2q_0q_1 + 2q_2q_3)] \quad (7.6)$$

$$\tau_{g_y} = mg [r_{p_x} (q_0^2 - q_1^2 - q_2^2 + q_3^2) + r_{p_z} (2q_0q_2 - 2q_1q_3)] \quad (7.7)$$

$$\tau_{g_z} = -mg [r_{p_x} (2q_0q_1 + 2q_2q_3) + r_{p_y} (2q_0q_2 - 2q_1q_3)] \quad (7.8)$$

During hover the pivot location is at the center of gravity $\mathbf{r}_p = \mathbf{0}$, and the gravitational torque will be zero.

The torque from the rotor thrust can be expressed as

$$\boldsymbol{\tau}_r = T_R (\mathbf{r}_r^R - \mathbf{r}_p) \times [\cos \alpha_R, 0, -\sin \alpha_R]^T + T_L (\mathbf{r}_r^L - \mathbf{r}_p) \times [\cos \alpha_L, 0, -\sin \alpha_L]^T \quad (7.9)$$

where \mathbf{r}_r^R and \mathbf{r}_r^L are the positions, relative to the center of gravity, of the right and left rotor articulation points, T_R and T_L are the thrusts of the right and left rotors, and α_R and α_L are the articulation angles of the right and left rotors about the y axis where zero articulation is defined as when the rotor spin axis is parallel with the vehicle x axis.

Since the rotor articulation points are located at the same x and z locations, their positions with respect to the center of gravity can be written as

$$\mathbf{r}_r^R = \begin{bmatrix} r_{r_x} \\ r_{r_y}^R \\ r_{r_z} \end{bmatrix}, \text{ and } \mathbf{r}_r^L = \begin{bmatrix} r_{r_x} \\ r_{r_y}^L \\ r_{r_z} \end{bmatrix} \quad (7.10)$$

Defining the locations of the rotor articulation points relative to the pivot location gives

$$\Delta \mathbf{r}_r^R = \mathbf{r}_r^R - \mathbf{r}_p = \begin{bmatrix} \Delta r_{r_x} \\ \Delta r_{r_y}^R \\ \Delta r_{r_z} \end{bmatrix}, \text{ and } \Delta \mathbf{r}_r^L = \mathbf{r}_r^L - \mathbf{r}_p = \begin{bmatrix} \Delta r_{r_x} \\ \Delta r_{r_y}^L \\ \Delta r_{r_z} \end{bmatrix} \quad (7.11)$$

Using this notation, Equation 7.9 can be expanded as

$$\tau_{r_x} = -\Delta r_{r_y}^L T_L \sin \alpha_L - \Delta r_{r_y}^R T_R \sin \alpha_R \quad (7.12)$$

$$\tau_{r_y} = \Delta r_{r_z} (T_L \cos \alpha_L + T_R \cos \alpha_R) + \Delta r_{r_x} (T_L \sin \alpha_L + T_R \sin \alpha_R) \quad (7.13)$$

$$\tau_{rz} = -\Delta r_{ry}^L T_L \cos \alpha_L - \Delta r_{ry}^R T_R \cos \alpha_R \quad (7.14)$$

Again, since the rotors are counter rotating, will usually be close to aligned, and will most often have similar rates of rotation, the rotor drag torques will be neglected.

Aerodynamic forces come from damping on the motion of the wing and tail as they move through the air as well as from the interaction of the rotor slipstream with the wing surface. The propulsive induced forces on the wing involve complex interactions and are not well understood or easily modeled through an analytic expression derived from the laws of physics. Nevertheless, empirical results in [46], where the rotor of an MAV was angled at ± 5 degrees from alignment with the longitudinal axis, suggest that the change in magnitude of the aerodynamic forces due to propeller slipstream interactions will be small compared to that of the thrust required for hover. System identification could be used to characterize these effects in detail, however, for the present model they are neglected.

During takeoff and hover, the predominant longitudinal flow over the wing surface will be due to the rotor slipstreams. As a result, on areas of the wing where the slipstreams have little effect, airflow caused by rotational motion of the wing will result in stalled flow. In these areas, a damping force can be computed from the dynamic pressure of the air as it encounters the wing surface. In areas where the propulsive induced flow is sufficiently high, however, the wing will generate lift due to the induced angle of attack. Again, developing an analytic model for these effects while allowing for arbitrary rotor orientation would result in a much more complex model. Furthermore, at low rotational rates, these forces are likely to be negligible compared to the rotor torques and will be neglected. Since the damping forces help to stabilize the system, failure to include aerodynamic damping in the model will result in a more conservative assessment of the vehicle's stability characteristics.

7.2 Translational Dynamics

7.2.1 Equations of Motion

The translational dynamics in hover can be expressed in the earth frame as

$$\ddot{\mathbf{R}} = \frac{1}{m} (\mathbf{F})_E \quad (7.15)$$

where $\mathbf{F} = [F_x, F_y, F_z]^T$ is the total applied force and $\mathbf{R} = [X, Y, Z]^T$ is the vehicle position in the earth fixed reference frame.

7.2.2 Applied Forces

Again, neglecting aerodynamic forces, the applied forces in hover come from gravity and the rotor forces. The vehicle weight is easily expressed in the earth frame as

$$(\mathbf{F}_g)_E = \begin{bmatrix} 0 \\ 0 \\ mg \end{bmatrix} \quad (7.16)$$

The body rotor forces can be calculated as in Equation 7.9 by

$$\mathbf{F}_r = \begin{bmatrix} F_{r_x} \\ F_{r_y} \\ F_{r_z} \end{bmatrix} = T_R \begin{bmatrix} \cos \alpha_R \\ 0 \\ -\sin \alpha_R \end{bmatrix} + T_L \begin{bmatrix} \cos \alpha_L \\ 0 \\ -\sin \alpha_L \end{bmatrix} \quad (7.17)$$

Quaternion multiplication can then be used to express the rotor forces in the earth frame as

$$\left[0, (\mathbf{F}_r)_E^T \right]^T = q \otimes [0, \mathbf{F}_r^T]^T \otimes q^* \quad (7.18)$$

Expanding Equation 7.18 and adding the weight force in Equation 7.16 allows the earth frame accelerations to be written as

$$m\ddot{X} = (q_0^2 + q_1^2 - q_2^2 - q_3^2) F_{r_x} + 2(q_0 q_2 + q_1 q_3) F_{r_z}$$

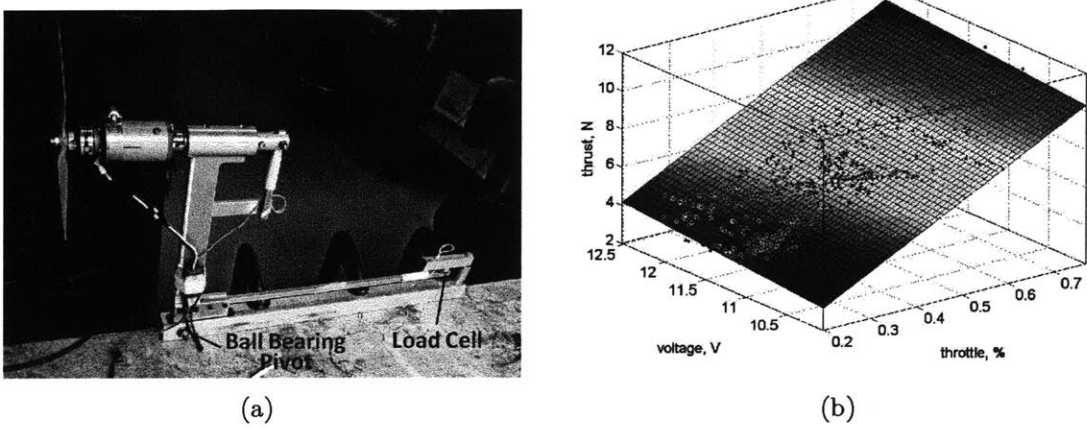


Figure 7-1: Motor test setup (a) and thrust data surface fit (b).

$$\begin{aligned} m\ddot{Y} &= 2(q_0q_3 + q_1q_2) F_{r_x} + 2(q_2q_3 - q_0q_1) F_{r_z} \\ m\ddot{Z} &= 2(q_1q_3 - q_0q_2) F_{r_x} + (q_0^2 - q_1^2 - q_2^2 + q_3^2) F_{r_z} + mg \end{aligned} \quad (7.19)$$

7.3 Thrust Model

Figure 7-1(a) shows the test setup used for the motor characterization. A calibrated load cell and voltage divider were used to take thrust and voltage measurements. The throttle was varied manually by PWM input from an RC transmitter receiver pair. After each throttle update, a wait time of 100 ms was imposed to allow the motor and rotor to stabilize to the commanded speed. For each throttle setting, 10,000 thrust and battery measurements were taken and their average values were recorded.

For a true speed controlled motor, thrust is expected to be a function of the throttle input squared. Nevertheless, a second order surface fit of the thrust data showed less than a 2% improvement in the fit quality over a first order fit as defined by the R-squared value. As a result, a first order surface was selected for the model in order to keep the model thrust input linear with the commanded throttle. The linear least squares surface fit shown in Figure 7-1(b) is defined as

$$T = C_0 + C_V V + C_\delta \delta \quad (7.20)$$

where δ is the percentage of the maximum throttle applied, V is the battery voltage in volts, and C_0 , C_V , and C_δ are constants defined by the surface fit to be -3.36 N, 0.41 N/V, and 12.46 N respectively.

7.4 Model Summary

As a review, the equations of motion, control torques, and thrust model for the vehicle rotational dynamics are presented below

$$J\dot{\boldsymbol{\omega}} = \mathbf{L} \times \boldsymbol{\omega} + \boldsymbol{\tau}$$

$$\boldsymbol{\tau} = \boldsymbol{\tau}_g + \boldsymbol{\tau}_r$$

$$\tau_{gx} = -mg [r_{py} (q_0^2 - q_1^2 - q_2^2 + q_3^2) - r_{pz} (2q_0q_1 + 2q_2q_3)]$$

$$\tau_{gy} = mg [r_{px} (q_0^2 - q_1^2 - q_2^2 + q_3^2) + r_{pz} (2q_0q_2 - 2q_1q_3)]$$

$$\tau_{gz} = -mg [r_{px} (2q_0q_1 + 2q_2q_3) + r_{py} (2q_0q_2 - 2q_1q_3)]$$

$$\tau_{rx} = -\Delta r_{ry}^L T_L \sin \alpha_L - \Delta r_{ry}^R T_R \sin \alpha_R$$

$$\tau_{ry} = \Delta r_{rz} (T_L \cos \alpha_L + T_R \cos \alpha_R) + \Delta r_{rx} (T_L \sin \alpha_L + T_R \sin \alpha_R)$$

$$\tau_{rz} = -\Delta r_{ry}^L T_L \cos \alpha_L - \Delta r_{ry}^R T_R \cos \alpha_R$$

$$\ddot{\mathbf{R}} = \frac{1}{m} (\mathbf{F})_E$$

$$\mathbf{F} = \mathbf{F}_g + \mathbf{F}_r$$

$$(\mathbf{F}_g)_E = \begin{bmatrix} 0 \\ 0 \\ mg \end{bmatrix}$$

$$\mathbf{F}_r = \begin{bmatrix} F_{rx} \\ F_{ry} \\ F_{rz} \end{bmatrix} = T_R \begin{bmatrix} \cos \alpha_R \\ 0 \\ -\sin \alpha_R \end{bmatrix} + T_L \begin{bmatrix} \cos \alpha_L \\ 0 \\ -\sin \alpha_L \end{bmatrix}$$

$$m\ddot{X} = (q_0^2 + q_1^2 - q_2^2 - q_3^2) F_{rx} + 2(q_0q_2 + q_1q_3) F_{rz}$$

$$m\ddot{Y} = 2(q_0q_3 + q_1q_2) F_{rx} + 2(q_2q_3 - q_0q_1) F_{rz}$$

$$m\ddot{Z} = 2(q_1q_3 - q_0q_2) F_{ry} + (q_0^2 - q_1^2 - q_2^2 + q_3^2) F_{rz} + mg$$

$$T = C_0 + C_V V + C_\delta \delta$$

7.5 Simulation

7.5.1 Overview

A nonlinear simulation based on Equations 7.1, 6.11, and 7.15 was implemented using MATLAB's ode23 solver. By specifying the control algorithm and pivot location, the simulation can predict the vehicle dynamics in both the takeoff and hovering mission phases.

In addition to the angular rates, quaternion orientation, and earth frame translational rates and positions, the simulated state vector includes delayed actuator responses which are modeled as first order poles. For the servos, the delay time constant is set at 70 ms. For the motors, the delay time constant is 250 ms. Additional pure delays are included in the command signals and the sensor measurements for closed loop simulations. The attitude sensing frequency is simulated at 140 Hz and the command signals are delayed at 50 Hz. The moments of inertia and physical parameters used in the simulation were estimated from detailed CAD models and direct measurements of the prototype vehicle.

7.5.2 Validation

The simulation was validated in the pitch axis based on several open loop pitch up maneuvers where the vehicle was placed on the ground, the rotors were commanded to point vertically at all times to prevent translational motion, and the thrust was set at a fixed value. Different length standoffs were secured to the trailing edge of the vehicle, as shown in Figure 7-2, to simulate off nominal pivot location.

Figure 7-3 shows the pitch responses of the simulation compared to five experimental results for pivots at the wing trailing edge, 150 mm behind the trailing edge, and 300 mm behind the trailing edge.

Similar validation tests were performed with closed loop feedback on the pitch

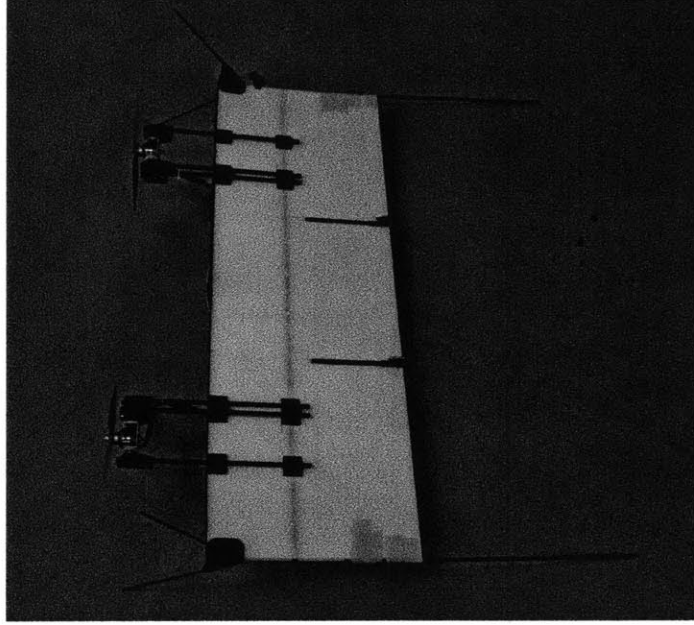


Figure 7-2: Prototype with standoff on trailing edge to simulate off nominal pivot locations

error. The tests shown in Figure 7-4 incorporated proportional derivative feedback on the pitch error into the throttle input.

The simulated responses in Figures 7-3 and 7-4 show some deviation from the experimental results, particularly in the 150 mm offset case. Nevertheless, the large scale behavior is still the same. Since the vehicle must switch between takeoff and hover controller modes when it gets near a vertical orientation, it is important that the simulation phase matches the experimental data at pitch angles near vertical. Figures 7-3 and 7-4 indicate that the model is capable of estimating the terminal phase condition.

The delays included in the simulation have a significant affect on the ability of the PD throttle control to stabilize the vehicle trajectory about the desired phase. Figure 7-5 shows the response for the same simulations as presented in Figure 7-4, but without any delays. These simulations indicate that the delays are a significant contributor to the destabilizing effect present in the experimental data and the takeoff control problem could potentially be simplified through improved actuator selection.

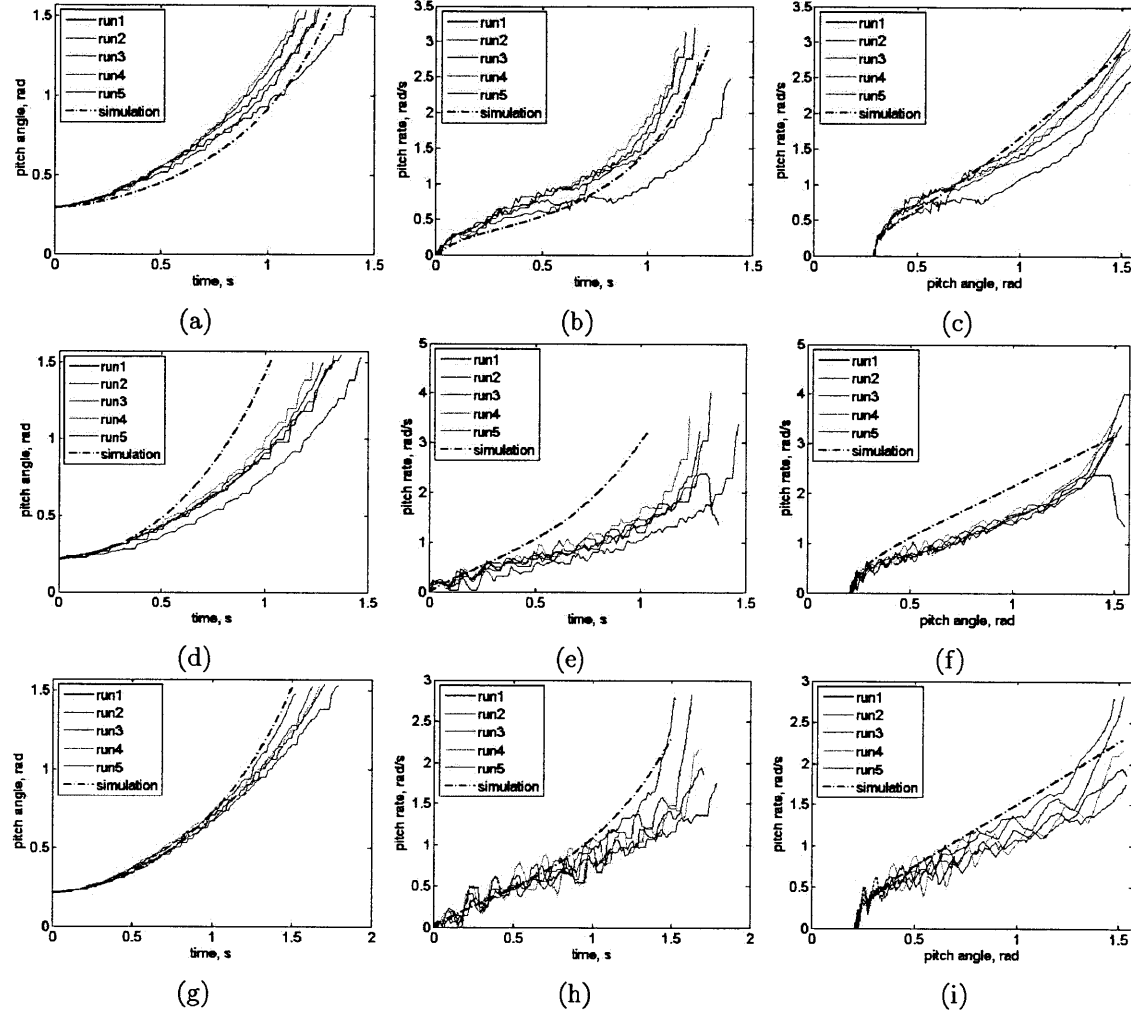


Figure 7-3: Simulated pitch response compared to experimental results for an open loop pitch up manuever with the pivot location at the trailing edge (a-c), 150 mm behind the trailing edge (d-f), and 300 mm behind the trailing edge (g-i).

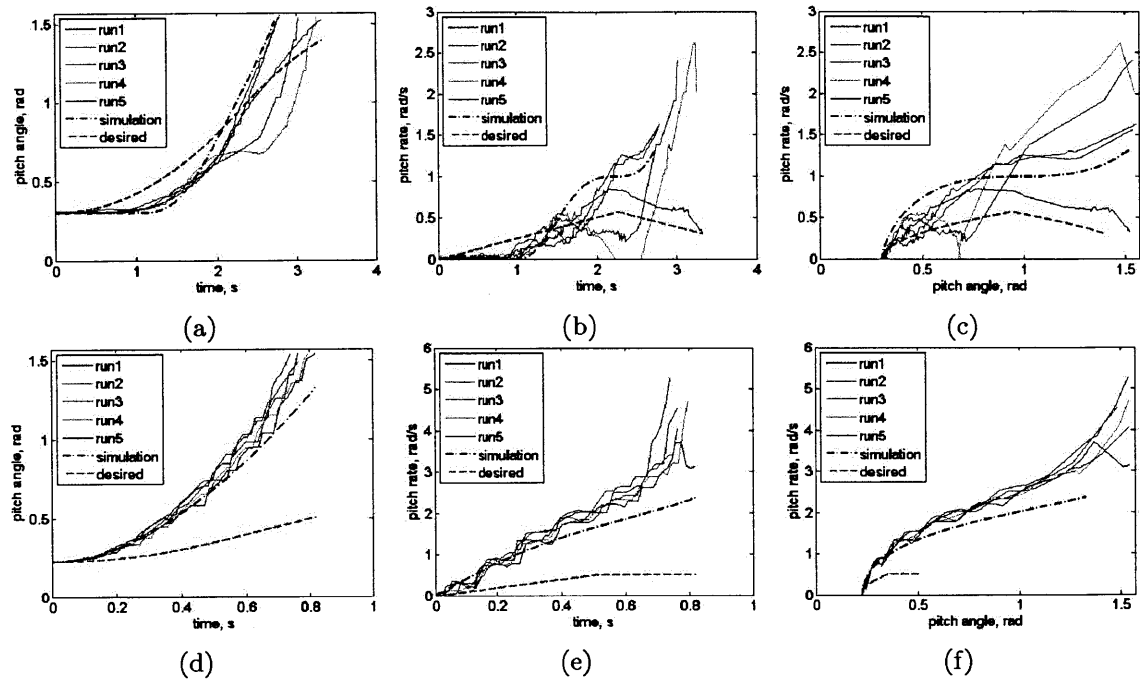


Figure 7-4: Simulated pitch response compared to experimental results for a closed loop pitch up manuever with the pivot location at the trailing edge (a-c) and 150 mm behind the trailing edge (d-f).

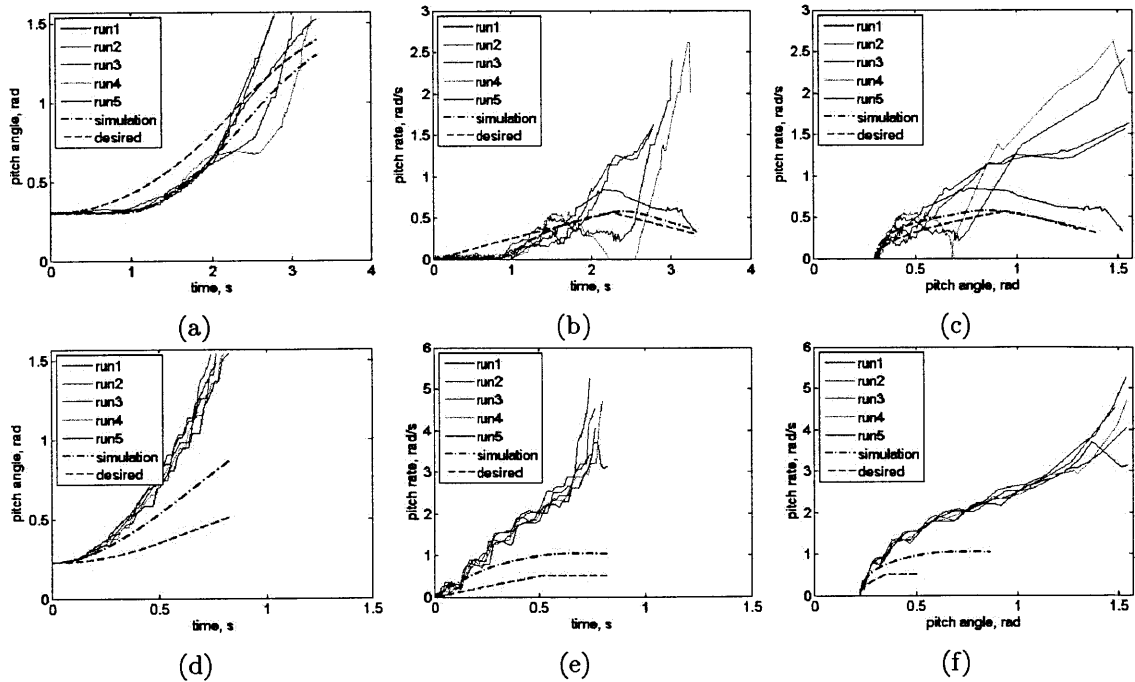


Figure 7-5: Simulated pitch response with no delay compared to experimental results for a closed loop pitch up maneuver with the pivot location at the trailing edge (a-c) and 150 mm behind the trailing edge (d-f).

THIS PAGE INTENTIONALLY LEFT BLANK

Chapter 8

Hovering Control

8.1 Overview

Based on successful implementations of nested linear controllers in fixed wing hovering flight [29, 45], a linear PD attitude controller is used to stabilize the vehicle about the nominal hovering attitude. PID control is used to maintain the vehicle altitude, and an outer PID position feedback loop is proposed for translational vehicle control.

8.2 Linearized Hovering Model

During hovering flight, the pivot location is at the center of gravity. As a result $\mathbf{r}_p = \mathbf{0}$ so the torques due to gravity are zero and the approximate inertia tensor reduces to a diagonal matrix. The vehicle rotational dynamics can then be expressed as

$$\dot{P} = \frac{1}{J_{xx}} \left[-T_L \sin \alpha_L r_{r_y}^L - T_R \sin \alpha_R r_{r_y}^R + QR (J_{yy} - J_{zz}) \right] \quad (8.1)$$

$$\begin{aligned} \dot{Q} &= \frac{1}{J_{yy}} [r_{r_z} (T_L \cos \alpha_L + T_R \cos \alpha_R) \\ &\quad + r_{r_x} (T_L \sin \alpha_L + T_R \sin \alpha_R) + PR (J_{zz} - J_{xx})] \end{aligned} \quad (8.2)$$

$$\dot{R} = \frac{1}{J_{zz}} \left[-T_L r_{r_y}^L \cos \alpha_L - T_R r_{r_y}^R \cos \alpha_R + PQ (J_{xx} - J_{yy}) \right] \quad (8.3)$$

Linearizing these equations about zero angular rate gives

$$\dot{\boldsymbol{\omega}} = B_{\boldsymbol{\omega}} \mathbf{u}_0 \quad (8.4)$$

where $B_{\boldsymbol{\omega}}$ is the input matrix defined by Equations B.1-B.13 in Appendix B, and

$$\mathbf{u}_0 = [\alpha_R, \alpha_L, T_R, T_L]^T \quad (8.5)$$

Similarly, linearizing the translational dynamics in Equation 7.19 gives

$$\ddot{\mathbf{R}} = A_R \mathbf{e} + B_R \mathbf{u}_0 \quad (8.6)$$

where A_R and B_R are the matrices defined by Equations B.14-B.36 in Appendix B.

If it is assumed that $r_y^R = -r_y^L = r_y$ and $r_z = 0$, then for a vertical orientation equilibrium is achieved when $\alpha_R = \alpha_L = 0$ and $T_R = T_L = \frac{W}{2}$. Evaluating the matrix $B_{\boldsymbol{\omega}}$ at this operating point gives

$$B_{\boldsymbol{\omega}} = \begin{bmatrix} -\frac{Wr_y}{2J_{xx}} & \frac{Wr_y}{2J_{xx}} & 0 & 0 \\ \frac{Wr_x}{2J_{yy}} & \frac{Wr_x}{2J_{yy}} & 0 & 0 \\ 0 & 0 & -\frac{r_y}{J_{zz}} & \frac{r_y}{J_{zz}} \end{bmatrix} \quad (8.7)$$

The coupling in Equation 8.7 can be eliminated by a simple linear mapping of the control inputs. Rather than the individual thrusts and articulation angles of each motor, let the control inputs be defined based on a collective throttle input δ_{coll} , a differential throttle input δ_{diff} , a collective articulation angle α_{coll} , and a differential articulation angle, α_{diff} such that,

$$\mathbf{u}_0 = Y \mathbf{u} \quad (8.8)$$

where the control input \mathbf{u} is defined by

$$\mathbf{u} = [\alpha_{diff}, \alpha_{coll}, \delta_{diff}, \delta_{coll}]^T \quad (8.9)$$

and Y is the control mapping given by

$$Y = \begin{bmatrix} -1 & 1 & 0 & 0 \\ 1 & 1 & 0 & 0 \\ 0 & 0 & -C_\delta & C_\delta \\ 0 & 0 & C_\delta & C_\delta \end{bmatrix} \quad (8.10)$$

With this input mapping, the linearized angular accelerations become

$$\dot{\boldsymbol{\omega}} = B_{\boldsymbol{\omega}} Y \mathbf{u} = \begin{bmatrix} \frac{W r_{ry}}{J_{xx}} & 0 & 0 & 0 \\ 0 & \frac{W r_{rx}}{J_{yy}} & 0 & 0 \\ 0 & 0 & \frac{2 r_{rz}}{J_{zz}} & 0 \end{bmatrix} \mathbf{u} \quad (8.11)$$

Since the last column in the matrix $B_{\boldsymbol{\omega}} Y$ is zero, the collective throttle input does not affect the rotational dynamics of the linearized model. For simplicity, let $[B_{\boldsymbol{\omega}} Y]_{\boldsymbol{\omega}}$ denote the first three columns of $B_{\boldsymbol{\omega}} Y$, and $\mathbf{u}_{\boldsymbol{\omega}} = [\alpha_{diff}, \alpha_{coll}, \delta_{diff}]^T$. Using the axis errors defined in Equation 6.15, the linearized attitude dynamics can be described by

$$\begin{bmatrix} \dot{\mathbf{e}} \\ \dot{\boldsymbol{\omega}} \end{bmatrix} = \begin{bmatrix} 0 & I_3 \\ 0 & 0 \end{bmatrix} \begin{bmatrix} \mathbf{e} \\ \boldsymbol{\omega} \end{bmatrix} + \begin{bmatrix} 0 \\ [B_{\boldsymbol{\omega}} Y]_{\boldsymbol{\omega}} \end{bmatrix} \mathbf{u}_{\boldsymbol{\omega}} \quad (8.12)$$

where I_3 is the 3×3 identity matrix.

Similarly, evaluating A_R and B_R at the specified operating condition gives

$$\ddot{\mathbf{R}} = \begin{bmatrix} 0 & -\frac{W}{m} & 0 \\ 0 & 0 & \frac{W}{m} \\ 0 & 0 & 0 \end{bmatrix} \mathbf{e} + \begin{bmatrix} 0 & -\frac{W}{m} & 0 & 0 \\ 0 & 0 & 0 & 0 \\ 0 & 0 & 0 & -\frac{2C_\delta}{m} \end{bmatrix} \mathbf{u} \quad (8.13)$$

8.3 Attitude Control

The diagonal structure of the blocks in Equation 8.12 leads to 3 decoupled pairs of attitude equations, one about each axis. This structure motivates direct feedback from the individual axis errors to the control inputs such that errors about the x -axis

are fed back into the differential articulation command, errors about the y -axis are fed back into the collective articulation command, and errors about the z -axis are fed back into the differential throttle command. This leads to the proportional derivative control given by

$$\mathbf{u}_\omega = \begin{bmatrix} -K_p & -K_d \end{bmatrix} \begin{bmatrix} \mathbf{e} \\ \boldsymbol{\omega} \end{bmatrix} \quad (8.14)$$

where K_p and K_d are positive semi-definite matrices such that

$$K_p = \begin{bmatrix} k_{p_x} & & \\ & k_{p_y} & \\ & & k_{p_z} \end{bmatrix} \quad (8.15)$$

and

$$K_d = \begin{bmatrix} k_{d_x} & & \\ & k_{d_y} & \\ & & k_{d_z} \end{bmatrix} \quad (8.16)$$

The closed loop, linearized attitude dynamics are then given by

$$\begin{bmatrix} \dot{\mathbf{e}} \\ \dot{\boldsymbol{\omega}} \end{bmatrix} = \begin{bmatrix} \mathbf{0} & I_3 \\ -[B_\omega Y]_\omega K_p & -[B_\omega Y]_\omega K_d \end{bmatrix} \begin{bmatrix} \mathbf{e} \\ \boldsymbol{\omega} \end{bmatrix} \quad (8.17)$$

This control strategy is derived from the decoupled equations that arise from the diagonal structure of $B_\omega Y$. However, this structure arises as a result of the assumptions that $r_y^R = -r_y^L = r_y$ and $r_z = 0$. While these assumptions are not unreasonable since $r_y^R \approx -r_y^L$ and $r_z \ll r_x$, they are not completely accurate. As a result, the equilibrium orientation is not exactly vertical and in the equilibrium condition, the rotors will have non-zero articulation angles and different thrust forces. These deviations from the assumed equilibrium condition give rise to off-diagonal coupling terms in $B_\omega Y$, as defined by Equations B.2–B.13.

The trigonometric functions defining B_ω in Equations B.2–B.13 make it difficult to obtain a closed form solution for decoupling the control inputs in order to restore

nominal performance. Taylor series expansions of the trigonometric functions can be used as an approximation in order to allow for decoupling solutions. Nevertheless, investigations with first order approximations of the coupling effects failed to restore the nominal behavior and second order and higher approximations became too computationally demanding for implementation in the on-board flight control system. Since the attitude coupling effects are minimal, they are neglected here. However, this is an area for future work.

8.4 Position Control

The linearized hovering Z dynamics described by the third row in Equation 8.13 are decoupled from the attitude dynamics and controlled by the collective throttle input. Let the position error be denoted by $\mathbf{e}_R = \mathbf{R} - \mathbf{R}_d = [e_X, e_Y, e_Z]^T$ where \mathbf{R}_d is the desired position. The collective throttle input is commanded by

$$\delta_{coll} = [k_{p_Z}, k_{i_Z}, k_{d_Z}] \begin{bmatrix} e_Z \\ \int e_Z dt \\ \dot{e}_Z \end{bmatrix} + \delta_{coll_0} - \Delta V \frac{C_V}{C_\delta} \quad (8.18)$$

where δ_{coll_0} is the collective throttle setting required for the thrust to equal the vehicle weight and k_{p_Z} , k_{i_Z} , and k_{d_Z} are positive constants. In order to correct for varying battery voltages, the collective throttle input is also adjusted by $-\Delta V \frac{C_V}{C_\delta}$, where ΔV represents the difference in the battery voltage from its nominal charge voltage of 11.1 V such that $\Delta V = V - 11.1$.

In Equation 8.13, the control input α_{coll} is multiplied by a nonzero term in B_R and will result in inputs to the vehicle translational dynamics in the X - Y plane. However, this control input is determined by the inner loop attitude controller as defined by Equation 8.14. Assuming that the attitude controller operates at a sufficiently high frequency, these inputs will be treated as perturbations outside of the position controller bandwidth. Thus, the only other translational dynamics in the X - Y plane come from the vehicle attitude.

In Equation 8.13, rotation about the body y axis causes a force aligned with the earth X axis while rotation about the body z axis causes a force aligned with the earth Y axis. Thus, the outer loop vehicle position control can be achieved by inputs to the desired hovering orientation. Equation 8.13 is based on the linearization of the system dynamics where the vehicle z and y axes are aligned with the Earth X and Y axes respectively. As a result, the outer position control loop can be implemented at arbitrary heading angles by projecting the earth fixed X and Y errors onto the body frame using the heading angle γ_{hdg} given in Equation 8.30 such that,

$$\begin{bmatrix} \mathbf{e}_z & \mathbf{e}_y \end{bmatrix} = \begin{bmatrix} \mathbf{e}_X & \mathbf{e}_Y \end{bmatrix} \begin{bmatrix} \cos \gamma_{hdg} & -\sin \gamma_{hdg} \\ \sin \gamma_{hdg} & \cos \gamma_{hdg} \end{bmatrix} \quad (8.19)$$

where \mathbf{e}_z and \mathbf{e}_y are the translational errors in body frame coordinates and

$$\mathbf{e}_X = \left[X - X_d, \int (X - X_d) dt, \dot{X} - \dot{X}_d \right]^T \quad (8.20)$$

and

$$\mathbf{e}_Y = \left[Y - Y_d, \int (Y - Y_d) dt, \dot{Y} - \dot{Y}_d \right]^T \quad (8.21)$$

Although the responses in Equation 8.13 are of equal magnitude for equivalent angular errors about the y and z axes, separate gains may be desired for rotation about the body y and z axes since they have different methods of actuation with unique actuator dynamics. For a given set of gains $K_y = [K_{p_y}, K_{i_y}, K_{d_y}]$ and $K_z = [K_{p_z}, K_{i_z}, K_{d_z}]$ for the body z and y axes respectively, the desired angular offset is computed as

$$\Delta\gamma = \sqrt{(K_y \mathbf{e}_y)^2 + (K_z \mathbf{e}_z)^2} \quad (8.22)$$

The axis of rotation for the offset, $\Delta\mathbf{u}$, is then defined by

$$\Delta\mathbf{u} = \frac{1}{\sqrt{(K_y \mathbf{e}_y)^2 + (K_z \mathbf{e}_z)^2}} \begin{bmatrix} 0 \\ K_z \mathbf{e}_z \\ -K_y \mathbf{e}_y \end{bmatrix} \quad (8.23)$$

The offset quaternion can then be expressed as

$$\Delta q_d = \begin{bmatrix} \cos \frac{\Delta\gamma}{2} \\ \Delta \mathbf{u} \sin \frac{\Delta\gamma}{2} \end{bmatrix} \quad (8.24)$$

Rotating the equilibrium attitude by this offset quaternion gives the total desired hovering attitude quaternion to be

$$q_{\text{hover}} = q_{d_0} \otimes \Delta q_d \quad (8.25)$$

where q_{d_0} represents the equilibrium hovering attitude that results in zero translational motion.

8.5 Hover Error Correction

The quaternion error derivation in Equation 6.13 results in an error quaternion that connects the measured and desired quaternions along a great circle on the unit three-sphere representing the unit quaternions in 4D Euclidean space [52]. This approach results in a minimum quaternion distance between the measured and desired attitudes where the rotation is achieved by simultaneous rotations about all of the body frame axes. While rotationally efficient, this “smooth” definition of the attitude error can sometimes lead to undesirable intermediate attitudes. For example, consider the hovering case where the desired vehicle orientation is at 90 degrees pitch, given by the unit quaternion

$$q_d = \frac{1}{2} [\sqrt{2}, 0, \sqrt{2}, 0]^T \quad (8.26)$$

Suppose that the vehicle’s measured position is at zero pitch and roll, and yawed to 180 degrees as shown in Figure 8-1. This error is significantly larger than most errors that the vehicle will encounter, however it is useful for illustrating the concept and could occur when the vehicle transitions to hovering after takeoff or level flight. Using Equation 6.15 gives the axis errors to be

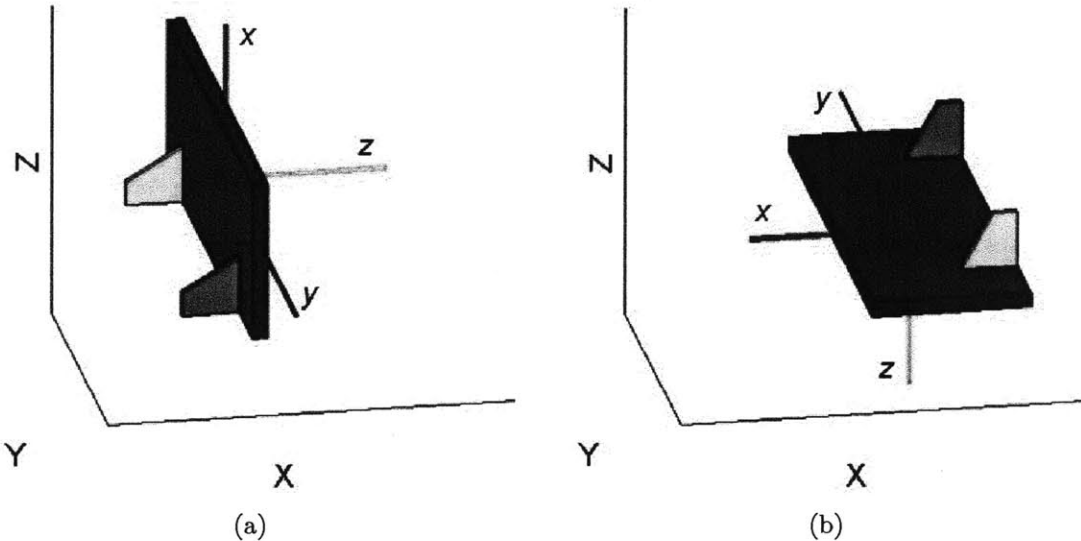


Figure 8-1: Example error calculation scenario with (a) desired and (b) measured orientations.

$$\begin{aligned}
 e_x &= 2.22 \\
 e_y &= 0.0 \\
 e_z &= -2.22
 \end{aligned} \tag{8.27}$$

Thus, rather than rotating about the body y -axis up to a vertical orientation and then rotating about the body x -axis to the desired heading, the quaternion axis errors suggest that the angular error be corrected by a combination of rotation about the body x -axis and the body z -axis. While this rotation will achieve the desired orientation, it does not take into account the transient vehicle dynamics or actuator saturation. As a result, if it follows the rotation prescribed by the raw quaternion error, the vehicle will lose altitude and will translate in the earth X - Y plane as it is rotated. This effect could be accounted for by explicitly including the vehicle translational dynamics in the attitude control algorithm. However, in the nested control structure with an inner attitude loop designed about a stationary hovering orientation, this attitude error formulation could result in large position errors. Furthermore, the inner attitude controller will input large differential throttle and differential articulation inputs for large x and z errors. As they deviate farther from the linearization operating point, these inputs will also begin to become more highly coupled, resulting in attenuation

of the linear hovering controller performance.

For hovering, the desired corrective motion is a semi-sequential rotation that first “smoothly” rotates the vehicle about the body y -axis to the desired pitch angle while keeping the wings level by rotating about the z -axis. This rotation orients the vehicle vertically to eliminate translational motion and control coupling. Once vertical, the rotation sequence then rotates the vehicle about the body x -axis to achieve the desired heading. This semi-sequential rotation effectively decouples the heading error from the wings level and pitch errors and allows more emphasis to be placed on the wings level and pitch error to minimize translational motion.

In order to create this semi-sequential error, the desired quaternion is pre-rotated about the earth fixed Z -axis to a heading angle that corresponds to the direction that the belly of the vehicle is facing. The axis errors are then computed as in Equation 6.15 but the body x -axis error is replaced by the negative of the heading angle.

The vehicle heading angle is computed by first taking the projection of the vehicle y and z axes onto the earth axis system as shown in Equations 8.28 and 8.29.

$$\left[0, (\mathbf{y})_E^T \right]^T = q \otimes [0, 0, 1, 0]^T \otimes q^* \quad (8.28)$$

$$\left[0, (\mathbf{z})_E^T \right]^T = q \otimes [0, 0, 0, 1]^T \otimes q^* \quad (8.29)$$

As can be seen in Figure 8-2, the heading angle can then be determined by the projection of the y -axis onto the earth fixed X - Y plane as

$$\gamma_{hdg} = \text{sign}((\mathbf{z})_E \cdot \mathbf{j}) \times \arccos \left(\frac{(\mathbf{y})_E \cdot \mathbf{j}}{\sqrt{[(\mathbf{y})_E \cdot \mathbf{i}]^2 + [(\mathbf{y})_E \cdot \mathbf{j}]^2}} \right) \quad (8.30)$$

where $\mathbf{i} = [1, 0, 0]$ and $\mathbf{j} = [0, 1, 0]$. The heading quaternion is then constructed as

$$q_{hdg} = \left[\cos \frac{\gamma_{hdg}}{2}, 0, 0, \sin \frac{\gamma_{hdg}}{2} \right]^T \quad (8.31)$$

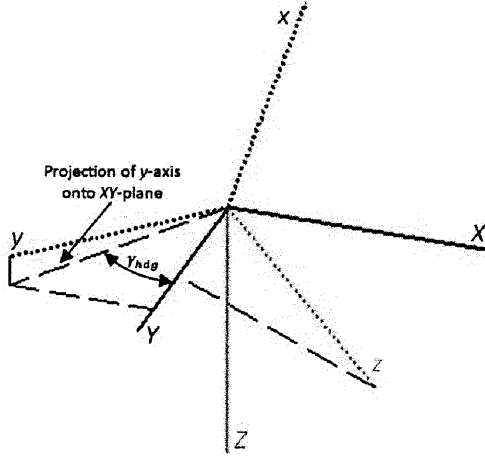


Figure 8-2: Heading angle calculation from y and z axis projections.

Pre-rotating by this quaternion gives the desired quaternion as

$$q_d = q_{hdg} \otimes q_{hover} \quad (8.32)$$

where q_{hover} is the desired attitude quaternion based on the outer loop position controller in Equation 8.25. Using this formulation, the body y and z angular errors are computed as in Equation 6.15 and the x axis error is given as $e_x = -\gamma_{hdg}$. As desired, this method gives the axis angular errors for the previous example to be

$$\begin{aligned} e_x &= 3.14 \\ e_y &= -1.57 \\ e_z &= 0 \end{aligned} \quad (8.33)$$

8.6 Performance

The attitude controller and altitude position controller were successfully implemented on the prototype vehicle. Figure 8-3 shows the vehicle in autonomous hovering flight.



Figure 8-3: Prototype vehicle autonomously hovering with attitude and altitude control.

8.6.1 Attitude Control

Figure 8-4 shows the vehicle attitude responses for impulses about each of the body axes. All three responses in Figure 8-4 exhibit significant overshoot and lightly damped oscillations. These response could be improved by further tuning the controller gains, however, sensor and actuator delays and sensor noise are a limiting factor in the controller performance. As was discussed in Section 8.5, the x axis gains are set lower relative to the other two axes in order to prioritize achieving the desired vertical orientation over the desired heading angle. This choice of gains results in the much slower x axis response shown in Figure 8-4.

8.6.2 Position Control

Figure 8-5 shows the vehicle altitude error during hovering. Although decreasing battery voltage reduces the rotor thrust, the integrated altitude error allow the controller to maintain zero steady state error.

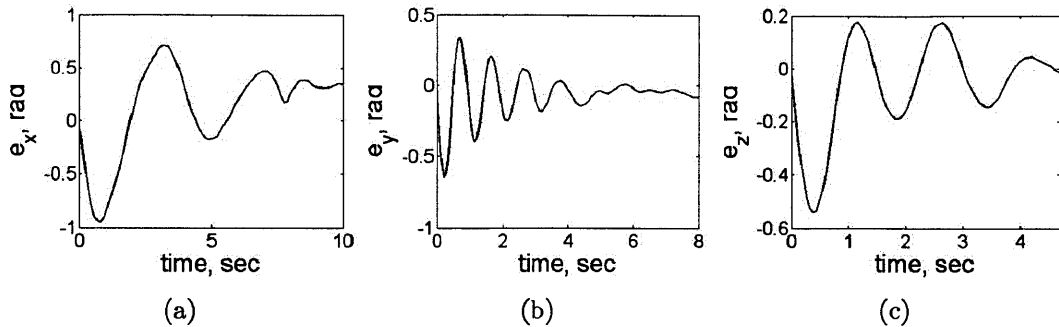


Figure 8-4: Attitude impulse responses. (a) x axis error for a 2.1 rad/sec impulse, (b) y axis error for a 4.9 rad/sec impulse, (c) z axis error for a 2.1 rad/sec impulse.

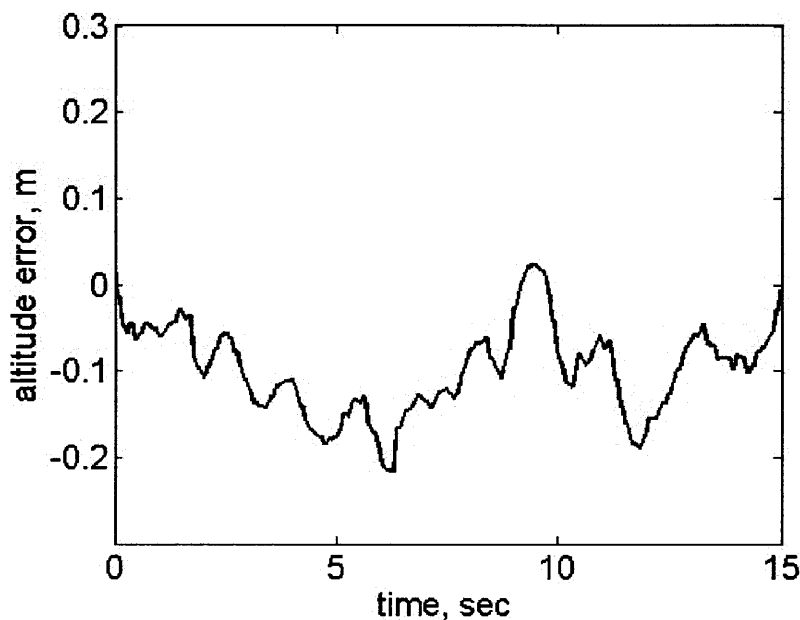


Figure 8-5: Filtered sonar altitude error measurements during hovering flight.

Due to the lack of an integrated translational position feedback sensor in the vehicle flight control system at the time of writing, no experimental results are available for the vehicle X and Y position control. Nevertheless, Figure 8-6 shows the simulated vehicle position response for a 1 m simultaneous X and Y step input assuming a position sensor with a 10 Hz update rate.

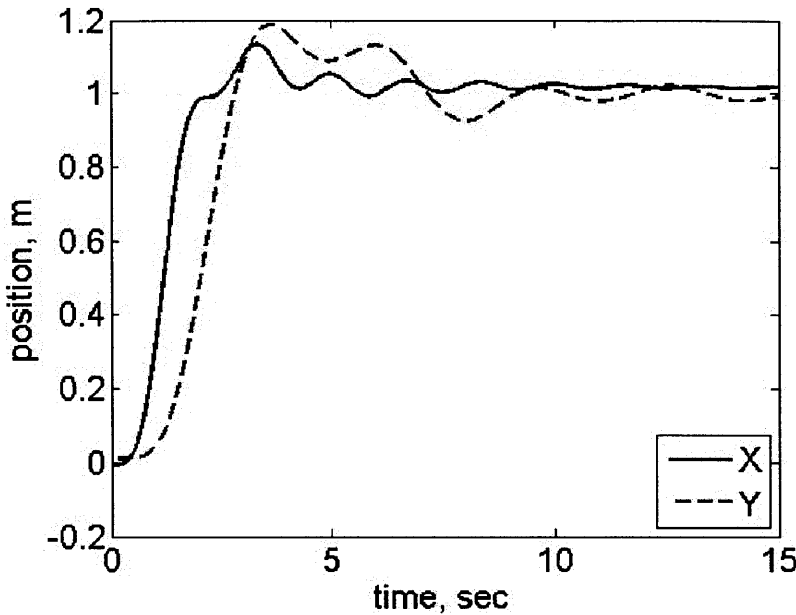


Figure 8-6: Vehicle translational position response to a simultaneous 1 m step input in X and Y .

8.6.3 Hover Region of Attraction Estimation

The feasibility of composing of locally valid feedback controllers to achieve control over a larger portion of the controllable state space is predicated on the ability of each controller to “funnel” the system dynamics from an input region of the state space to a terminal region of the state space that is a subset of the input region of an adjacent controller. For the hovering attitude controller, the input region consists of the region of attraction (ROA) of the state space that can be stabilized to the desired hovering orientation. Identification of this region is necessary for guaranteeing successful transitions between the takeoff and hovering controllers. If, for any starting orientation and pivot location, the takeoff controller is capable of achieving a terminal state that is within the hovering attitude controller ROA, then the transition can occur successfully.

Since the heading angle is arbitrarily defined, the commanded heading can simply be set to the current heading at takeoff. As a result, the ROA analysis need only consider the body y and z axis errors. Figure 8-7 shows experimentally obtained data from the hovering controller where a number of impulses were input about the

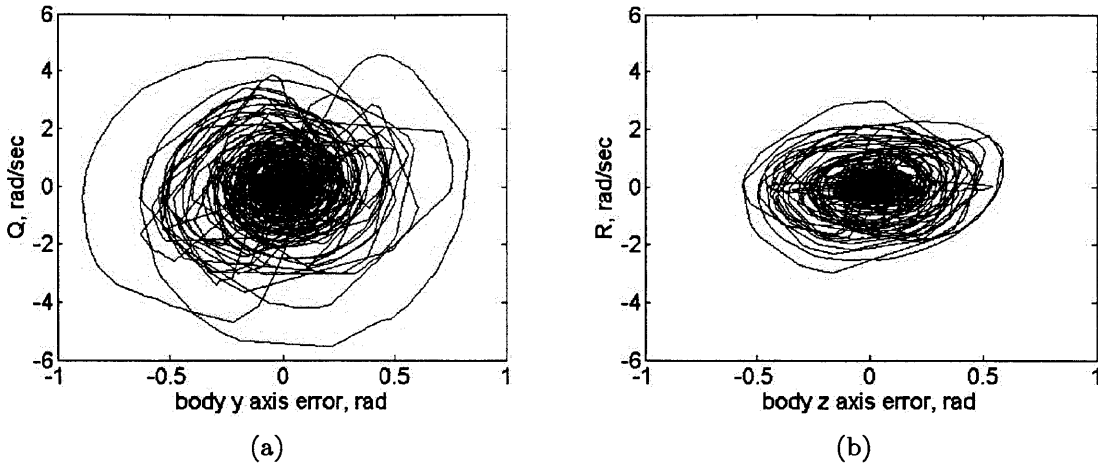


Figure 8-7: Experimental region of attraction data for the body y axis (a) and z axis (b) errors

body y and z axes. Due to spatial constraints, the magnitudes of impulses were limited and the attitude controller was able to stabilize the vehicle for all inputs. As a result, the experimental results provide a conservative estimate of the hovering attitude controller ROA. Nevertheless, the experimental data shows that the hovering controller is capable of stabilizing the vehicle attitude dynamics over a large portion of the state space.

If it is assumed that the roll and yaw dynamics are stabilized during the takeoff maneuver, then the transition between the takeoff and hover controllers can be described by the y axis errors. By setting the roll and yaw errors to zero, the attitude dynamics can be simplified to a 2 degree of freedom model as in Section 9.2. Using the MATLAB SOSTOOLS toolbox [57], Sum of Squares convex optimization tools were used to generate a Lyapunov function for the y axis dynamics, guaranteeing global stability for the closed loop y axis dynamics without delays.

By including delayed actuator states in the hovering dynamics model, the expanding interior, iterative search method proposed by Jarvis-Wloszek in [58], was used to approximate the y axis region of attraction for the hovering controller with actuator delays. The resulting estimate of the region of attraction, projected onto the pitch and pitch rate plane, can be seen in Figure 8-8. As with all sum-of-squares approaches, the region shown Figure 8-8 is a conservative estimate of the true region of attraction.

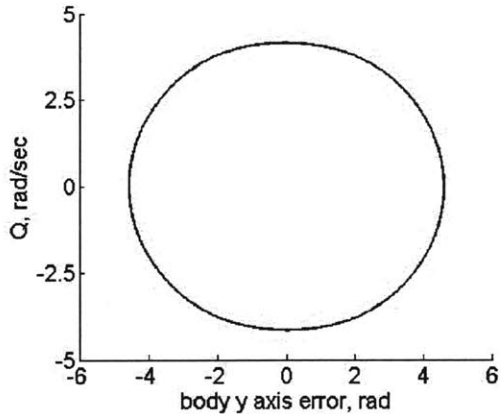


Figure 8-8: Sum-of-squares approximation of the hover controller y axis region of attraction with actuator delays.

Nevertheless, this approximation encompasses a very large portion of the state space. And while the actuator and sensor delays certainly contribute to instability, these results agree with the experimentally obtained data and suggest that the region of attraction may be much larger than Figure 8-7 would indicate.

Although the ROA of the hover controller appears to be quite large, the analysis assumes that the vehicle is already in the air and in a hovering configuration. During the transition from takeoff to hover, the vehicle will be on the ground at a lower throttle setting than required by the hover controller. As a result, the hover controller will be less effective as the rotors accelerate to the desired speeds and the vehicle will not pivot about its center of gravity until the rotors develop enough thrust to lift the vehicle off of the ground. In order to account for these off nominal conditions, the vehicle should be well within the hover controller ROA before switching controllers.

what are the axes of fig 8-8
and how do I relate this figure to the ones in fig 8-7?
I really am unsure what the connection is here

THIS PAGE INTENTIONALLY LEFT BLANK

Chapter 9

Takeoff Control

9.1 Overview

The hover attitude controller is capable of stabilizing the vehicle over most pitch angle and rate configurations, however during takeoff, when it is on the ground, the vehicle will pivot from a location other than its center of gravity. The off-nominal pivot location introduces torque from gravity, increases the vehicle inertia, and affects the control input magnitudes. Furthermore, the linear feedback gains used in the hover controller are designed for operation about a vertical orientation. As a result, switching to the hover controller at low pitch angles could result in significant control coupling and transient translational dynamics. During takeoff, while the vehicle is on the ground, translational motion may be impeded by nearby earth obstacles. Accordingly, it is desired that the vehicle be in an orientation near vertical with a low pitch rate before switching to the hover controller.

By keeping the rotors oriented vertically, the takeoff controller is designed to minimize translational motion as the vehicle is rotated to a vertical orientation. A dynamic inversion of the pitch dynamics is used to cancel the nonlinear vehicle dynamics. A linear feedback policy is then implemented on the linearized dynamics. In order to prevent control saturation and improve the controller bandwidth, two separate feedback control strategies are implemented based on the vehicle pitch angle.

A switching algorithm is proposed for transferring control between the takeoff

and hovering controllers. The controller switching condition accounts for delays in the actuator responses during the transfer and smooths the control input signal at the transfer. Results are presented from takeoff tests.

9.2 Pitch Only Model

The takeoff maneuver consists primarily of a pitch up motion to a vertical orientation. Nominally, with zero roll error, the desired motion can be accomplished through rotation about the body y axis. In this case, with zero errors about the body x and z axes ($q_1 = q_3 = P = R = 0$), the attitude model can be simplified to

$$\dot{Q} = \frac{\tau_y}{J_{yy} + m(r_{px}^2 + r_{pz}^2)} \quad (9.1)$$

where

$$\tau_y = \tau_{gy} + \tau_{ry} \quad (9.2)$$

$$\tau_{gy} = mg [r_{px} (q_0^2 - q_2^2) + 2q_0 q_2 r_{pz}] \quad (9.3)$$

$$\tau_{ry} = (r_{rz} - r_{px}) (T_L \cos \alpha_L + T_R \cos \alpha_R) + (r_{rx} - r_{px}) (T_L \sin \alpha_L + T_R \sin \alpha_R) \quad (9.4)$$

$$\dot{q}_0 = -\frac{Q q_2}{2} \quad (9.5)$$

and

$$\dot{q}_2 = \frac{Q q_0}{2} \quad (9.6)$$

Noting that $q_0 = \cos \theta/2$ and $q_2 = \sin \theta/2$ for a pure pitch rotation of θ degrees, Equations 9.3 and 9.5 can be rewritten as

$$\tau_{gy} = mg (r_{px} \cos \theta + r_{pz} \sin \theta) \quad (9.7)$$

$$\dot{\theta} = Q \quad (9.8)$$

The x offset term ($r_{rx} - r_{px}$) in Equation 9.4 will be approximately two orders of magnitude greater than the z offset term ($r_{rz} - r_{px}$). Similarly, the pivot z location

r_{p_z} in Equation 9.7 will typically be several orders of magnitude smaller than r_{p_x} . As a result, the dynamics can be further simplified to include only the torques caused by displacements in the x direction.

$$\tau = (r_{r_x} - r_{p_x}) (T_L \sin \alpha_L + T_R \sin \alpha_R) + m g r_{p_x} \cos \theta \quad (9.9)$$

9.3 Takeoff Trajectory

The primary constraints on the takeoff trajectory come from the motor and servo dynamics. In order to be controllable, the pitch up maneuver must be performed at a rate that is within the bandwidth of the servos and motors. The takeoff controller goal of reaching a vertical orientation with zero rotational rate implies an upper bound on the pitch rate and angular acceleration. Experimental data suggests that the vehicle dynamics remain within the actuator bandwidth for angular rates below 4 rad/sec.

In order to satisfy the constraints on the takeoff maneuver, the desired trajectory is parameterized by a maximum pitch rate, a pitch angular acceleration, and a pitch angular deceleration. As shown in Figure 9-1, the desired pitch trajectory starts at rest and is accelerated until it reaches the maximum pitch rate or the angular distance needed to decelerate at the specified rate is equal to the current angular distance from vertical. When the angular distance needed to decelerate is equal to the current angular distance from vertical, the desired trajectory is decelerated until the pitch rate reaches zero at a pitch angle of $\pi/2$ rad.

As will be shown in Section 9.5, the relationship between the pitch angle and rate is critical for successful transition to the hover controller. As a result, feedback control is implemented on the phase rate error. Thus, for a given pitch angle, the rate error is computed based on the desired trajectory in the phase plane. Since the error is on the pitch rate, derivative feedback is accomplished by measurements of the pitch angular acceleration.

The desired roll angle and rate are held fixed at zero during takeoff. The desired heading angle is set to the vehicle heading and the desired heading rate is zero.

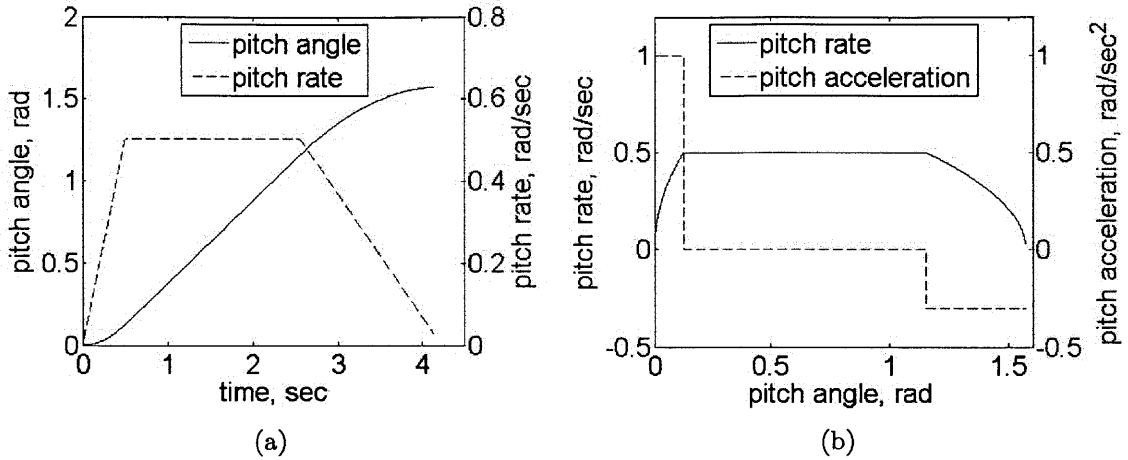


Figure 9-1: Desired takeoff trajectory in time (a) and phase (b) with a maximum pitch rate of 0.5 rad/sec , an angular acceleration of 1.0 rad/sec^2 , and an angular deceleration of -0.3 rad/sec^2 .

9.4 Takeoff Attitude Control

9.4.1 Algorithm

In order to achieve the most efficient pitch control torque, both rotors would be articulated to 90 degrees, causing the $\sin\alpha$ terms in Equation 9.9 to go to 1. Pitch torque could then be controlled through the collective throttle input. However, fixing the rotor articulation angles in this manner would put the rotors in an undesirable orientation for entering hovering flight.

In order to ensure that the rotors are near their desired orientations for hover, the nominal rotor orientation is set at $\alpha_R = \alpha_L = \alpha = \pi/2 - \theta$ so that both rotors point vertically. This articulation choice is also meant to direct the rotor forces parallel the Z axis to prevent translational acceleration on flat surfaces. Since the thrust vectors are parallel, Equation 9.9 can be further simplified by combining the rotor thrust forces as $T = T_R + T_L$. The pitch torque then becomes

$$\tau_y = T(r_{r_x} - r_{p_x}) \cos \theta + m g r_{p_x} \cos \theta \quad (9.10)$$

In Equation 9.10, both the rotor and gravitational torques are functions of the current pitch angle. If the pivot location is known, both of these nonlinearities can

be canceled by letting

$$T = T_0 + \frac{\Delta T}{\cos \theta} \quad (9.11)$$

where

$$T_0 = -\frac{mgr_{px}}{r_{rx} - r_{px}} \quad (9.12)$$

Since the servos are limited in travel to ± 90 degrees, this approach fails for negative pitch angles. When the pitch angle is less than zero, the rotor articulation is saturated at 90 degrees and the pitch torques in Equation 9.9 become

$$\tau_y = T(r_{rx} - r_{px}) + mgr_{px} \cos \theta \quad (9.13)$$

Based on Equation 9.13, for pitch angles less than zero, the system nonlinearities can be canceled by setting

$$T = T_0 \cos \theta + \Delta T \quad (9.14)$$

where T_0 is defined, as before, by Equation 9.12. Using the thrust input $T = T_0 + \frac{\Delta T}{\cos \theta}$ for pitch angles greater than zero, and $T = T_0 \cos \theta + \Delta T$ for pitch angles less than zero, the pitch torque becomes linear with ΔT such that

$$\tau_y = \Delta T(r_{rx} - r_{px}) \quad (9.15)$$

Based on the linear thrust model developed in Equation 7.20, T_0 and ΔT can be mapped to throttle inputs δ_{coll_0} and $\Delta\delta_{coll}$ that maintain the linearity of the canceled dynamics. As a result, using these cancellations, the pitch dynamics reduce to a linear system given by

$$\dot{Q} = \frac{2\Delta\delta_{coll}}{C_\delta} \frac{(r_{rx} - r_{px})}{J_{yy} + m(r_{px}^2 + r_{pz}^2)} \quad (9.16)$$

Since T_0 is a constant that is dependent on the unknown pivot location, an initial adaptation phase can be implemented that quickly initializes δ_{coll_0} for the takeoff maneuver. Slower adaptation through the use of integrators can then be included to fine tune δ_{coll_0} during the maneuver.

For pitch angles near $\pi/2$, scaling the throttle by $1/\cos \theta$ will result in large magni-

tude throttle inputs. These inputs may saturate the motor and ESC or exceed their bandwidth. As a result, if used at large pitch angles, this control strategy may cease to be able to control the pitch dynamics.

To account for the large magnitude throttle inputs that arise at large pitch angles, for pitch angles above $\pi/4$ the throttle is fixed at the nominal collective throttle defined by T_0 in Equation 9.12. Pitch control is then achieved by articulating the rotors about the vertical orientation such that $\alpha = \pi/2 - \theta + \Delta\alpha$. With this control implementation, the pitch torque becomes

$$\tau_y = (r_{r_x} - r_{r_p}) T_0 \cos(\theta - \Delta\alpha) + mgr_{p_x} \cos\theta \quad (9.17)$$

$$= (r_{r_x} - r_{r_p}) T_0 (\cos\theta \cos\Delta\alpha + \sin\theta \sin\Delta\alpha) + mgr_{p_x} \cos\theta \quad (9.18)$$

If it is assumed that $\Delta\alpha$ is small, then Equation 9.18 can be approximated by

$$\tau_y = (r_{r_x} - r_{r_p}) T_0 (\cos\theta + \Delta\alpha \sin\theta) + mgr_{p_x} \cos\theta \quad (9.19)$$

$$= -mgr_{p_x} \Delta\alpha \sin\theta \quad (9.20)$$

As before, the nonlinear sine term in Equation 9.20 can be canceled by redefining the articulation angle as $\alpha = \pi/2 - \theta + \Delta\alpha/\sin\theta$. The approximate linearized dynamics are then given by

$$\dot{Q} = \Delta\alpha \frac{-mgr_{p_x}}{J_{yy} + m(r_{p_x}^2 + r_{p_z}^2)} \quad (9.21)$$

For both segments of the takeoff maneuver, the control inputs are computed by PID gains on the pitch rate phase error such that

$$\Delta\delta_{coll} = -K_T \mathbf{e}_\theta, \text{ and } \Delta\alpha = -K_\alpha \mathbf{e}_\theta \quad (9.22)$$

where

$$\mathbf{e}_\theta = \left[Q - Q_d, \int (Q - Q_d) dt, \dot{Q} - \dot{Q}_d \right]^T \quad (9.23)$$

$$K_T = [K_{p_T}, K_{i_T}, K_{d_T}] \quad (9.24)$$

and

$$K_\alpha = [K_{p_\alpha}, K_{i_\alpha}, K_{d_\alpha}] \quad (9.25)$$

and the integrated error is saturated at $\theta_{i_{max}}$.

An additional, lower gain unsaturated integrator on the rate phase error is fed back into the nominal collective throttle input to correct for errors in the initialization process such that

$$\delta_{coll_0} = \delta_{coll_0_{initial}} - K_{i_{\theta_{slow}}} \int (Q - Q_d) dt \quad (9.26)$$

The vehicle roll error is fed back into differential throttle control such that

$$\delta_{diff} = -K_\phi \mathbf{e}_\phi \quad (9.27)$$

where

$$K_\phi = [K_{p_\phi}, K_{i_\phi}, K_{d_\phi}] \quad (9.28)$$

and

$$\mathbf{e}_\phi = \left[\phi, \int \phi dt, P \right]^T \quad (9.29)$$

where ϕ is defined as the Euler roll angle.

Since off center pivot locations can cause large gravitational torques about the roll axis, a relatively large roll integrator gain is used to ensure that zero roll is reached quickly. The roll integrator is saturated to prevent excessive overshoot.

For positive pitch angles, the yaw rate is feed back into the differential rotor articulation to prevent excessive yawing during the maneuver.

$$\alpha_{diff} = K_{d_\psi} R \quad (9.30)$$

The takeoff control algorithm can be summarized as a composition of the three phases described below:

Initialization

1. Set desired pitch rate and angular acceleration to zero.
2. Set the integral errors and the baseline collective throttle, $\delta_{coll_0_{initial}}$ to zero.

- Set the pitch rate Q_{adapt} where the adaption phase stops to a fixed value greater than zero.

Phase I - Baseline Throttle Adaption

- Articulate both rotors to an angle of $\pi/2 - \theta$ rad.
- Increase baseline collective throttle, $\delta_{coll_0_{initial}}$ at a fixed rate.
- If the pitch angle is less than zero, set the collective throttle input to $\delta_{coll} = \delta_{coll_0_{initial}} \cos \theta$. Otherwise, set the collective throttle input to $\delta_{coll} = \delta_{coll_0_{initial}}$.
- If the pitch rate is greater than Q_{adapt} , fix $\delta_{coll_0_{initial}}$ at the current value and go to Phase II. Otherwise, remain in Phase I.

Phase II - Throttle Control

- Articulate both rotors to an angle of $\pi/2 - \theta$ rad.
- Set the desired pitch rate and angular acceleration based on desired phase trajectory at current pitch angle.
- Apply pitch rate, integrated rate, and acceleration feedback on the collective throttle such that $\Delta\delta_{coll} = -K_T \mathbf{e}_\theta$.
- Set $\delta_{coll_0} = \delta_{coll_0_{initial}} - K_{i_{\theta_{slow}}} \int (q - q_d) dt$.
- If the pitch angle is less than zero, set the collective throttle input to $\delta_{coll} = \delta_{coll_0} \cos \theta + \Delta\delta_{coll}$. Otherwise, set the collective throttle input to $\delta_{coll} = \delta_{coll_0} + \frac{\Delta\delta_{coll}}{\cos \theta}$.
- If $\theta > \pi/4$, go to Phase III. Otherwise stay in Phase II.

Phase III - Rotor Articulation Control

- Set $\delta_{coll} = \delta_{coll_0_{initial}} - K_{i_{\theta_{slow}}} \int (q - q_d) dt$.
- Set the desired pitch rate and angular acceleration based on the desired phase trajectory at current pitch angle.
- Set the collective rotor articulation to $\alpha_{coll} = \pi/2 - \theta + \Delta\alpha/\sin\theta$, where $\Delta\alpha = -K_\alpha \mathbf{e}_\theta$.
- If the switching conditions described in Section 9.5 are met, switch to the hovering controller, set the desired heading angle to the current heading angle, and command an initial altitude above the ground. Otherwise, if $\theta < \pi/4$, go to Phase II . If neither of these conditions are met, stay in Phase III.

The roll and yaw feedback defined in Equations 9.27 and 9.30 are applied to the differential throttle and rotor articulation commands throughout the entire takeoff maneuver.

The switching pitch rate, Q_{adapt} should be a small positive value. However, it should be large enough that it exceeds the sensor noise threshold. In the following results, a value of 0.15 rad/sec was used for the switching rate condition.

9.4.2 Performance

Simulation and experimental data confirm that the takeoff controller is capable of achieving a terminal state that is well within the hover controller ROA. Figure 9-2 shows a simulated pitch response from a flat, horizontal surface along with five experimentally obtained responses for the same conditions with a maximum commanded pitch rate of 0.5 rad/sec , an angular acceleration of 1.0 rad/sec^2 , and an angular deceleration of 0.3 rad/sec^2 . The experimental results show significant variation in the takeoff controller performance. These variations are likely due to unmodeled aerodynamic interactions, sensor noise, and perturbations such as battery voltage fluctuations that are not completely compensated for by the throttle adjustment and variation in motor and ESC performance due to thermal effects. Nevertheless, in each test, the vehicle reaches a vertical pitch orientation with a pitch rate below 2 rad/sec .

In some of the tests, the vehicle pitch angle undershoots the desired 90 degree orientation, resulting in a pitch oscillation indicated by a loop in the phase plane. These cases resulted in the highest observed pitch rates.

In Figure 9-4, pitch responses are plotted for multiple takeoff rotations starting from various surfaces and orientations. The 100 mm inboard pivot plots come from positioning the vehicle on a wood block parallel to the trailing edge with its back edge 100 mm from the vehicle trailing edge as shown in Figure 9-3(a). The 100 mm and 200 mm offset tests involved securing a carbon fiber rod to the left wingtip that extended to the specified distance behind the trailing edge as in Figure 9-3(b). It is not realistic that the vehicle would have such a protrusion during normal operation, however, these offsets force the vehicle to pivot about a point that is far from the

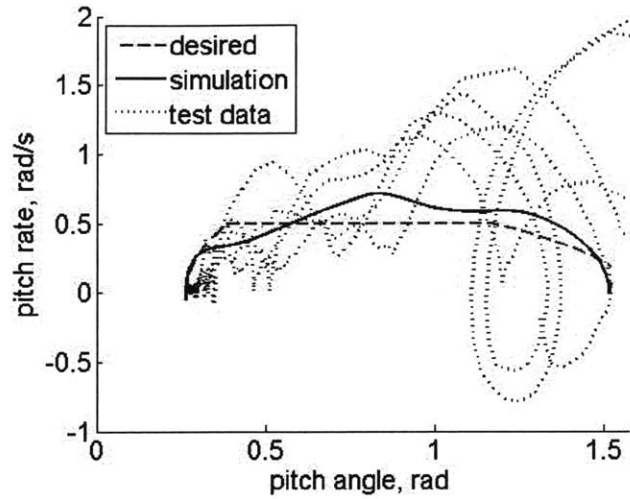


Figure 9-2: Simulated pitch response with five experimental results for a takeoff rotation from a flat, horizontal surface.

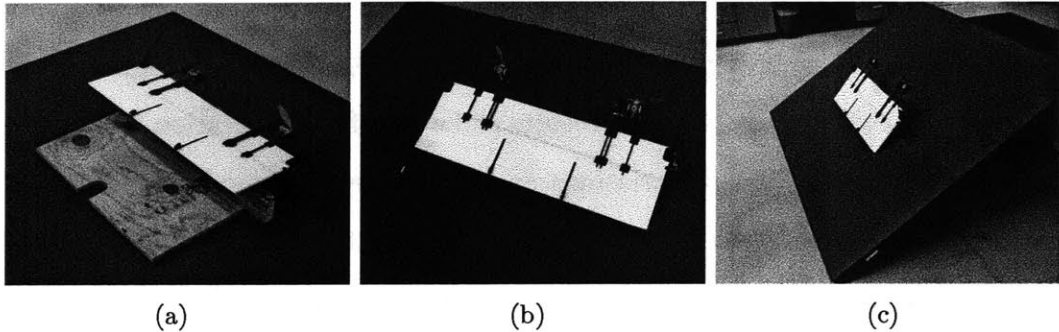


Figure 9-3: Off-nominal test setups: (a) 100 mm inboard pivot, (b) 200 mm offset, and (c) 30 deg incline.

trailing edge and the center of gravity. In doing so, they exaggerate the change in dynamics that comes from taking off from an unknown surface. Additionally, as the vehicle rotates up, the offset causes a large roll error that is used to simulate a takeoff where the vehicle is positioned sideways on an inclined surface. In experiments, tests of the takeoff maneuver from inclined surfaces with the vehicle pointing sideways resulted in the vehicle sliding off the surface and rotating from the flat ground at the base of the incline. As a result, these offset tests provide a more convenient way to test the vehicle's ability to correct for large roll perturbations. The inclined and declined tests were performed from a surface oriented at the specified angle as shown in Figure 9-3(c).

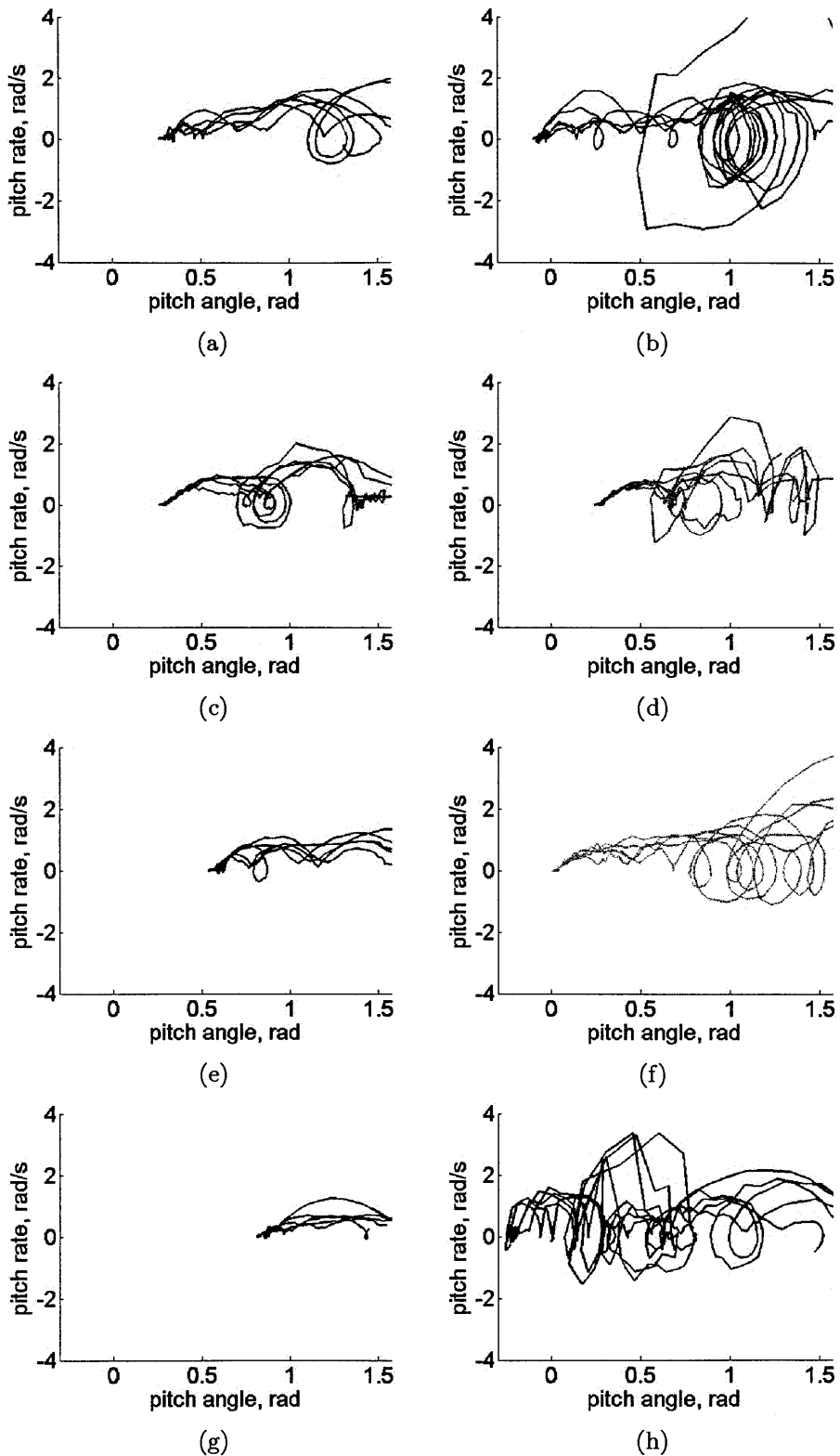


Figure 9-4: Takeoff test data from the following surfaces and configurations: (a) flat, level surface, (b) 100 mm inboard pivot, (c) 100 mm offset, (c) 200 mm offset, (e) 15 degree incline, (f) 15 degree decline, (g) 30 degree incline, (h) 30 degree decline.

Some of the trajectories in Figure 9-4 exhibit significant oscillations due to the vehicle translational motion over the off-nominal terrains. In many cases, the vehicle would slide off the inclined or declined surface or pivot offset and experience an oscillation as the vehicle pivot location changed or encountered a flat surface. Nevertheless, even with these oscillations, the controller still reaches a vertical orientation with a relatively low pitch rate in most cases.

9.5 Switching Algorithm

The takeoff switching algorithm must ensure that the vehicle is within the hover controller ROA and near a vertical orientation before switching to the hover controller. These criteria will be met by imposing a minimum pitch angle for switching to the hover controller. Assuming that the pitch angle is above the minimum prescribed value, the objective of the switching algorithm will be to minimize the pitch overshoot and translational motion that occur during the transition between controllers.

Figure 9-5 shows the takeoff trajectories from Figure 9-4 plotted with a number of simulated hover trajectories starting from points along the $Q = 0$ axis. In most cases, the takeoff controller trajectories start out crossing the hover trajectories towards trajectories that are closer to the desired hovering attitude. Accordingly, at the time that the takeoff trajectory goes from moving towards more favorable hovering trajectories to less favorable trajectories, the takeoff trajectory and the hovering trajectory will be tangent. Assuming that switching between controllers results in an instantaneous transfer between trajectories and that the takeoff and hover trajectories will cross only once, at their first point of tangency, the optimal switching point would be at points of tangency between the two controller trajectories. In the case of an undershoot, where the takeoff controller trajectory fails to reach 90 degrees of pitch, the trajectories will become tangent at $Q = 0$, thus this switching method also implies a lower rate bound.

Such a switching algorithm can be accomplished by using the vehicle hovering dynamics model to approximate the hover controller trajectory at the current point

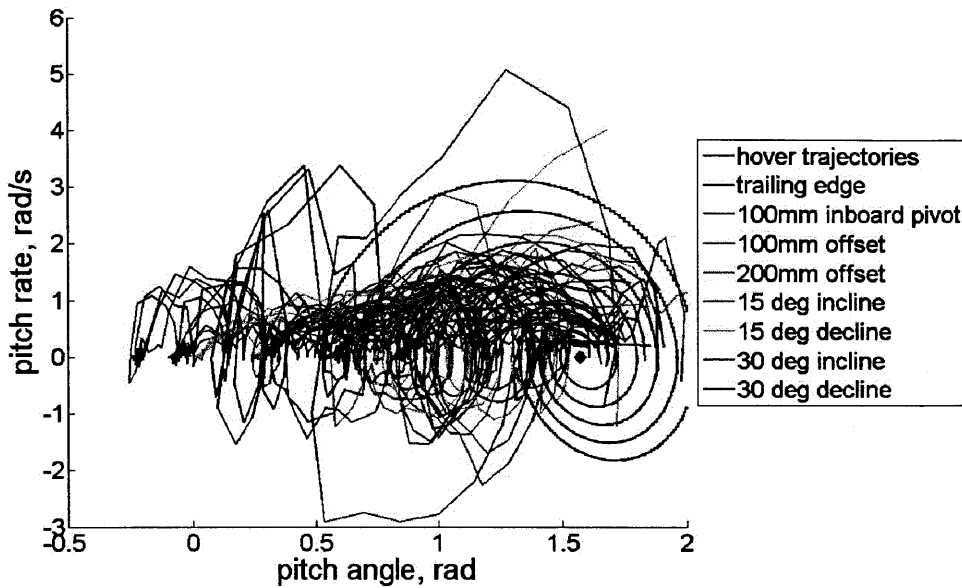


Figure 9-5: Experimental pitch responses for takeoff rotations from a variety of terrains and starting orientations with simulated hovering responses.

in the phase plane and using the measured pitch rate and angular acceleration to estimate the takeoff pitch trajectory. If the two estimates are within a specified tolerance of tangency, the vehicle can be commanded to switch from the takeoff controller to the hover controller. Since the vehicle will takeoff when the hover controller is activated, control cannot be switched back to the takeoff controller. As a result, this method evaluates the performance of the takeoff controller conservatively. Experimental results indicate that the takeoff trajectories typically have multiple points of tangency with the approximate hover trajectories and, even though they may experience some oscillations, typically achieve improved performance if the switching is delayed beyond the first point of tangency.

Furthermore, this approach is model dependent and, due to the discrete nature of the control implementation, it can fail to identify points of tangency if sensor measurements are not taken near enough to the actual time of tangency. Such a failure could result in the vehicle rotating past vertical. This can be accounted for by a maximum angle limit that forces the transfer to happen, however, this approach could still result in an undesirable transfer at a pitch angle near vertical and a large

angular rate.

The transfer decision is further complicated by actuator delays and the fact that the hovering model assumes that the vehicle is in the air and free to rotate about its center of gravity with no torques due to gravity. In reality, when the transfer occurs, the vehicle is still on the ground, pivoting about some point other than its center of gravity. Since the throttle response is delayed by the motor and rotor dynamics, the vehicle remains on the ground until the thrust is greater than vehicle weight.

The servo responses are also delayed, however, they are much faster than the motor responses. Accordingly, the desired rotor articulation angle is reached while the thrust is still much less than desired. This effect, coupled with the increased vehicle rotational inertia due to rotation about a point other than the center of gravity, results in a reduction in pitch control authority. The pivot location also results in a pitch torque due to the vehicle weight that causes an angular acceleration acting in opposition to the feedback controller.

Figure 9-6 shows the simulated hovering responses that would occur if the phase tangency switching conditions were applied to the experimental data shown in Figure 9-4. A maximum angle and minimum rate limit are also included to ensure that even with sensor delays, the transfer occurs before the vehicle reaches 90 degrees of pitch or zero pitch rate. The sharp corners in the hovering trajectories occur when the vehicle leaves the ground. These responses are verified by the experimental takeoff trajectory using the same switching conditions shown in Figure 9-7.

Based on the results in Figures 9-6 and 9-7, neglecting the transient vehicle response during the controller transition will result in significant, undesirable oscillations about the desired hovering pitch angle. In the experimental tests, this implementation also resulted in significant translational motion during the oscillations that occurred while the vehicle was still on the ground. In spaced constrained environments such motion could cause collisions (only one experimental trajectory is shown because the vehicle did, in fact, collide with a wall after taking off using this approach).

Since the pitch control authority decreases during the controller transition, an

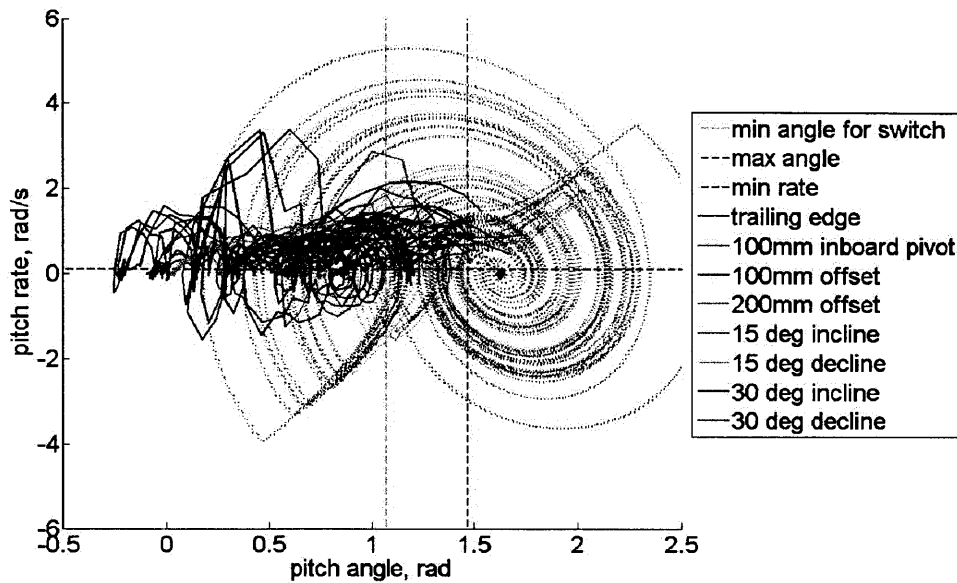


Figure 9-6: Simulated hovering responses after switching from experimentally obtained takeoff trajectories based on a minimum rate constraint of 0.1 rad/sec , a maximum angle constraint of $\pi/2 - 0.1 \text{ rad}$, and phase tangency switching with a tolerance of $\pm 0.1 \text{ rad/sec}$ for pitch angles above 1.07 rad . Simulated responses are displayed as dotted lines, while the experimental data is shown as solid lines.

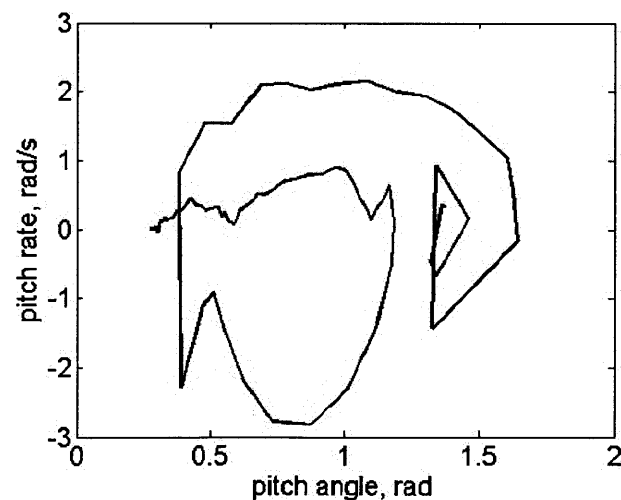


Figure 9-7: Experimentally obtained takeoff trajectory based on a minimum rate constraint of 0.1 rad/sec , a maximum angle constraint of $\pi/2 - 0.1 \text{ rad}$, and phase tangency switching with a tolerance of $\pm 0.1 \text{ rad/sec}$ for pitch angles above 1.07 rad .

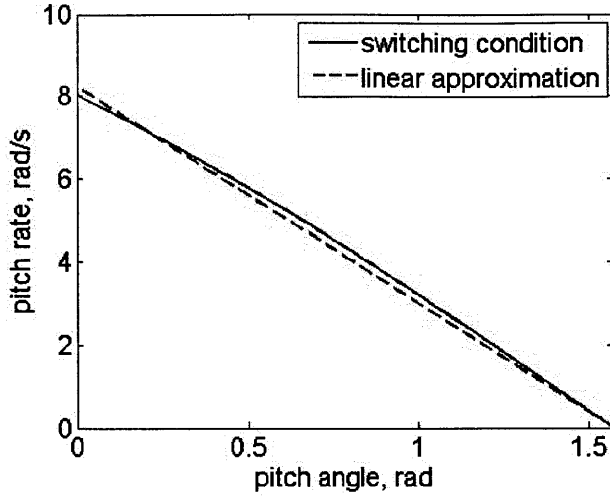


Figure 9-8: Energy based switching condition and linear approximation

alternative energy based approach to the tangency switching condition is to switch at a point in the phase plane where, in the absence of any control inputs, the vehicle will continue to rotate from its current pitch angle and stop in a vertical orientation. For the simplified, pitch only dynamics in Equation 9.9, this condition is met when

$$Q = \sqrt{\frac{2r_{px}(\sin\theta - 1)mg}{J_{yy} + mr_{px}^2}} \quad (9.31)$$

Figure 9-8 shows a plot the solutions of Equation 9.31 for a pivot location at the vehicle trailing edge. Figure 9-8 also includes a line that intersects the zero rate axis at a pitch angle of $\pi/2$ rad and is tangent to the curve defined by Equation 9.31 at a pitch angle of $\pi/4$ rad. The straight line approximation appears to provide a good approximation for the switching condition in the range of angles where the switching will occur.

The slope of the line approximating the switching condition is dependent on the unknown pivot location r_{px} . However, as shown in Figure 9-9, the slope remains within 10% of the slope with the pivot at the trailing edge for pivot locations from the trailing edge to within 5 cm of the trailing edge.

Even with reduced authority, the takeoff controller will exert a torque on the vehicle that will cause over-rotation if the energy based switching condition is used.

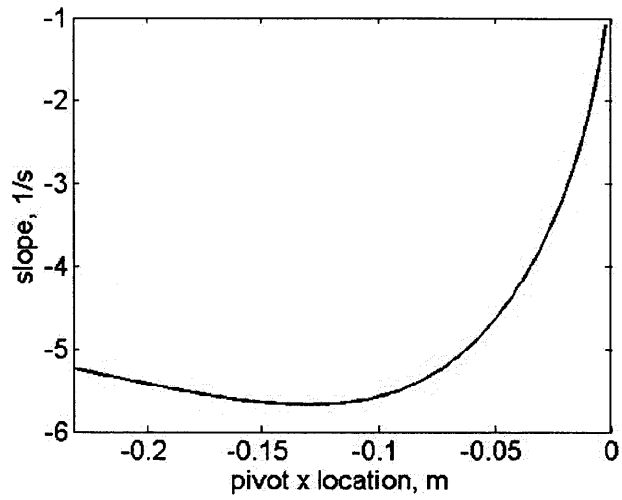


Figure 9-9: Slope of Equation 9.31 evaluated at $\pi/4$ rad

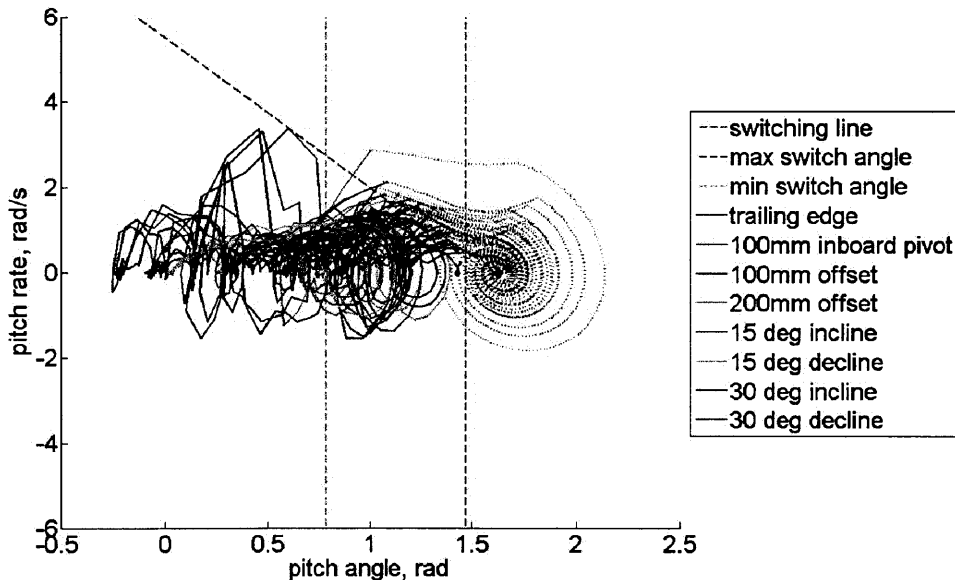


Figure 9-10: Simulated hovering responses after switching from experimentally obtained takeoff trajectories with an energy based switching condition with a slope of -3.5 rad/sec and a maximum angle of $\pi - 0.1 \text{ rad}$ for pitch angles above $\pi/4 \text{ rad}$. Simulated responses are displayed as dotted lines, while the experimental data is shown as solid lines.

Accordingly, the slope of the switching line is reduced from the trailing edge slope of -5.24 1/sec to -3.5 1/sec which represents approximately 46 % of the kinetic energy required to reach a vertical orientation from the trailing edge. From Figure 9-9, it can be seen that this choice of slope will result in switching at a pitch rate that is less than the rate required by all pivot locations farther than 2.5 cm aft of the center of gravity. Although this switching condition limits the maximum takeoff pitch angle to $\pi/2$, an additional upper angle limit can be imposed to force switching for trajectories that are close to a vertical orientation. Figure 9-10 shows the simulated takeoff responses using these switching conditions.

Figure 9-11 shows test data from takeoffs from a flat, horizontal surface using the same energy based switching conditions as in Figure 9-10. Unlike the simulations, the experimental data shows the pitch angle dropping off immediately after the controller transfer. This drop in the pitch angle was accompanied by significant translational acceleration. In order to help correct for this effect, the rotor collective articulation input is offset by a time decaying value such that,

$$\alpha_{\text{off}} = \left(\frac{\pi}{2} - \theta_0 - \alpha_{\text{hover}_0} \right) \exp \left(-\frac{t - t_0}{\tau_{\text{decay}}} \right) \quad (9.32)$$

where α_{off} is the offset added to the hover collective articulation input, θ_0 is the pitch angle at the transfer time t_0 , α_{hover_0} is the rotor collective articulation angle commanded by the hover controller at the transfer time, and τ_{decay} is the decay time constant. This offset smooths the jump in the servo input at the transfer and effectively adds additional delay to the servo response to match the motor response and partially offsets the gravitational torque as the rotor thrust increases and the hover controller regains pitch control authority.

Figure 9-12 shows the simulated takeoff trajectories with the energy based switching condition and the servo offset. Although this simulation shows more overshoot than Figure 9-10, the experimental results presented in Section 9.6 resulted in fewer oscillations during the transfer and less translational motion.

Because of its close proximity to the ground, the sonar occasionally outputs er-

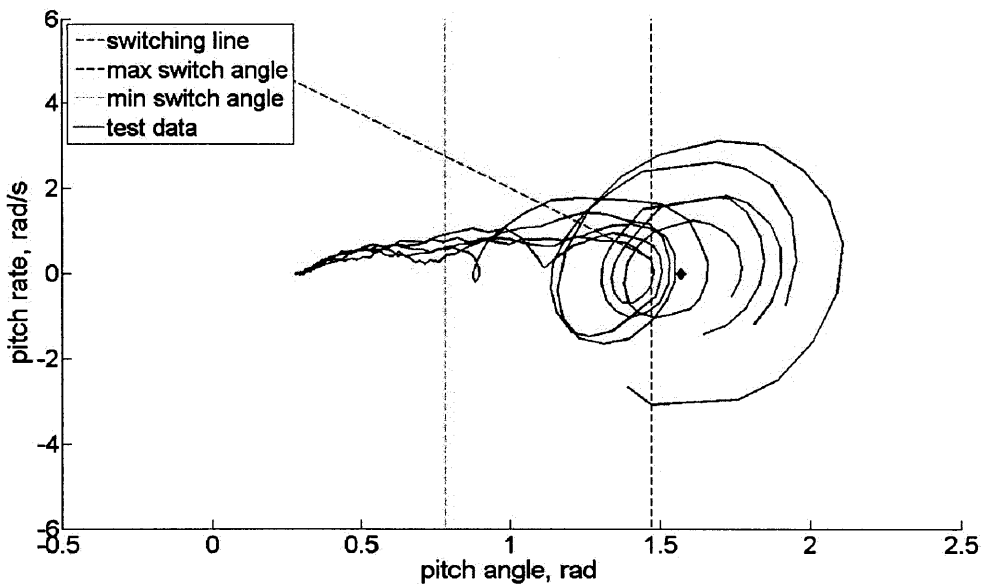


Figure 9-11: Experimental responses with energy based switching conditions with a slope of -3.5 rad/sec and a maximum angle of $\pi - 0.1 \text{ rad}$ for pitch angles above $\pi/4 \text{ rad}$.

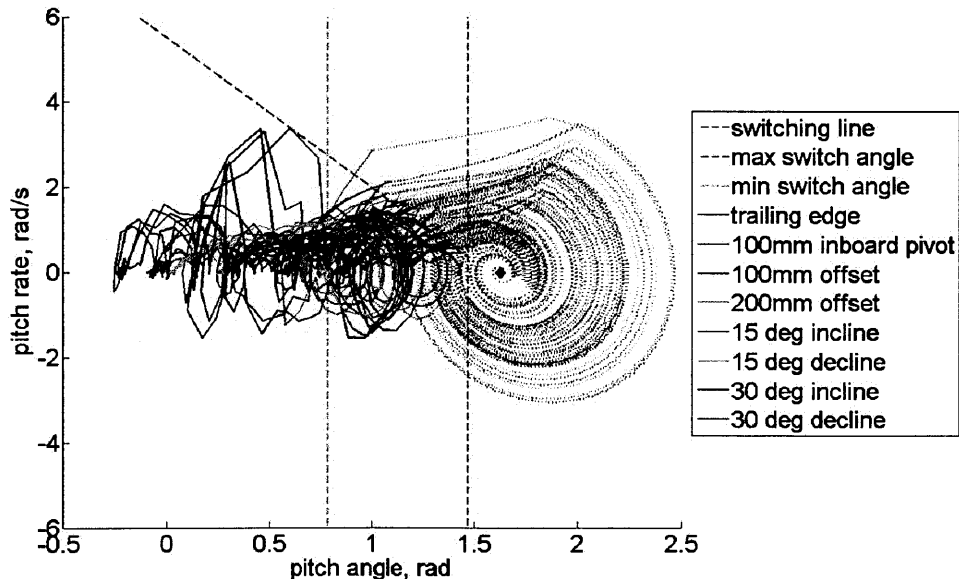


Figure 9-12: Simulated hovering responses after switching from experimentally obtained takeoff trajectories with an energy based switching condition with a slope of -3.5 rad/sec and a maximum angle of $\pi - 0.1 \text{ rad}$ for pitch angles above $\pi/4 \text{ rad}$. Servo input is offset at the controller transfer with a decay time constant of 77 ms. Simulated responses are displayed as dotted lines, while the experimental data is shown as solid lines.

roneously large range readings at takeoff. This error can significantly reduce the collective throttle commanded by the hovering controller at takeoff, resulting in insufficient control authority and a crash during the transfer. In order to correct for this issue, the altitude integral error is set such that at the transfer time,

$$\int e_Z dt = \min\left(-\frac{K_{p_Z} e_Z}{K_{i_p}}, 0\right) \quad (9.33)$$

Thus, the starting throttle commanded by the hovering controller is at least the nominal value for thrust to equal weight for hovering flight.

9.6 Experimental Takeoff Results

Figure 9-13 show the results of implementing the takeoff algorithm described in the previous section. Takeoff tests were conducted on flat ground from the trailing edge, a 100 mm inboard pivot, and a 200 mm offset on one wingtip as shown in Figure 9-3. Incline and decline tests were not conducted due to spatial constraints. The pitch time responses are shown in Figure 9-14. All tests resulted in successful takeoffs with little translational motion.

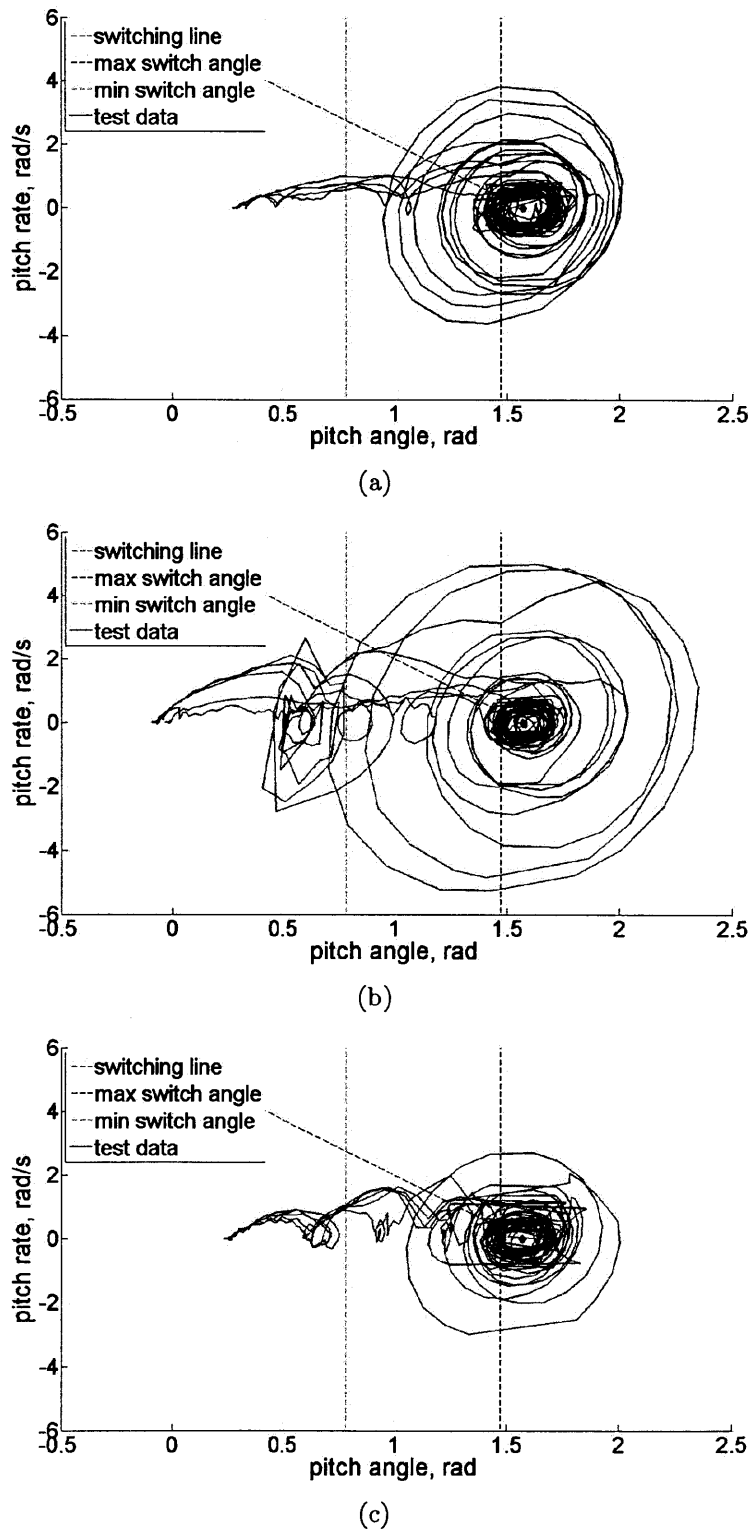


Figure 9-13: Experimental pitch responses for takeoffs with an energy based switching condition with a slope of -3.5 rad/sec and a maximum angle of $\pi - 0.1 \text{ rad}$ for pitch angles above $\pi/4 \text{ rad}$. Servo input is offset at the controller transfer with a decay time constant of 77 ms.

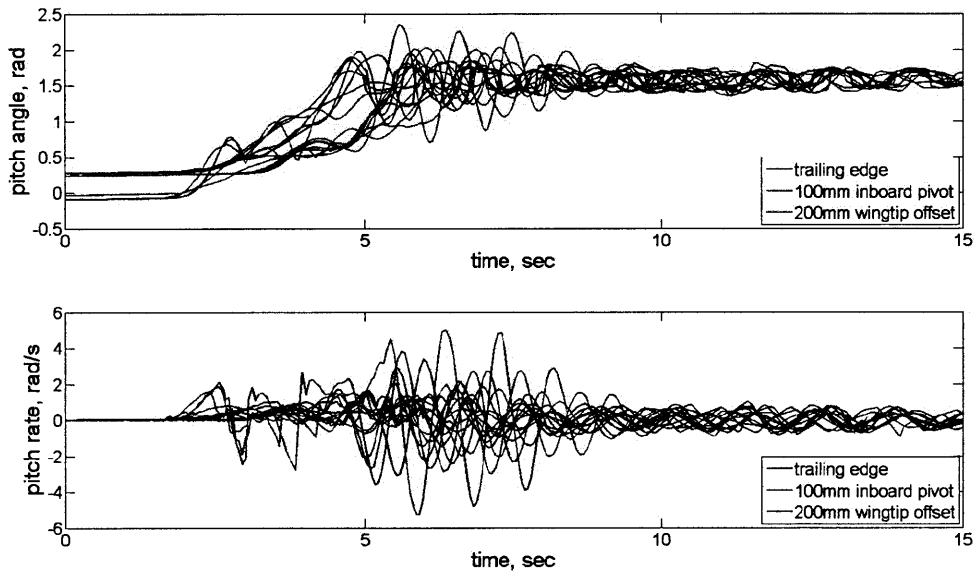


Figure 9-14: Pitch time histories for takeoffs with an energy based switching condition with a slope of -3.5 rad/sec and a maximum angle of $\pm\pi - 0.1 \text{ rad}$ for pitch angles above $\pi/4 \text{ rad}$. Servo input is offset at the controller transfer with a decay time constant of 77 ms.

Chapter 10

Conclusions and Recommendations for Future Work

10.1 Conclusions

Analysis of the proposed vehicle design configuration indicates the existence of a feasible small UAV design capable of achieving continuous flight over a large portion of the day. A composition of locally valid feedback controllers is implemented to demonstrate the autonomous takeoff and hovering flight capabilities of the proposed vehicle design. Experimental results show successful takeoffs from a variety of diverse, unprepared terrains. These capabilities provide the first step towards achieving extended small UAV missions through a combination of energy harvesting and power management approaches. A final design will provide for expanded UAV functionality and integration with military and civilian applications at reduced costs.

10.2 Future work

The work presented here addresses only a small component of the challenges required to realize a viable solution for small, long endurance unmanned vehicles. Future work should be directed towards the following areas:

Improved Controller and Vehicle Designs

Although takeoffs were successfully performed from a number of different terrains and starting orientations, the takeoff maneuver proved to be more challenging than initially anticipated. The primary difficulty occurred during the transition between controller modes where actuator delays and discontinuous control input signals resulted in undesirable transient behaviors. Based on the simulated and observed responses, switching conditions that determined where the controller transfer occurred were designed to shape the transient behavior. Additional time decaying inputs had to be included in the hover controller to smooth the rotor articulation input during the controller transfer.

The difficulties experienced during the control transfer motivate further research into alternative controller and vehicle designs. The use of a nonlinear controller that does not require discrete controller states would eliminate the controller transfer problem. Nevertheless, since most nonlinear control design approaches are highly model dependent, the takeoff rotation while the vehicle is on the ground could prove to be more difficult. Similar to the approach presented in Section 9.4, an initial adaption period could be implemented to initialize model parameters. Even though a nonlinear controller would not function in discrete modes, the trajectory would still be designed to reflect the mission phases in Table 5.1. This phase information could be incorporated into an adaptive controller by varying the adaption rates and controller bandwidth based on the mission phase.

Vehicle design is another potential solution to the takeoff control issue. A vehicle design that does not require the same takeoff rotation would create less variation in the system dynamics. This would simplify the control problem and would allow for easier implementation of nonlinear controllers.

Figure 10-1 shows a conceptual design for a vehicle that would remain horizontal during the takeoff maneuver. The concept has four articulated rotors. The primary lifting rotors are driven by two contra rotating motors. By positioning

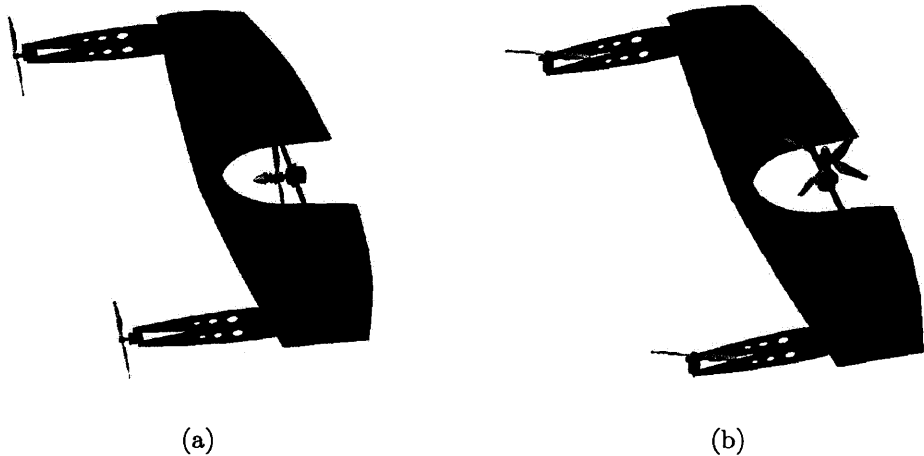


Figure 10-1: Conceptual design of a vehicle capable of performing the desired takeoff maneuver without the pitch up rotation in (a) Level flight and (b) takeoff-hover.

the primary lifting rotors in the wing, near the center of gravity, these rotor could be fixed in either a horizontal or vertical orientation for level flight (see Figure 10-1(a)) or hovering (see Figure 10-1(b)) respectively.

The two rotors located in front of the vehicle would provide the necessary attitude control inputs. Since they are located far in front of the vehicle, the two control motors can be significantly smaller than the main lifting motor. As a result, they will provide faster responses and increase the controller bandwidth.

The drawback to the design shown in Figure 10-1 is the additional mass required to support two additional motors and rotors. Further sizing analysis is needed to ensure that the sizing constraints do not have to be relaxed to provide a feasible sized vehicle with this configuration.

Sensor Integration

In order to allow for position control while hovering and accurate waypoint navigation in level flight, a set of position sensors needs to be incorporated into the vehicle design. In typical aircraft applications, GPS, pressure, and inertial sensors are combined through a Kalman filter to provide absolute position estimates. Nevertheless, the vehicle's hovering capability and low stall speed will allow it to operate in cluttered, near earth environments where it is

important, for navigation and collision avoidance purposes, to be able to identify obstacles and provide accurate position estimation relative to those obstacles.

Furthermore, large buildings and features typical of near earth environments can obstruct GPS measurements. If uncorrected by GPS, drift and biases in inertial measurement sensors can develop significant position estimation errors. In [45], the author suggests the use of optical flow sensors for collision avoidance and navigation in urban environments. These sensors are lightweight, low power, and have been demonstrated to successfully enable collision avoidance in small UAVs [59]. Combining these sensors with a conventional GPS and inertial approach will provide increased functionality by allowing for navigation through cluttered, near earth, GPS denied environments.

Autonomous Landing

Like takeoff, the vehicle must demonstrate the capability to land on diverse, unprepared terrains. The landing maneuver should allow for precise position control and orient the vehicle with its wings in a configuration that is suitable for collecting solar energy. The low mass of the vehicle allows it to sustain moderate falls. Thus, a landing control algorithm could simply lower the vehicle to the ground while hovering and then allow it to fall over uncontrolled. Adding a slight pitch forward input when the vehicle reaches ground level could help to ensure that the proper orientation is achieved.

Level Flight Demonstration

To fly efficiently, the vehicle must demonstrate a level flight capability with transitions to and from hover. Such maneuvers have been demonstrated with similar, multi-modal controllers in related work [29, 45].

In order to limit the number of controller modes, simplify the level flight transition, and provide superior flight performance, a nonlinear controller could be designed to replace the hovering and level flight controllers. With the control authority provided by the rotor articulation, a nonlinear flight controller could allow for agile maneuvers to be accomplished easily without adding additional

controller modes. Such a controller will require improved modeling through system identification.

Solar Cell Integration and Mission Demonstration

The multi-segmented mission concept depends on the integration of the solar energy harvesting capability with vehicle power system. The sizing model in Chapter 3 suggests that with the integration of solar cells, the vehicle will be able to achieve continuous flight from one hour after sunrise to one hour before sunset. However, these results need to be confirmed in hardware. A more detailed sizing and performance model with improved aerodynamic and mass models specifically tailored to the vehicle design and rough sizing will allow for more accurate sizing based on the mission requirements. Furthermore, a full mission demonstration with multiple takeoff, landing, and charge cycles will verify the mission feasibility.

Payload Integration The vehicle must be capable of supporting one or more payloads. In addition to supplying the required payload mass and power, the vehicle should include the communications infrastructure for passing information between the payload and the user. Support for an open architecture payload will increase the vehicle utility by allowing for diverse missions and, potentially, the cooperation of different payloads operating on multiple UAVs.

Design Optimization For a final implementation, the vehicle design must be optimized to provide the lowest mass and power required for cruise flight. In addition to structural and aerodynamic design, considerations must be taken to minimize actuator power demands. For example, using worm gears on the servos rather than a planetary gear set would ensure that the servo could not be back driven by torques on the motor and rotor. This would effectively eliminate any servo holding power required in a static, trim condition.

The design must also be made robust to environmental factors such as rain. Either ducts or protective enclosures should be included on the rotors to protect them from being damaged by ground strikes.

THIS PAGE INTENTIONALLY LEFT BLANK

Appendix A

Sonar Validation and Test Data

Tests were conducted with the MaxBotix XL-MaxSonar-AE2 to determine its performance over variable terrain, its ability to detect objects centered in its beam, and the effect of motor noise on range measurements. All tests were performed with the sensor in its installed configuration.

A.1 Surface Test

Range measurements were taken at 0.25, 0.30, 0.50, and 0.80 m over asphalt, dirt, gravel, grass, and a 0.30 m tall bush. The surfaces can be seen in Figure A-1. Each configuration was sampled 100 times at 10 Hz.

The test results for each height are shown in Figure A-2. This data indicates that the sensor is able to function across a wide range of surfaces. For surfaces other than the bush, the sensor reports consistent readings at all distances at or above 0.30 m. The reported range typically does not vary by more than a centimeter in these tests. At 0.25 m, the sensor readings vary more significantly. However, the variations still do not exceed 3 cm.

There are some small (~ 1 cm) differences between the reported ranges for the different surfaces. Nevertheless, this is more likely due to sensor placement error than a measurement error.

For ranges above 0.30 m, Figure A-2 also shows that the sensor detects the top

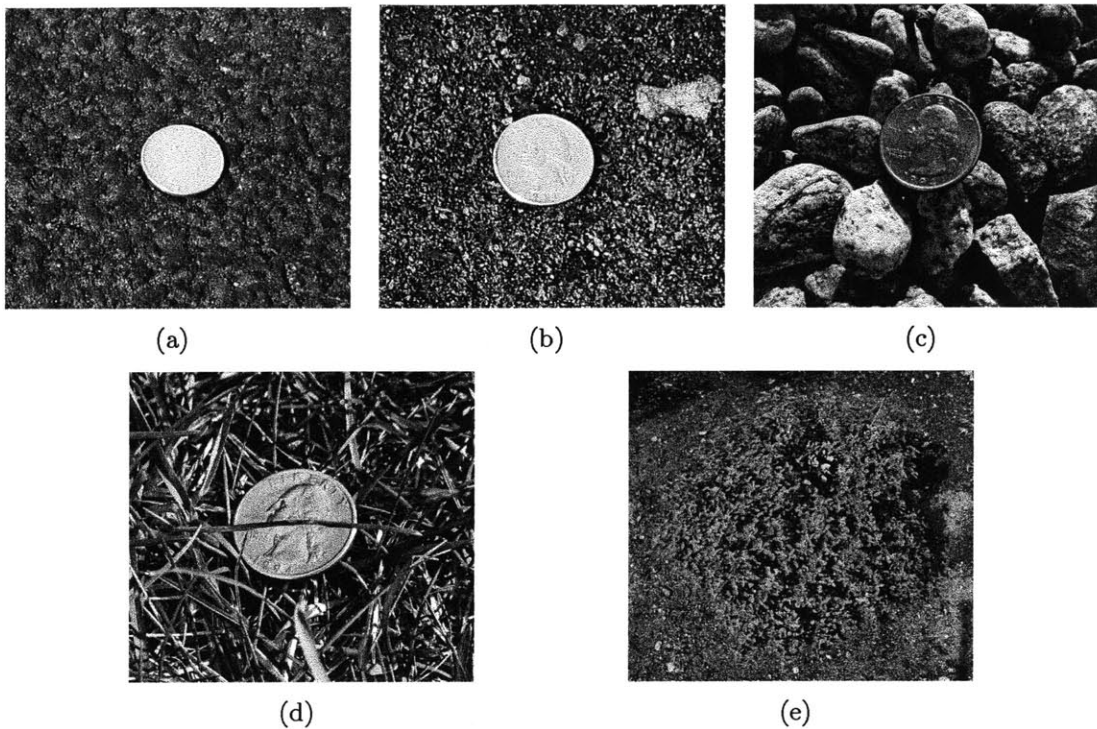
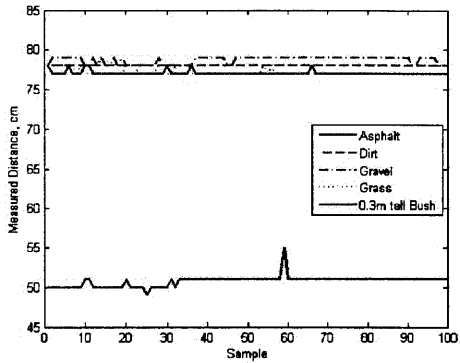


Figure A-1: Test surfaces: (a) asphalt, (b) dirt, (c) gravel, (d) grass, and (e) 0.3m bush.

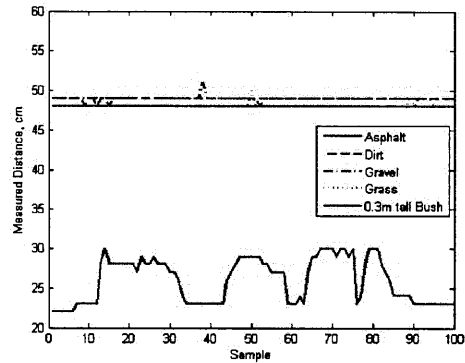
of the bush at the correct height. At 0.80 m the readings have similar variability to the other surfaces. As the sensor is lowered, the measurements begin to vary more significantly. At 0.3 m from the ground, the sensor is at the surface of the bush. The high readings (up to ~ 450 cm) are likely due to the sensor's internal filter treating the multiple return signals from the leaves as noise and choosing a reflected signal as the truth value.

A.2 Target Test

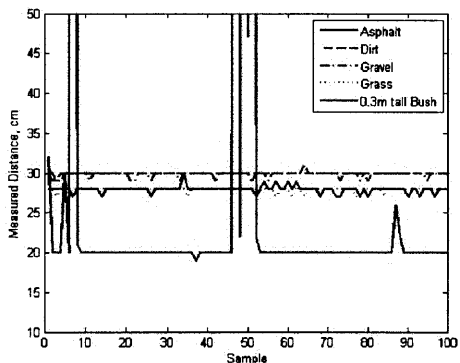
In order to evaluate the sensor's object detection capability, range measurements were taken while the sensor was pointed at a series of target objects. Range measurements were taken indoors at 0.50, 1.0, 2.0, 5.0, and 7.0 m. A horizontal wall was used as the reference and measurements were taken 1.0 m above the ground. Three different sized cardboard boxes, shown in Figure A-3(a), were used as the test targets. A test setup with one of the targets can be seen in Figure A-3(b). The dimensions of the boxes



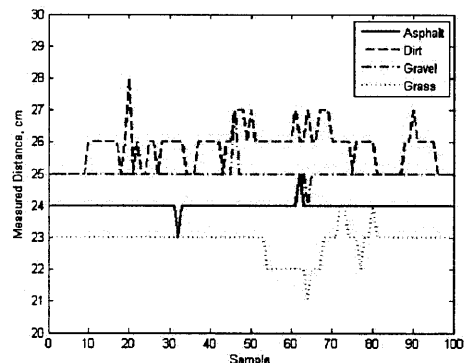
(a)



(b)



(c)



(d)

Figure A-2: Range measurements from (a) 0.80 m, (b) 0.50 m, (c) 0.30 m, and (d) 0.25 m.

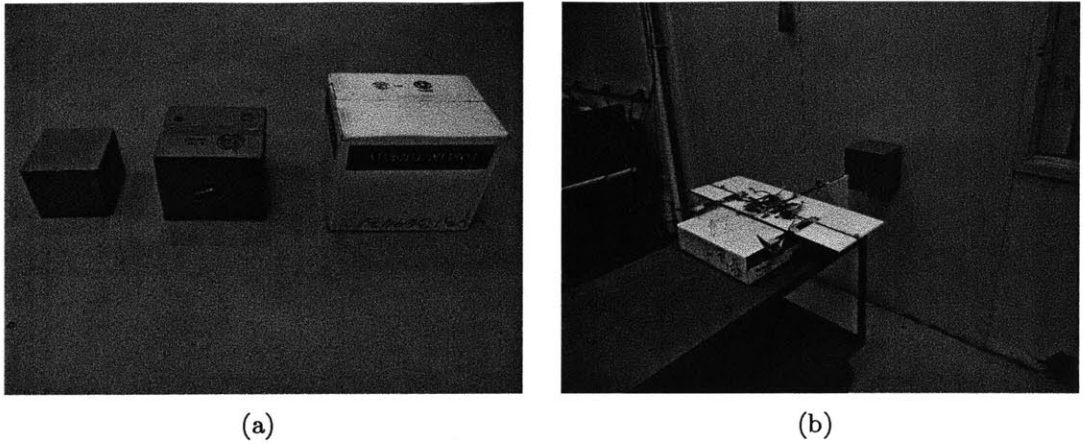


Figure A-3: Target test (a) targets and (b) test setup.

Table A.1: Target dimensions

Target	Length, cm (parallel to floor)	Width, cm (perpendicular to floor)	Height, cm (perpendicular to wall)
Small Box	22	22	19.5
Medium Box	30.5	262	26
Large Box	44	34	36

are given in Table A.1.

The test results are presented in Figure A-4. Although there appears to be a bias of approximately 3 cm, for distances less than 5 m the sensor correctly detected all targets. At distances of 5 m and greater, the signal to noise ratio drops below 1. The bad readings are likely due to reflections from the floor or other objects in the room. This effect could be mitigated by raising the test setup higher off the ground. Even with this low signal to noise ratio, the data is still useful since the readings never drop below 340 cm and improve as the distance to the target decreases.

A.3 Interference Test

A final test was conducted to ensure that the sensor readings would not be affected by the motor and rotor noise. To do this, the sensor was pointed at the wall as in Figure A-3(b) and measurements were taken at 0.5 m and 1.0 m from the wall with the motors off and at 75% throttle. The results, shown in Figure A-5, indicate that

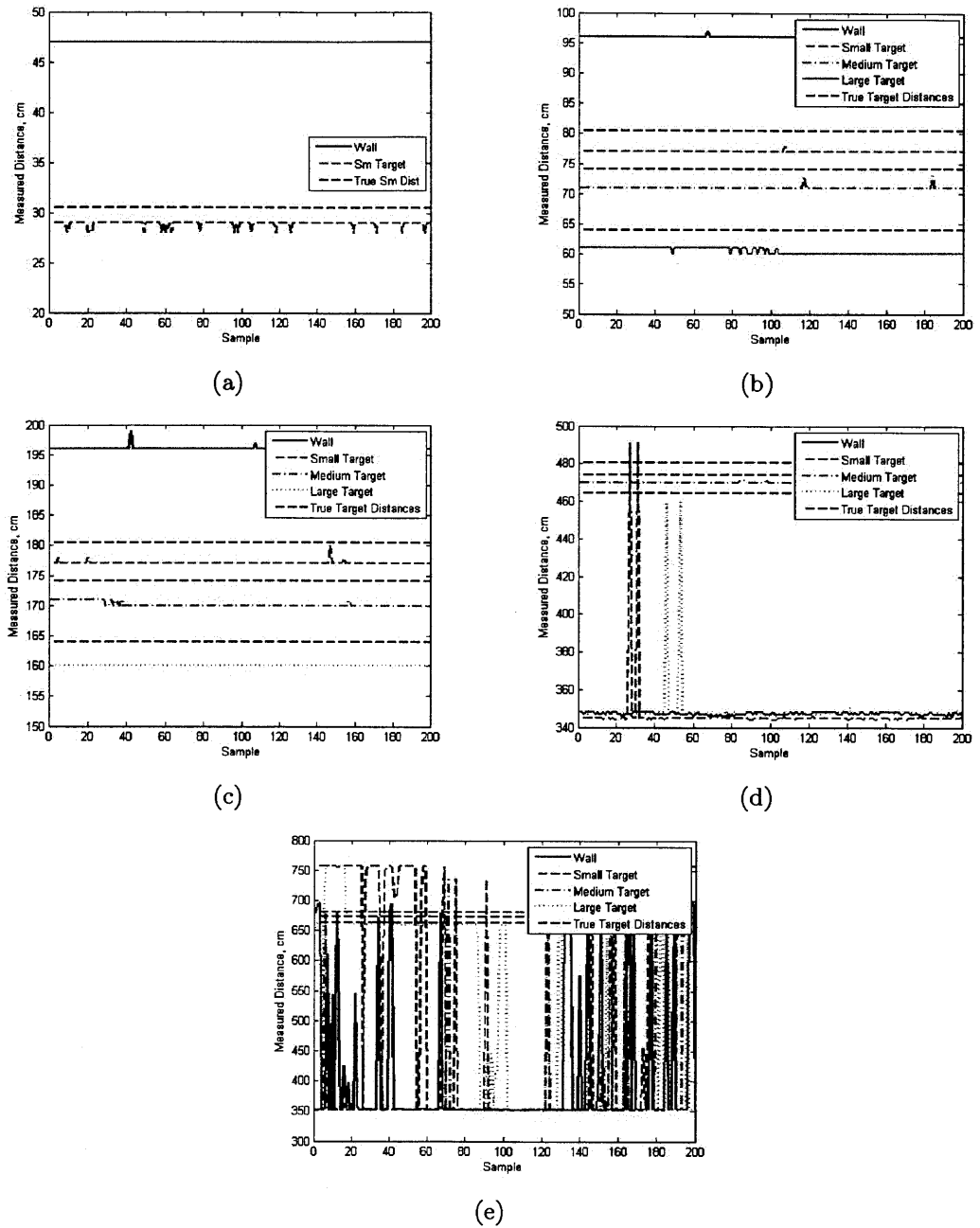


Figure A-4: Target test results from (a) 0.5 m, (b) 1.0 m, (c) 2.0 m, (d) 5.0 m, and (e) 7.0 m

minimal signal noise is added by turning the motors on.

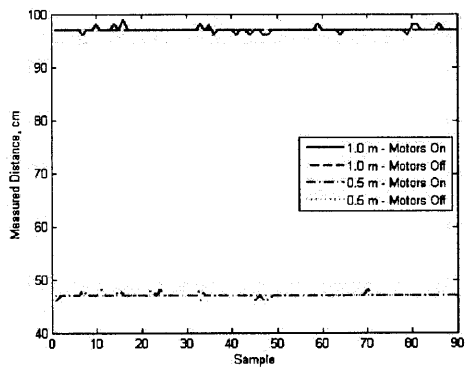


Figure A-5: Motor interference test results

Appendix B

Linearization Details

The linearized input matrix for the vehicle rotational dynamics is

$$B_{\omega} = \begin{bmatrix} B_{\omega_{1,1}} & B_{\omega_{1,2}} & B_{\omega_{1,3}} & B_{\omega_{1,4}} \\ B_{\omega_{2,1}} & B_{\omega_{2,2}} & B_{\omega_{2,3}} & B_{\omega_{2,4}} \\ B_{\omega_{3,1}} & B_{\omega_{3,2}} & B_{\omega_{3,3}} & B_{\omega_{3,4}} \end{bmatrix}_O \quad (\text{B.1})$$

where the O subscript indicates evaluation at the operating point and the individual matrix elements are defined by

$$B_{\omega_{1,1}} = -\frac{1}{J_{xx}} T_R r_{r_y}^R \cos \alpha_R \quad (\text{B.2})$$

$$B_{\omega_{1,2}} = -\frac{1}{J_{xx}} T_L r_{r_y}^L \cos \alpha_L \quad (\text{B.3})$$

$$B_{\omega_{1,3}} = -\frac{1}{J_{xx}} r_{r_y}^R \sin \alpha_R \quad (\text{B.4})$$

$$B_{\omega_{1,4}} = -\frac{1}{J_{xx}} r_{r_y}^L \sin \alpha_L \quad (\text{B.5})$$

$$B_{\omega_{2,1}} = \frac{T_R}{J_{yy}} (r_{r_x} \cos \alpha_R - r_{r_z} \sin \alpha_R) \quad (\text{B.6})$$

$$B_{\omega_{2,2}} = \frac{T_L}{J_{yy}} (r_{r_x} \cos \alpha_L - r_{r_z} \sin \alpha_L) \quad (\text{B.7})$$

$$B_{\omega_{2,3}} = \frac{1}{J_{yy}} (r_{r_z} \cos \alpha_R + r_{r_x} \sin \alpha_R) \quad (\text{B.8})$$

$$B_{\omega_{2,4}} = \frac{1}{J_{yy}} (r_{r_z} \cos \alpha_L + r_{r_x} \sin \alpha_L) \quad (\text{B.9})$$

$$B_{\omega_{3,1}} = \frac{1}{J_{zz}} T_R r_y^R \sin \alpha_R \quad (\text{B.10})$$

$$B_{\omega_{3,2}} = \frac{1}{J_{zz}} T_L r_y^L \sin \alpha_L \quad (\text{B.11})$$

$$B_{\omega_{3,3}} = -\frac{1}{J_{zz}} r_y^R \cos \alpha_R \quad (\text{B.12})$$

$$B_{\omega_{3,4}} = -\frac{1}{J_{zz}} r_y^L \cos \alpha_L \quad (\text{B.13})$$

Similarly, the linearized vehicle translational dynamics are described by

$$A_R = \begin{bmatrix} A_{R_{1,1}} & A_{R_{1,2}} & A_{R_{1,3}} \\ A_{R_{2,1}} & A_{R_{2,2}} & A_{R_{2,3}} \\ A_{R_{3,1}} & A_{R_{3,2}} & A_{R_{3,3}} \end{bmatrix}_O \quad (\text{B.14})$$

where

$$A_{R_{1,1}} = \frac{2}{m} (q_1 q_2 - q_0 q_3) (T_L \sin \alpha_L + T_R \sin \alpha_R) \quad (\text{B.15})$$

$$\begin{aligned} A_{R_{1,2}} = & -\frac{1}{m} [2(q_0 q_2 + q_1 q_3) (T_L \cos \alpha_L + T_R \cos \alpha_R) \\ & + (q_0^2 + q_1^2 - q_2^2 - q_3^2) (T_L \sin \alpha_L + T_R \sin \alpha_R)] \end{aligned} \quad (\text{B.16})$$

$$A_{R_{1,3}} = \frac{2}{m} (q_1 q_2 - q_0 q_3) (T_L \cos \alpha_L + T_R \cos \alpha_R) \quad (\text{B.17})$$

$$A_{R_{2,1}} = \frac{1}{m} (q_0^2 - q_1^2 + q_2^2 - q_3^2) (T_L \sin \alpha_L + T_R \sin \alpha_R) \quad (\text{B.18})$$

$$\begin{aligned} A_{R_{2,2}} = & \frac{1}{m} [2(q_0 q_1 + q_2 q_3) (T_L \cos \alpha_L + T_R \cos \alpha_R) \\ & - (q_1 q_2 + q_0 q_3) (T_L \sin \alpha_L + T_R \sin \alpha_R)] \end{aligned} \quad (\text{B.19})$$

$$A_{R_{2,3}} = \frac{1}{m} (q_0^2 - q_1^2 + q_2^2 - q_3^2) (T_L \cos \alpha_L + T_R \cos \alpha_R) \quad (\text{B.20})$$

$$A_{R_{3,1}} = \frac{2}{m} (q_0 q_1 + q_2 q_3) (T_L \sin \alpha_L + T_R \sin \alpha_R) \quad (\text{B.21})$$

$$\begin{aligned} A_{R_{3,2}} = & -\frac{1}{m} [(q_0^2 - q_1^2 - q_2^2 + q_3^2) (T_L \cos \alpha_L + T_R \cos \alpha_R) \\ & - 2(q_0 q_2 - q_1 q_3) (T_L \sin \alpha_L + T_R \sin \alpha_R)] \end{aligned} \quad (\text{B.22})$$

$$A_{R_{3,3}} = \frac{2}{m} (q_0 q_1 + q_2 q_3) (T_L \cos \alpha_L + T_R \cos \alpha_R) \quad (\text{B.23})$$

and the linearized translational input matrix is given by

$$B_R = \begin{bmatrix} B_{R_{1,1}} & B_{R_{1,2}} & B_{R_{1,3}} & B_{R_{1,4}} \\ B_{R_{2,1}} & B_{R_{2,2}} & B_{R_{2,3}} & B_{R_{2,4}} \\ B_{R_{3,1}} & B_{R_{3,2}} & B_{R_{3,3}} & B_{R_{3,4}} \end{bmatrix}_O \quad (\text{B.24})$$

$$B_{R_{1,1}} = -\frac{T_R}{m} [2(q_0q_2 + q_1q_3) \cos \alpha_R + (q_0^2 + q_1^2 - q_2^2 - q_3^2) \sin \alpha_R] \quad (\text{B.25})$$

$$B_{R_{1,2}} = -\frac{T_L}{m} [2(q_0q_2 + q_1q_3) \cos \alpha_L + (q_0^2 + q_1^2 - q_2^2 - q_3^2) \sin \alpha_L] \quad (\text{B.26})$$

$$B_{R_{1,3}} = \frac{1}{m} [(q_0^2 + q_1^2 - q_2^2 - q_3^2) \cos \alpha_R - 2(q_0q_2 + q_1q_3) \sin \alpha_R] \quad (\text{B.27})$$

$$B_{R_{1,4}} = \frac{1}{m} [(q_0^2 + q_1^2 - q_2^2 - q_3^2) \cos \alpha_L - 2(q_0q_2 + q_1q_3) \sin \alpha_L] \quad (\text{B.28})$$

$$B_{R_{2,1}} = -\frac{2T_R}{m} [(-q_0q_1 + q_2q_3) \cos \alpha_R + (q_1q_2 + q_0q_3) \sin \alpha_R] \quad (\text{B.29})$$

$$B_{R_{2,2}} = -\frac{2T_L}{m} [(-q_0q_1 + q_2q_3) \cos \alpha_L + (q_1q_2 + q_0q_3) \sin \alpha_L] \quad (\text{B.30})$$

$$B_{R_{2,3}} = \frac{2}{m} [(q_1q_2 + q_0q_3) \cos \alpha_R + (q_0q_1 - q_2q_3) \sin \alpha_R] \quad (\text{B.31})$$

$$B_{R_{2,4}} = \frac{2}{m} [(q_1q_2 + q_0q_3) \cos \alpha_L + (q_0q_1 - q_2q_3) \sin \alpha_L] \quad (\text{B.32})$$

$$B_{R_{3,1}} = -\frac{T_R}{m} [(q_0^2 - q_1^2 - q_2^2 + q_3^2) \cos \alpha_R + (-q_0q_2 + q_1q_3) \sin \alpha_R] \quad (\text{B.33})$$

$$B_{R_{3,2}} = -\frac{T_L}{m} [(q_0^2 - q_1^2 - q_2^2 + q_3^2) \cos \alpha_L + (-q_0q_2 + q_1q_3) \sin \alpha_L] \quad (\text{B.34})$$

$$B_{R_{3,3}} = \frac{1}{m} [2(q_1q_3 - q_0q_2) \cos \alpha_R + (-q_0^2 + q_1^2 + q_2^2 - q_3^2) \sin \alpha_R] \quad (\text{B.35})$$

$$B_{R_{3,4}} = \frac{1}{m} [2(q_1q_3 - q_0q_2) \cos \alpha_L + (-q_0^2 + q_1^2 + q_2^2 - q_3^2) \sin \alpha_L] \quad (\text{B.36})$$

THIS PAGE INTENTIONALLY LEFT BLANK

Bibliography

- [1] (2011, April) Northrop Grumman RQ-4 Global Hawk. [Online]. Available: http://www.ask.com/wiki/RQ-4_Global_Hawk?qsrc=3044
- [2] (2011, April) UAV Gallery. [Online]. Available: http://darkangelreport.com/UAV_Gallery.htm
- [3] “U.S. Air Force Fact Sheet RQ-11B Raven System,” U.S. Air Force Special Operations Command, Hurlburt Field, FL, November 2009. [Online]. Available: http://www.avinc.com/downloads/USAF_Raven_FactSheet.pdf
- [4] “U.S. Air Force Fact Sheet Wasp III Micro Unmanned Aircraft System,” U.S. Air Force Special Operations Command, Hurlburt Field, FL, 2011. [Online]. Available: <http://www.avinc.com/downloads/USAirForceFactSheet.pdf>
- [5] *Jane's Unmanned Aerial Vehicles and Targets*, Jane's Information Group, July 2009.
- [6] A. L. Desbiens, A. Asbeck, and M. Cutosky, “Hybrid Aerial and Scansorial Robotics,” in *IEEE International Conference on Robotics and Automation*, Anchorage, Alaska, 3-8 May 2010.
- [7] M. L. Anderson, C. J. Perry, B. M. Hua, D. S. Olsen, J. R. Parcus, K. M. Pederson, and D. D. Jensen, “The Sticky-Pad Plane and other Innovative Concepts for Perching UAVs,” in *47th AIAA Aerospace Sciences Meeting*, Orlando, Florida, 5-8 January 2009.
- [8] R. J. Bachman, F. J. Boria, R. Vaidyanathan, P. G. Ifju, and R. D. Quinn, “A Biologically Inspired Micro-Vehicle Capable of Aerial and Terrestrial Locomotion,” *Mechanism and Machine Theory*, vol. 44, pp. 513–526, 2009.
- [9] A. Noth, “Design of Solar Powered Airplanes for Continuous Flight,” Ph.D. dissertation, Swiss Federal Institute of Technology (ETH) Zurich, Zurich, 2008.

- [10] N. Diepeveen, "The Sun-Surfer," Autonomous Systems Lab, Swiss Federal Institute of Technology (ETH) Zurich, Zurich, Internship Report, 2007.
- [11] M. Bronz, J. M. Moschettay, P. Brissetz, and M. Gorraz, "Towards a Long Endurance MAV," *International Journal of Micro Air Vehicles*, vol. 1, no. 4, pp. 241–254, December 2009.
- [12] (2011, April) Sikorsky MARINER/"Cypher II". [Online]. Available: http://www.aviastar.org/helicopters_eng/sik_cypher2.php
- [13] (2011, April) X-50A Dragonfly Canard Rotor/Wing prototype completes hover flight. [Online]. Available: <http://www.gizmag.com/go/4906/picture/17736/>
- [14] (2011, April) GoldenEye 50. [Online]. Available: <http://www.aurora.aero/TacticalSystems/GoldenEye50.aspx>
- [15] (2011, April) Guided Systems selected by IAS to provide Adaptive Neural Network flight controls technology for their newest Pitagora VTOL UAV. [Online]. Available: <http://www.guidedsys.com/news.php>
- [16] (2011, April) The Bell Eagle Eye UAV ready to fly. [Online]. Available: <http://www.gizmag.com/go/3006/picture/5637/>
- [17] (2011, April) V-BAT UAV. [Online]. Available: http://www.spyplanes.com/pages_new/products.htm
- [18] F. Kendoul, I. Fantoni, and R. Lozano, "Modeling and Control of a Small Autonomous Aircraft Having Two Tilting Rotors," in *44th IEEE Conference on Decision and Control*, Seville, Spain, 2005.
- [19] "Predator," General Atomics, April 2011. [Online]. Available: <http://www.ga-asi.com/products/aircraft/predator>
- [20] "The U.S. Air Force Remotely Piloted Aircraft and Unmanned Aerial Vehicle Strategic Vision," U.S. Air Force, 2005.
- [21] "RQ-4 Global Hawk Fact Sheet," May 208. [Online]. Available: http://www.as.northropgrumman.com/products/ghrq4a/assets/HALE_Factsheet.pdf
- [22] K. L. Cook, "The Silent Force Multiplier: The History and Role of UAVs in Warfare," in *Proceedings of IEEE Aerospace Conference*, no. 1619. Big Sky, Montana: U.S. Air Force, March 2007.

- [23] E. D. McCormack, "The Use of Small Unmanned Aircraft by the Washington State Department of Transportation," Washington State Transportation Center, University of Washington, Seattle, Washington, Research Report WA-RD 703.1, June 2008.
- [24] A. Noth, "Sky-Sailor Solar Powered Airplane Proved Continuous Flight," Swiss Federal Institute of Technology (ETH) Zurich, Zurich, Tech. Rep., 2008.
- [25] M. Raju, "Energy Harvesting," Texas Instruments Incorporated, Whitepaper, 2008. [Online]. Available: http://www.ti.com/corp/docs/landing/cc430/graphics/slyy018_20081031.pdf
- [26] "Kestrel Autopilot System," 2010. [Online]. Available: http://www.procerusuav.com/Downloads/DataSheets/Kestrel_2.4.pdf
- [27] "Piccolo Flight Management System," 2011. [Online]. Available: <http://www.cloudcaptech.com/Sales%20and%20Marketing%20Documents/Piccolo%20Autopilot%20System.pdf>
- [28] "Skate UAS," Aurora Flight Sciences, June 2010. [Online]. Available: <http://www.aurora.aero/Common/Images/ResearchDevelopment/RDfact.pdf>
- [29] A. Frank, J. S. McGrew, M. Valenti, D. Levine, and J. P. How, "Hover, transition, and level flight control design for a single-propeller indoor airplane," in *AIAA Guidance, Navigation and Control Conference and Exhibit*, no. AIAA 2007-6318, Hilton Head, South Carolina, 20 - 23 August 2007.
- [30] J. A. Duffie and W. A. Beckman, *Solar Engineering of Thermal Processes*, 3rd ed. Wiley, 2006.
- [31] "Solar Radiation," NASA, April 2011. [Online]. Available: <http://atmospheres.gsfc.nasa.gov/climate/index.php?section=136>
- [32] S. A. Brandt, R. J. Stiles, J. J. Bertin, and R. Whitford, *Introduction to Aerodynamics: A Design Perspective*, 2nd ed. AIAA, 2004.
- [33] T. J. Mueller, J. C. Kellogg, P. G. Ifju, and S. V. Sharayev, *Introduction to the Design of Fixed-Wing Micro Air Vehicles*. AIAA, 2007.
- [34] "Cell Type: S 32," Azur Space Solar Power GMBH, April 2007. [Online]. Available: <http://azurspace.de/index.php?mm=74>

- [35] D. P. Raymer, *Aircraft Design: A Conceptual Approach*, 4th ed. AIAA, 2006.
- [36] “Thunder Power RC,” 2011. [Online]. Available: <http://thunderpowerrc.com/PDF/ThunderPowerRC-Pricing.pdf>
- [37] D. C. D. Martin D. Maisel, Demo J. Giulianetti, *The History of the XV-15 Tilt Rotor Research Aircraft: From Concept to Flight*. NASA, 200.
- [38] L. C. P. T. USMC, “The V-22 Controversy,” National War College, Washington,DC, report, 1992.
- [39] M. E. Dreier, *Introduction to Helicopter and Tiltrotor Flight Simulation*. AIAA, 2007.
- [40] S. W. Choi, Y. S. Kim, and J. S. Lee, “Design and Test of Small Scale Ducted-Prop Aerial Vehicle,” in *47th AIAA Aerospace Sciences Meeting*, Orlando, FL, January 5-9 2009.
- [41] G. R. Gress, “Using Dual Propellers as Gyroscopes for Tilt-Prop Hover Control,” in *Biennial International Powered Lift Conference*, Williamsburg, Virginia, 2002.
- [42] H. L. Kelley and R. A. Champine, “Flight Operating Problems and Aerodynamic and performance characteristics of a Fixed-Wing,Tilt-Duct, VTOL Research Aircraft,” Langely Research Center, Hampton, VA, Tech. Rep., July 1963.
- [43] F. Sobolic, “Agile Flight Control Techniques for a Fixed-Wing Aircraft,” Master’s thesis, Massachusetts Institute of Technology, 2009.
- [44] N. B. Knoebel, “Adaptive Quaternion Control of a Miniature Tailsitter UAV,” Master’s thesis, Brigham Young University, 2007.
- [45] W. E. Green, “A Multimodal Micro Air Vehicle for Autonomous Flight in Near-Earth Environments,” Ph.D. dissertation, Drexel University, 2007.
- [46] W. Null, A. Noseck, and S. Shkarayev, “Effects of Propulsive-Induced Flow on the Aerodynamics of Micro Air Vehicles,” in *23rd AIAA Applied Aerodynamics Conference*, Toronto, Ontario, June 6-9 2005.
- [47] T. R. Yechout, S. L. Morris, D. E. Bossert, and W. F. Hallgren, *Introduction to Aircraft Flight Mechanics*. AIAA, 2003.

- [48] D. M. Black, H. S. Wainauski, and C. Rohrbach, “Shrouded Propellers - A Comprehensive Performance Study,” in *AIAA 5th Annual Meeting and Technical Display*, Philadelphia, PA, 1968.
- [49] E. N. Johnson, M. A. Turbe, A. D. Wu, S. K. Kannan, and J. C. Neidhoefer, “Flight Test Results of Autonomous Fixed-Wing UAV Transitions to and from Stationary Hover,” in *AIAA Guidance, Navigation, and Control*, Keystone, CO, August 2006.
- [50] E. Frazzoli, “Robust Hybrid Control for Autonomous Vehicle Motion Planning,” Ph.D. dissertation, Massachusetts Institute of Technology, 2001.
- [51] R. Tedrake, I. R. Manchester, M. Tobenkin, and J. W. Roberts, “LQR-trees: Feedback Motion Planning via Sums-of-Squares Verification,” *The International Journal of Robotics Research*, vol. 29, no. 8, July 2010.
- [52] A. J. Hanson, *Visualizing Quaternions*. San Francisco, CA: Elsevier, 2006.
- [53] J. B. Kuipers, *Quaternions and Rotation Sequences: A Primer with Applications to Orbits, Aerospace and Virtual Reality*. Princeton University Press, 1999.
- [54] J. C. Chou, “Quaternion Kinematic and Dynamic Differential Equations,” in *IEEE Transactions on Robotics and Automation*, February 1992.
- [55] B. Michini, “Modeling and Adaptive Control of Indoor Unmanned Aerial Vehicles,” Master’s thesis, Massachusetts Institute of Technology, 2009.
- [56] J.-J. E. Slotine and W. Li, *Applied Nonlinear Control*. Upper Saddle River, NJ: Prentice-Hall, 1991.
- [57] S. Prajna, A. Papachristodoulou, P. Seiler, and P. A. Parrilo, *SOSTOOLS: Sum of Squares Optimization Toolbox for MATLAB*, 2004.
- [58] Z. W. Jarvis-Wloszek, “Lyapunov Based Analysis and Controller Synthesis for Polynomial Systems using Sum-of-Squares Optimization,” Ph.D. dissertation, UNIVERSITY OF CALIFORNIA, BERKELEY, 2003.
- [59] (2011, May) Optical Flow. [Online]. Available: <http://centeye.com/technology-and-research/optical-flow/>